JKU

**JOHANNES KEPLER
UNIVERSITY LINZ**

Author
Gabriel Weissitsch B.Sc.

Submission
**Institute of Electrical
Drives and Power
Electronics**

Thesis Supervisor
**Univ.-Prof. DI Dr. Gerd
Bramerdorfer**

Assistant Thesis
Supervisor
**Assoc.-Prof. Dr. Greg
Heins**

September 2023

DESIGN OF A VARIABLE AIR GAP AXIAL FLUX MACHINE

Master's Thesis

to confer the academic degree of

Diplom-Ingenieur

in the Master's Program

Mechatronics

Sworn Declaration

I hereby declare under oath that the submitted Master's Thesis has been written solely by me without any third-party assistance, information other than provided sources or aids have not been used and those used have been fully documented. Sources for literal, paraphrased and cited quotes have been accurately credited.

_____

Place, Date

_____

Signature

Acknowledgements

English Abstract

Machines utilising permanent magnets to produce the rotor flux generally have a low efficiency when operating at high speeds. This is also true for the axial flux machine topology. However, axial flux machines provide a unique solution to increase efficiency at high speeds. By varying the air gap width between the rotor and stator, a mechanical rotor flux linkage control is made possible. An increased air gap decreases the rotor flux linkage and therefore reduces the necessary field weakening current for high speeds.

Air gap variation increases the computational cost of machine evaluation substantially, as it introduces a new dimension of freedom in the machine operation. This poses a challenge, as finding an optimal machine design for a given application depends, amongst other things, on the number of evaluated designs. For this reason, it is essential to reduce the computational expense of the machine evaluation as much as possible. This thesis introduces a computationally efficient method of evaluating axial flux machines with mechanical flux linkage control through air gap variation. The investigated machine is designed as a traction drive for a racecar in the Formula Student series.

Following the machine evaluation concept, two distinct design scenarios are presented and compared. In the first scenario, a relatively simple static air gap model is used and the machine is optimised for a single operating point. The second scenario uses the evaluation method proposed in this thesis and optimises the variable air gap machine for a driving cycle. The results indicate that machine efficiency can be significantly increased through air gap variation.

A specific design is chosen for some in-depth investigations, as a prototype design and for validation. The prototyping process is highlighted and the test setup to achieve air gap variation is shown. The machine is tested at different operating conditions and air gap widths. The acquired experimental data is compared to FEA results to validate the simulation model. The comparison shows, that the data generally correlates, but some discrepancies between simulation and experimental results exist. However, the results form a solid basis for future research to build upon.

German Abstract

Permanentmagneterregte Maschinen haben grundsätzlich einen schlechten Wirkungsgrad bei hohen Drehzahlen. Dies trifft auch auf Axialflussmaschinen zu, jedoch gibt es speziell bei diesem Maschinentyp eine Möglichkeit zur Erhöhung des Wirkungsgrades im Hochdrehzahlbereich. Durch die Veränderung der Luftspaltweite zwischen dem Stator und Rotor lässt sich die Rotorflussverkettung beeinflussen. Ein Vergrößern der Luftspaltweite verringert die Rotorflussverkettung und reduziert damit den für hohe Drehzahlen üblicherweise notwendigen Feldschwächungsstrom.

Durch die Veränderung der Luftspaltweite wird ein neuer Freiheitsgrad im Betrieb der Maschine geschaffen. Dadurch erhöht sich der notwendige Rechenaufwand im Entwurfsprozess enorm. Um das optimale Maschinendesign zu finden, muss eine große Menge verschiedener Designs analysiert werden, weshalb es essenziell ist den Rechenaufwand zu minimieren. In dieser Arbeit wird ein recheneffizientes Verfahren zur Analyse von Axialflussmaschinen mit veränderbarer Luftspaltweite vorgestellt. Die untersuchte Maschine wird als Traktionsantrieb für ein Rennfahrzeug in der Formula Student Serie ausgelegt.

Zwei verschiedene Entwurfsszenarien werden vorgestellt und verglichen. Im ersten Szenario wird ein relativ einfaches Maschinenmodell mit einem statischen Luftspalt verwendet und die Maschine für einen einzigen Betriebspunkt optimiert. Im zweiten Szenario wird das in dieser Arbeit vorgestellte Analyseverfahren verwendet und die Maschine für variable Luftspaltweite und unter Berücksichtigung von Fahrzyklen optimiert. Die Ergebnisse zeigen, dass der Wirkungsgrad der Maschine durch Luftspaltveränderung deutlich gesteigert werden kann.

Ein Maschinendesign wird ausgewählt und ein Prototyp gebaut. Der Aufbau des Prototyps sowie der Mechanismus für die Veränderung der Luftspaltweite wird vorgestellt und die Maschine getestet. Der Vergleich der Messdaten zu Simulationsergebnissen zeigt, dass die Daten grundsätzlich korrelieren, jedoch bei einigen Ergebnissen Diskrepanzen bestehen. Die vorliegenden Ergebnisse bilden jedoch eine solide Grundlage für zukünftige Forschung.

Contents

1 Introduction

1.1 Motivation

Electric machines have become the building blocks for achieving a net-zero carbon future. With this in mind, it is not surprising that an unprecedented rise in the adoption of electric machines has taken place in the recent past. For example, the sales of plug-in electric vehicles (EVs) have experienced a compound annual growth rate of 56 % globally over the last ten years [1].

While electrification is the first step to a carbon-neutral future, it is also imperative to increase the energy conversion efficiency of electric machines. Electric motors account for approximately 70 % of all the consumed energy in the EU with electricity demand for EVs reaching an all-time high of 65 thousand GWh in 2022 [2, 3]. Minimising the wasted energy of electric traction drives is therefore vital.
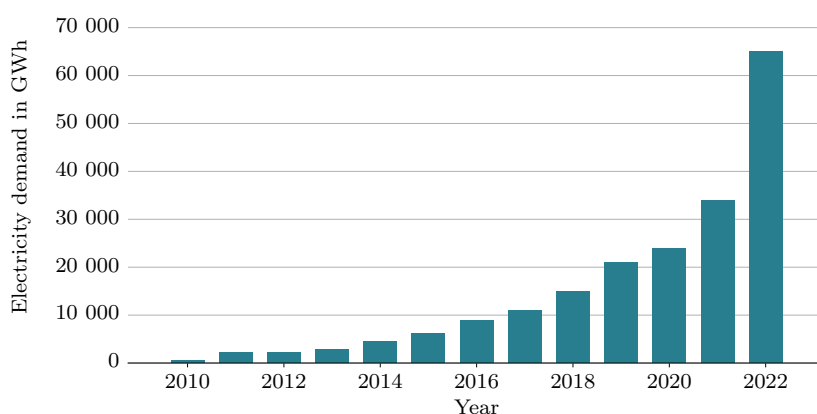
Figure 1.1: Electricity demand for EVs from 2012 to 2022 [2]

In the automotive industry, numerous significant Energy Efficient and Low-Carbon (ELC) innovations have been pioneered by motorsports [4]. New exploratory technologies are developed in motorsports, with the hope of gaining a competitive advantage. The research and development of these technologies may not be economically viable otherwise.

The goal of this project is to create a novel, more energy-efficient traction drive for an electric racecar in the motorsport series Formula Student. The focus lies on the electromagnetic design and optimisation of the investigated machine to achieve the highest possible efficiency.

1.2 Formula Student

Formula Student is a design competition with teams from universities all over the world. Students design, develop and fabricate formula-style racecars to compete in different challenges against other universities. In conjunction with the recent development in the automotive industry, many universities' focus has shifted from combustion engines to electric powertrains. Fig. 1.2 shows Monash University's 2022 electric racecar.

Figure 1.2: Monash Motorsport Formula Student 2022 racecar

The on-track competition is divided into four different events with different requirements and operating conditions for the racecar. Points are awarded, depending on the performance in four different events. The Acceleration Event tests the car's straight-line acceleration over a distance of 75 m. In the Skidpad Event, a figure of eight with diameters of 15.25 m, is passed through to test the lateral acceleration capability of the car. A

single 800 m long flying lap of a track is timed in the Autocross Event. In the Endurance Event, multiple laps of a racetrack with a total of 22 km are completed. The Endurance Event is the only dynamic event, where points are not only awarded for the shortest time but also for the least energy consumption.

Powertrain efficiency is not just important for scoring points in the Endurance Event. An inefficient motor means more energy is needed for the driving cycle, which in turn means that more accumulator mass has to be added to the vehicle, making the car slower. Loss is dissipated in the form of heat, so a less efficient motor produces more heat and therefore has a higher cooling requirement. For this reason, efficiency is key to this racing series.

1.3 Scope and Structure of the Thesis

This thesis presents the design, optimisation, prototyping and validation process of a specific machine topology.

Chapter 2 gives a brief overview of the fundamentals of electric machines, with a focus on their use as traction drives. The proposed topology is introduced and some benefits and challenges that come with the use of such a powertrain concept are highlighted.

Chapter 3 presents the proposed method to evaluate a machine design for a specific driving cycle. The focus of this chapter lies in the reduction of the computational cost, evaluating the machine with the combined use of finite element analysis (FEA) and analytical models.

Chapter 4 illustrates the optimisation methods employed for this project. Two different design scenarios are presented, comparing optimisation results from the evaluation method proposed in Chapter 3 to a more simple but frequently applied method.

Chapter 5 focuses on a single validation design, conducting some more in-depth evaluations. The prototyping process is highlighted and the machine is validated by comparing results acquired from simulation and experimental data.

Finally, Chapter 6 concludes this thesis and gives an outlook on possible future research.

2 Electric Machines as High Performance Traction Drives

2.1 Evolution of Electric Vehicle Traction

The first practical electric vehicles were developed in the late 19th century with direct current (DC) motors. These motors, however, had a large mass, low efficiency and bad reliability due to brushes and comutators. The first modern EVs, introduced in the late 20th century, featured mainly induction machines (IMs) in their powertrains. However, in the recent past, permanent magnet synchronous machines (PMSMs) have become the preferred topology for high-performance and racing applications. PMSMs feature an increased efficiency and higher power density when compared to IMs, with the main disadvantage being the dependence on rare-earth materials. Due to these advantages, the following sections focus on permanent magnet synchronous machines [1,5].

2.2 Fundamental Machine Characterisation

The following section gives a brief introduction to the fundamentals of electric machines. More detailed information about the fundamentals of electric machines can be found in the books by Hanselman [6] and Slemon [7]. A detailed investigation of electric vehicles is performed by Emadi [8]. Space Vector Control is described in the book by Vas [9] and more information on axial flux machines can be found in the book by Gieras et al. [10].

2.2.1 Space Vector Model of AC Machines

In a three-phase system, the a common way of denoting quantities like currents or voltages is using the abc-reference frame. In this frame, the complex state phasor of the stator

current and flux-linkage result to

$$\underline{i}_{\mathrm{s}}(t) = \frac{2}{3}(i_{\mathrm{a}}(t) + a\,i_{\mathrm{b}}(t) + a^2\,i_{\mathrm{c}}(t)) \tag{2.1}$$

and

$$\underline{\psi}_{\mathrm{s}}(t) = \frac{2}{3}(\psi_{\mathrm{a}}(t) + a\,\psi_{\mathrm{b}}(t) + a^2\,\psi_{\mathrm{c}}(t)) \tag{2.2}$$

respectively, with

$$a = \mathrm{e}^{\mathrm{j}\frac{2\pi}{3}}. \tag{2.3}$$

For the control of AC machines, it can be beneficial to also use different coordinate systems, namely the DQ-, and dq-reference frame. The d- and D-axis are denoted as the direct axis whereas the q- and Q-axis are called quadrature axis. The DQ-system transforms the three-phase values into a set of real and imaginary values with the D-axis being aligned with the a-axis of the three-phase system. This means that this reference frame is stationary to the machine's stator. The dq-frame also transforms the values to a set of real and imaginary values, but this system is stationary to the rotor with the d-axis being aligned with the rotor's flux-linkage-phasor. This means, that these two reference frames are offset by the rotor angle θ_r. Fig. 2.1 shows the different coordinate systems and their respective relation.
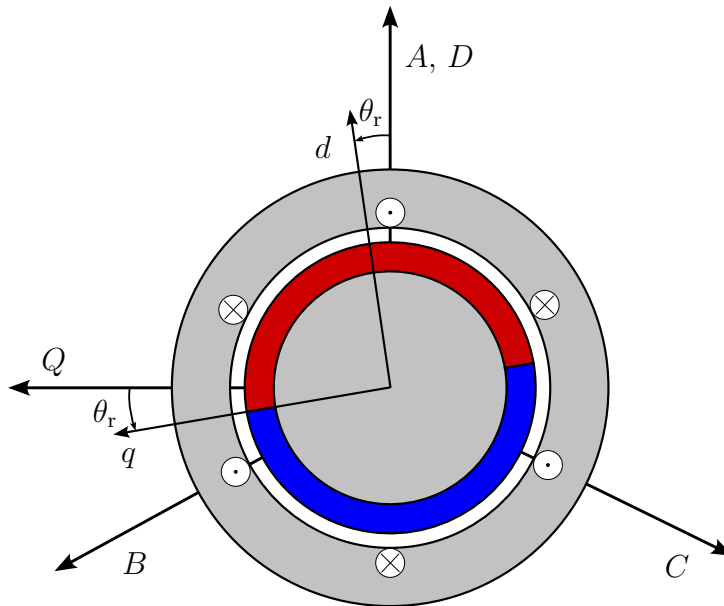

Figure 2.1: Different reference frames used for electric machines

The benefit of using the dq-system is that the flux-linkage vector and current vector are stationary. It should be noted, that this is only true with some assumptions, like stationary operating points, sinusoidal values and when using standard control techniques. This results in the AC machine having properties similar to a DC machine.

The conversion between DQ- and abc-frame is achieved using Clark's transformation

$$
\begin{bmatrix} x_{\mathrm{D}} \\ x_{\mathrm{Q}} \\ x_0 \end{bmatrix} = \boldsymbol{M}_{\mathrm{DQ0}} \begin{bmatrix} x_{\mathrm{a}} \\ x_{\mathrm{b}} \\ x_{\mathrm{c}} \end{bmatrix} \;\;,
\tag{2.4}
$$

with

$$
\boldsymbol{M}_{\mathrm{DQ0}} = \frac{2}{3} \begin{bmatrix} 1 & -\frac{1}{2} & -\frac{1}{2} \\ 0 & \frac{\sqrt{3}}{2} & -\frac{\sqrt{3}}{2} \\ \frac{1}{2} & \frac{1}{2} & \frac{1}{2} \end{bmatrix} .
\tag{2.5}
$$

For the abc- to dq-frame transformation the rotor angle θ_{r}, measured from the D-axis, is needed. The conversion is done using Park's transformation

$$
\begin{bmatrix} x_{\mathrm{d}} \\ x_{\mathrm{q}} \\ x_0 \end{bmatrix} = \boldsymbol{M}_{\mathrm{dq0}}(\theta_{\mathrm{r}}) \begin{bmatrix} x_{\mathrm{a}} \\ x_{\mathrm{b}} \\ x_{\mathrm{c}} \end{bmatrix} \;\;,
\tag{2.6}
$$

with

$$
\boldsymbol{M}_{\mathrm{dq0}}(\theta_{\mathrm{r}}) = \frac{2}{3} \begin{bmatrix} \cos(-\theta_{\mathrm{r}}) & \cos(\frac{2\pi}{3} - \theta_{\mathrm{r}}) & \cos(\frac{4\pi}{3} - \theta_{\mathrm{r}}) \\ \sin(-\theta_{\mathrm{r}}) & \sin(\frac{2\pi}{3} - \theta_{\mathrm{r}}) & \sin(\frac{4\pi}{3} - \theta_{\mathrm{r}}) \\ \frac{1}{2} & \frac{1}{2} & \frac{1}{2} \end{bmatrix} .
\tag{2.7}
$$

It should be noted that the variable x_0 in both transformations is introduced to allow for matrix inversion and thus making reverse transformation possible.

2.2.2 Operational Principles of PMSMs

Permanent magnet synchronous machines (PMSMs) utilise magnets to produce the rotor flux. This has the benefit that the rotor features no commutator or brush assembly and no excitation circuit. In addition, PMSMs have a higher efficiency and higher power density compared to electrically excited machines thanks to the loss-free creation of the rotor flux. The main disadvantage is the relatively high cost of rare earth magnets. For this reason, PMSMs have become the preferred topology for high-performance and racing applications.

The equivalent circuit of a PMSM is shown in Figs. 2.2 and 2.3. L_{md} and L_{mq} are the magnetising inductances, $L_{\sigma\mathrm{s}}$ and $L_{\sigma\mathrm{f}}$ are stray inductances and R_s is the resistance of the stator winding.
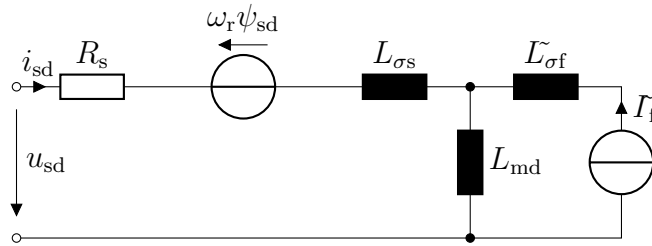
Figure 2.2: Equivalent circuit of a PMSM for the d-axis
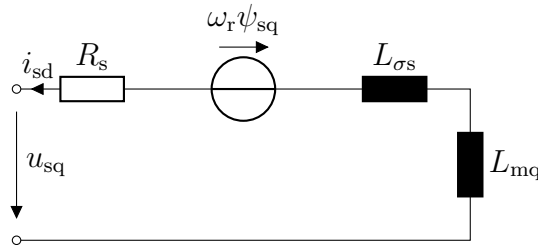
Figure 2.3: Equivalent circuit of a PMSM for the q-axis

The torque t of an AC machine depends on the number of poles, the stator flux linkage and stator currents and can be derived using

$$t = \frac{3}{2} p_{\mathrm{z}} \underline{\psi}_{\mathrm{s}} \times \underline{i}_{\mathrm{s}} \ . \tag{2.8}$$

Using the dq-coordinate system introduced in the previous chapter, the torque results to

$$t = \frac{3}{2} p_{\mathrm{z}} (\psi_{\mathrm{sd}} i_{\mathrm{sq}} - \psi_{\mathrm{sq}} i_{\mathrm{sd}}) \ . \tag{2.9}$$

In the following equations, the apostrophe indicates that the value is transformed from its source reference frame into the opposing system (DQ $\rightarrow$ dq or dq $\rightarrow$ DQ). The stator flux linkage results to

$$\underline{\psi}'_{\mathrm{s}} = \psi_{\mathrm{sd}} + \mathrm{j}\psi_{\mathrm{sq}} = L_{\mathrm{sd}}i_{\mathrm{sd}} + \mathrm{j}L_{\mathrm{sq}}i_{\mathrm{sq}} + L_{\mathrm{md}}I_{\tilde{\mathrm{f}}} \, , \tag{2.10}$$

where the first two terms represent the part of the flux produced by the stator coils. The last term is equivalent to the rotor flux linkage in the stator, as the properties of permanent magnets can be approximated by a set of coils with the current $I_{\tilde{\mathrm{f}}}$. The stator's self-inductance results as the sum of the magnetising inductance L_{md} or L_{mq} and stray inductance $L_{\sigma\mathrm{s}}$ with

$$L_{\mathrm{sd}} = L_{\mathrm{md}} + L_{\sigma\mathrm{s}} \, , \tag{2.11}$$

$$L_{\mathrm{sq}} = L_{\mathrm{mq}} + L_{\sigma\mathrm{s}} \, . \tag{2.12}$$

Under consideration of (2.10), the torque can be expressed as

$$t = \frac{3}{2}p_{\mathrm{z}}\Big[L_{\mathrm{md}}I_{\tilde{\mathrm{f}}}i_{\mathrm{sq}} + (L_{\mathrm{sd}} - L_{\mathrm{sq}})i_{\mathrm{sd}}i_{\mathrm{sq}}\Big]. \tag{2.13}$$

The first term is the permanent magnet torque. In commonly used machines it is responsible for the majority of torque production. The second term is called reluctance torque and only comes into effect if the rotor has a magnetic saliency.

The maximum speed of a permanent magnet machine depends amongst other things on the voltage supplied by the inverter. By increasing the supplied voltage, the speed and power of the machine can be increased up to a certain point. This is known as the constant torque region, as all available current can be used for torque production. The respective maximum speed is the base speed ω_{base}.

When the voltage limit of the inverter is reached, the speed can no longer be increased using this method. Some of the current is now used to field weaken the motor. This means torque is traded for speed while the power stays constant. Fig. 2.4 shows the speed-torque and power-torque curves of a PMSM with the constant torque region and the constant power region for a machine with no saliency.

The ratio between the maximum speed of the machine, ω_{max}, and the base speed is called the constant power speed range (CPSR).
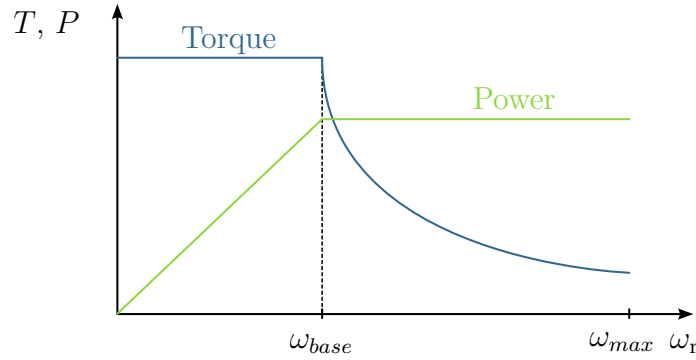
$$CPSR = \frac{\omega_{max}}{\omega_{base}} \; . \tag{2.14}$$

Figure 2.4: Speed-torque and power-torque curves of a PMSM

The voltage of a PMSM is defined as

$$\underline{u}'_{\mathrm{s}} = R_{\mathrm{s}}\underline{i}'_{\mathrm{s}} + \frac{\mathrm{d}\underline{\psi}'_{\mathrm{s}}}{\mathrm{d}t} + \mathrm{j}\omega_{\mathrm{r}}\underline{\psi}'_{\mathrm{s}} \tag{2.15}$$

Inserting equation (2.10) into equation (2.15) gives

$$
\begin{aligned}
u_{\mathrm{sd}} + \mathrm{j}u_{\mathrm{sq}} =& \left[R_{\mathrm{s}}i_{\mathrm{sd}} + L_{\mathrm{sd}}\frac{\mathrm{d}i_{\mathrm{sd}}}{\mathrm{d}t} + L_{\mathrm{md}}\frac{\mathrm{d}I_{\tilde{\mathrm{f}}}}{\mathrm{d}t} - \omega_{\mathrm{r}}L_{\mathrm{sq}}i_{\mathrm{sq}} \right] \\
&+ \mathrm{j}\left[R_{\mathrm{s}}i_{\mathrm{sq}} + L_{\mathrm{sq}}\frac{\mathrm{d}i_{\mathrm{sq}}}{\mathrm{d}t} + \omega_{\mathrm{r}}L_{\mathrm{sd}}i_{\mathrm{sd}} + \omega_{\mathrm{r}}L_{\mathrm{md}}I_{\tilde{\mathrm{f}}} \right] \; .
\end{aligned}
\tag{2.16}
$$

Assuming a steady-state operation of the machine with $\omega_{\mathrm{r}} = $ const., $i_{\mathrm{sd}} = $ const. and $i_{\mathrm{sq}} = $ const. simplifies the equation. Under this consideration and by applying RMS values, the voltage equation results to

$$U_{\mathrm{sd}} + \mathrm{j}U_{\mathrm{sq}} = \left[R_{\mathrm{s}}I_{\mathrm{sd}} - \omega_{\mathrm{r}}L_{\mathrm{sq}}I_{\mathrm{sq}} \right] + \mathrm{j}\left[R_{\mathrm{s}}I_{\mathrm{sq}} + \omega_{\mathrm{r}}L_{\mathrm{sd}}I_{\mathrm{sd}} + \omega_{\mathrm{r}}L_{\mathrm{md}}I_{\tilde{\mathrm{f}}}/\sqrt{2} \right] \; . \tag{2.17}$$

Fig. 2.5 shows the voltage vector diagrams for two different operating points of a permanent magnet synchronous machine, based on equation (2.17).
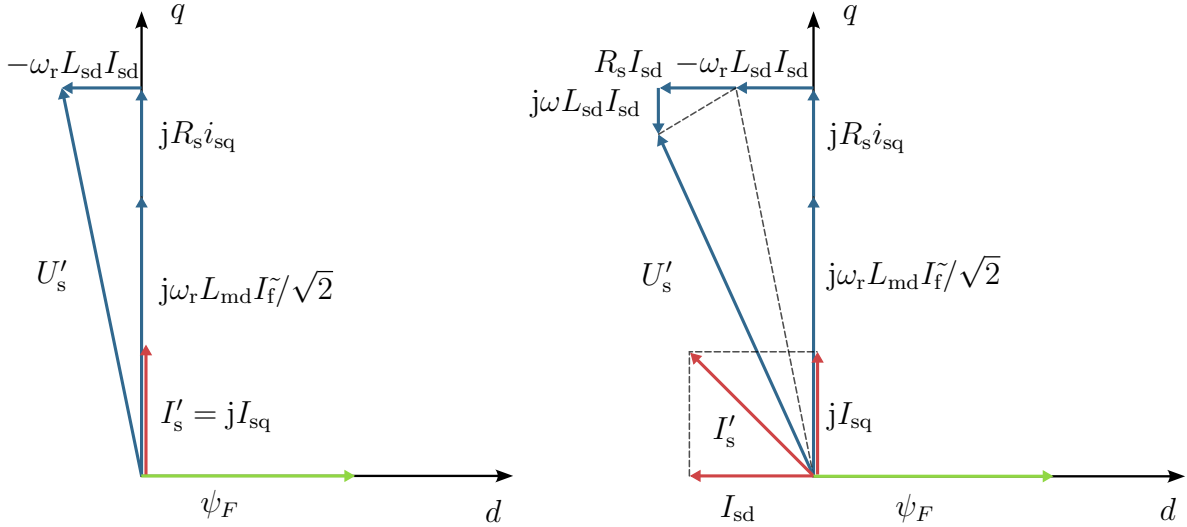
Figure 2.5: Phasor diagram for a PMSM during low-speed operation on the left and during field weakening on the right

The left image shows the vector diagram for optimal machine efficiency with no direct axis current I_{sd} under the assumption of no saliency and therefore no reluctance torque component. To increase the possible speed range, a negative d-axis current is introduced. By increasing the magnitude of this current, the norm of U_s' is decreased. This allows the speed to be further increased. The direct axis current increases the norm of I_s' while not contributing to torque. This means, that for increased direct axis current I_{sd}, the quadrature axis current I_{sq} must be decreased to avoid exceeding the inverter's current limit. While I_{sd} has no effect on torque production, it increases the machine's loss and therefore decreases the efficiency.

2.2.3 Losses in PMSMs

When an electric machine converts electrical into mechanical power, a part of the input power P_{in} is lost and dissipated in terms of heat. Fig. 2.6 shows the distribution of losses in electric machines. The air gap power P_δ is left over after all the stator losses are subtracted. Subtracting the rotor losses from the air gap power gives the output power P_{out} of the machine. For a PMSM the losses are separated into copper loss P_{cu}, core loss in the stator $P_{S,fe}$ and rotor $P_{R,fe}$, permanent magnet loss P_{pm}, stray loss P_{str} and mechanical loss P_{mech}.
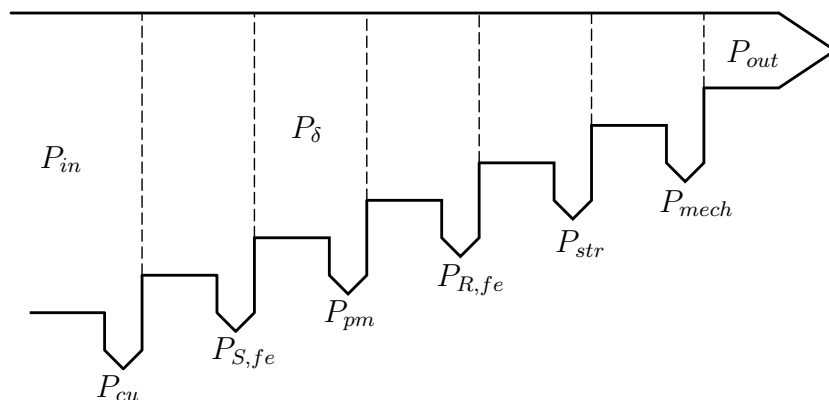
Figure 2.6: Loss distribution in electric machines

Copper Loss

Copper or joule losses P_{cu} appear due to the current distribution in a conductor. In the case of direct current I with uniform current density distribution in the conductor and the resistance R_{DC}, the copper loss can be derived as

$$P_{cu} = I^2 \cdot R_{DC}. \tag{2.18}$$

For alternating currents, the current density distribution is not homogeneous. The specific current density distribution is a result of the AC frequency, magnetic flux density as well as geometry of the slot and conductors. At high frequencies, skin and proximity effects cause the current density to increase on the surface and decrease in the centre of the conductor. This results in a net increase of the effective resistance and therefore higher copper loss.

Skin effect occurs due to eddy currents in the conductors. Alternating currents create a time-changing magnetic field, which in return creates a time-changing electric field opposing the magnetic field created by the alternating current. This opposing electric field induces a voltage, that pushes the electrons to the conductor's surface [8]. The qualitative distribution of the current density in a circular conductor at high frequency is shown in Fig. 2.7a.

Proximity effect is caused by eddy currents which in turn are caused by an external magnetic field. This external magnetic field is often created by the conductors in the vicinity. Fig. 2.7b shows the current density distribution for three circular conductors with the same current direction at high frequency interacting due to the proximity effect.
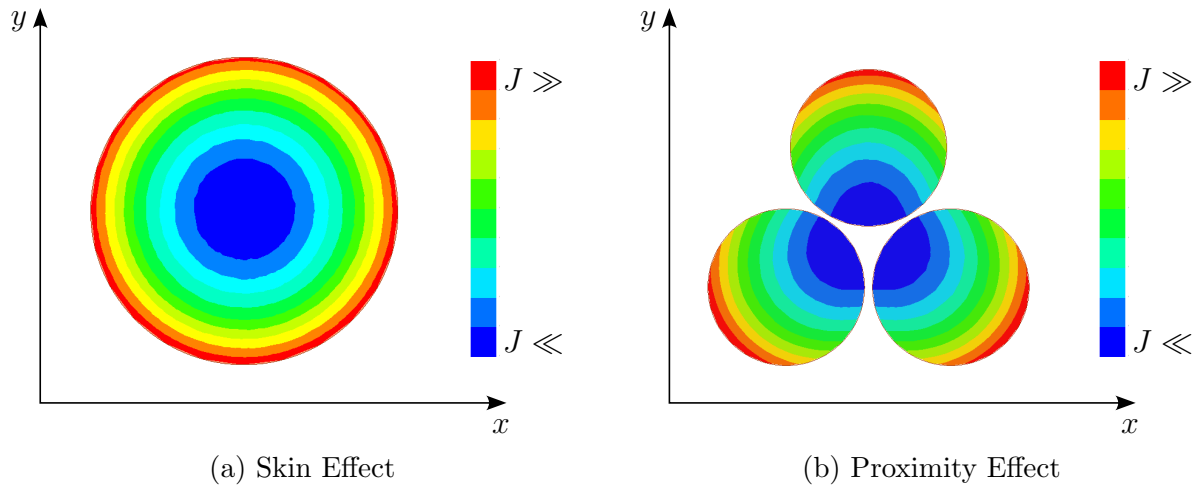
(a) Skin Effect   (b) Proximity Effect

Figure 2.7: Different alternating current effects in conductors

Core Loss

In the ferromagnetic material of the machine's magnetic core, losses occur due to hysteresis and eddy current effects.

Hysteresis loss appears due to the composition of ferromagnetic materials. These materials consist of domains in which the magnetic dipoles are fully lined up. The domains themself however are orientated randomly, resulting in a net-zero magnetic force. When an external magnetic field is applied, these dipoles try to align themselves with the direction of the magnetic field. The energy needed to change the orientation of these domains is called hysteresis loss. It depends on the strength of the magnetic flux density and the excitation frequency.

Eddy current losses also appear in magnetic materials. The alternating magnetic field induces eddy currents in the core, which in return create a magnetic field opposing the external field. For this reason, magnetic core materials are laminated with insulation layers between the segments of the core material. The summation of eddy current and hysteresis loss is the stator core loss $P_{S,fe}$ and rotor core loss $P_{R,fe}$.

Permanent Magnet Loss

In an ideal case with sinusoidal flux distribution, the field of a synchronous machine rotates at the same speed as the rotor. In reality, harmonics in the armature field induce eddy currents in the rotor circuit. The time-changing magnetic field induces eddy currents which create losses [8]. These are referred to as permanent magnet losses P_{pm}. Some magnet materials have very low conductivity and therefore low eddy current loss, in the case of high-performance neodymium-iron-boron (NdFeB) magnets the conductivity and therefore the losses are relatively high. To reduce eddy current loss, magnets are segmented, with an insulative layer between the segments.

Mechanical and Stray Loss

Friction occurs in the machine's bearings when the machine is in motion, creating losses. Another type of friction occurs when the machine rotates through the air molecules, this is referred to as windage loss. The summation of bearing friction and windage loss is the mechanical loss P_{mech}. Any excess loss that appears when testing the machine and which can not be attributed to any of the above losses, is referred to as a stray loss P_{str}.
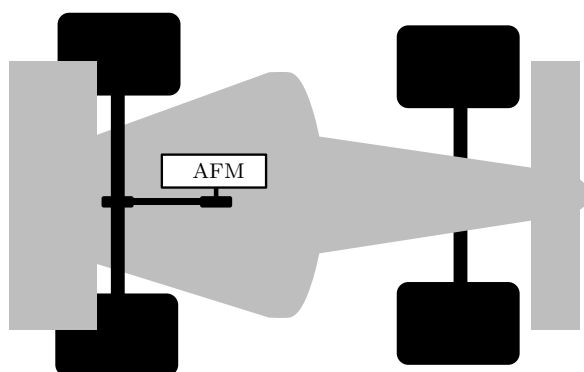
2.3 Commonly Used Powertrain Concepts in the Formula Student Racing Series

Internal combustion engine (ICE) cars have limited freedom when it comes to the position of the tractive power unit. ICEs are typically positioned in the centre of racing cars due to their relatively large size and high mass, allowing for even weight distribution.

Electric vehicles have higher freedom when it comes to the positioning of the powertrain, as multiple smaller and lighter electric motors can be used instead of a single heavy one. There are different ways of transferring the power created by the traction drive to the wheels. In any case, a gearbox is needed to increase the wheel torque and reduce the wheel speed. In the following, the two mainly used concepts in Formula Student are presented.

A common powertrain topology is the inboard axial flux machine (AFM). A single motor is placed inside the car's chassis behind the driver. This single motor powers the rear wheels through a transmission and differential. This concept can be beneficial for motor control, as only a single motor has to be controlled. Another benefit is that the entire mass of the machine, transmission and differential is sprung mass. A big disadvantage, however, is that in general only the two rear wheels are driven.

A very common off-the-shelf machine that is used for this kind of powertrain is the EM-RAX 228 motor. Fig. 2.8a displays this kind of concept and Fig. 2.8b shows a racecar that uses this powertrain topology. Axial flux machines are explained in more detail in the next section.

(a) Position of the single AFM in the racecar   (b) Racecar with single inboard motor

Figure 2.8: Formula Student inboard motor concept and example racecar

The second mainly used powertrain concept consists of outboard radial flux machines (RFMs). Instead of a single inboard motor producing the entire tractive power, multiple smaller machines are used. The motor and gearbox are placed in the wheel hubs of the racecar.

Either one pair of motors and gearboxes can be used in the two rear wheels, or a four-wheel drive system can be implemented by placing a motor and gearbox in every wheel hub. The benefit of this kind of four-wheel drive system is that every wheel can be controlled separately, thus enabling torque vectoring of the car in the corners. This lets the car rotate faster resulting in an improved lap time.

However, this concept comes with some disadvantages as well. Due to the position of the motor and gearbox in the wheel hubs of the car, the resulting mass is categorised as unsprung mass. Furthermore, the machine is exposed to the airflow in this arrangement, leading to a decrease in aerodynamic efficiency.

This topology is used by most larger and more successful teams today. Often custom motors are built by students for this kind of powertrain topology, the most common off-the-shelf machine for this use is the Fischer Elektromotoren Formula Student motor. The concept is illustrated in Fig. 2.9a and a racecar employing this kind of topology is shown in Fig. 2.9b.
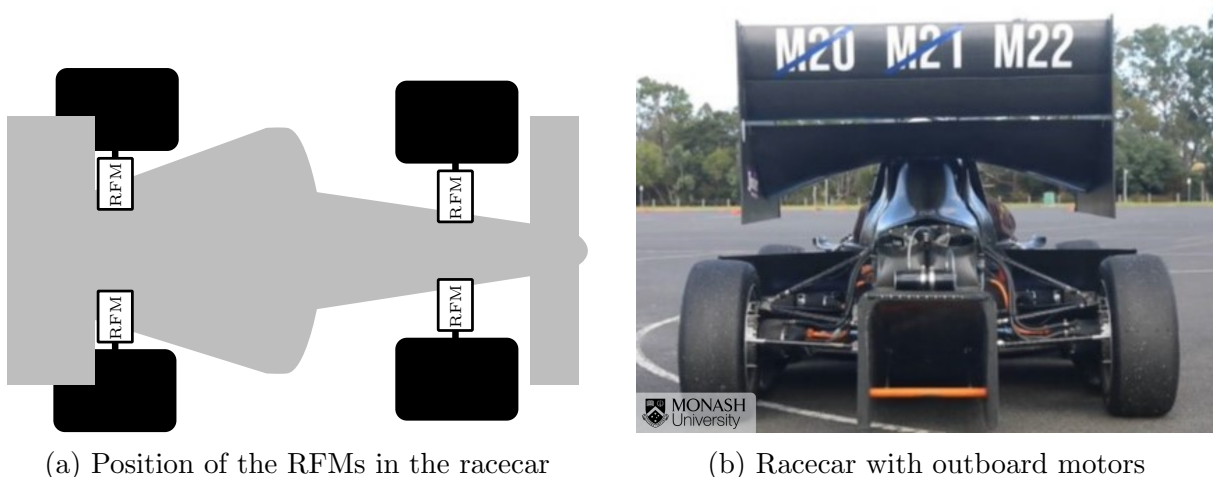

(a) Position of the RFMs in the racecar   (b) Racecar with outboard motors

Figure 2.9: Formula Student outboard motors concept and example racecar

2.4 Outboard Axial Flux Machines as Traction Drives

Axial flux machines are sometimes referred to as disc motors due to their distinctive disc-like shape. In the simplest form, they are composed of two discs, one stator and one rotor, that are spaced axially from each other. The machine's name comes from the direction the magnetic flux travels through the air gap. In AFMs, the flux moves axially through the air gap and tangentially and radially through the yoke. In radial flux machines, the flux passes through the air gap radially before moving tangentially through the yoke. Fig. 2.10 and 2.11a show the structure of a single-sided permanent magnet axial flux machine.
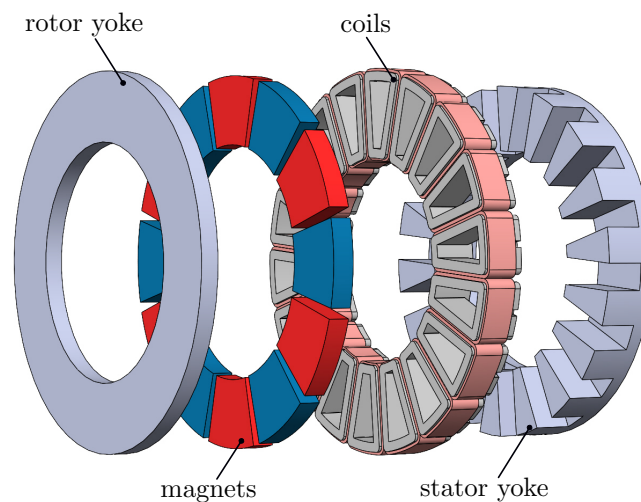

Figure 2.10: Axial flux machine components

Axial flux machines feature some advantages over radial flux machines for their utilisation as outboard traction drives. For example, the torque density is higher when compared to a similar-sized radial flux machine (RFM). The reason for this is that the entire machine diameter is used for torque production, while in RFMs only the rotor diameter can be utilised to produce torque.

One disadvantage of single-sided axial flux machines is that a strong axial force acts between the rotor and stator. This load has to be taken by bearings, located on the rotor shaft and can lead to reduced bearing life. To mitigate this problem, alternative AFM topologies are employed. For example, a double-sided AFM with two rotors and a single stator (Fig. 2.11b) or one rotor and two stators (Fig. 2.11c) can be used. Through the symmetric position of the two stators/rotors, the axial attraction forces cancel out. The downside, however, is the substantially increased mass of the machine and higher manufacturing complexity.

In the recent past, yokeless and segmented (YASA) machines (Fig. 2.11d) have gained a lot of attention for electric traction. A comparison between YASA and single-sided AFMs is performed in the papers by Taran et al. [11, 12]. Further information on current trends and recent research attention regarding axial flux machines can be found in the paper by Capponi et al. [13]. It should be noted, that the machine topologies illustrated in Fig. 2.11 are shown without stator windings.

(a) Single Sided AFM

(b) Double Rotor AFM

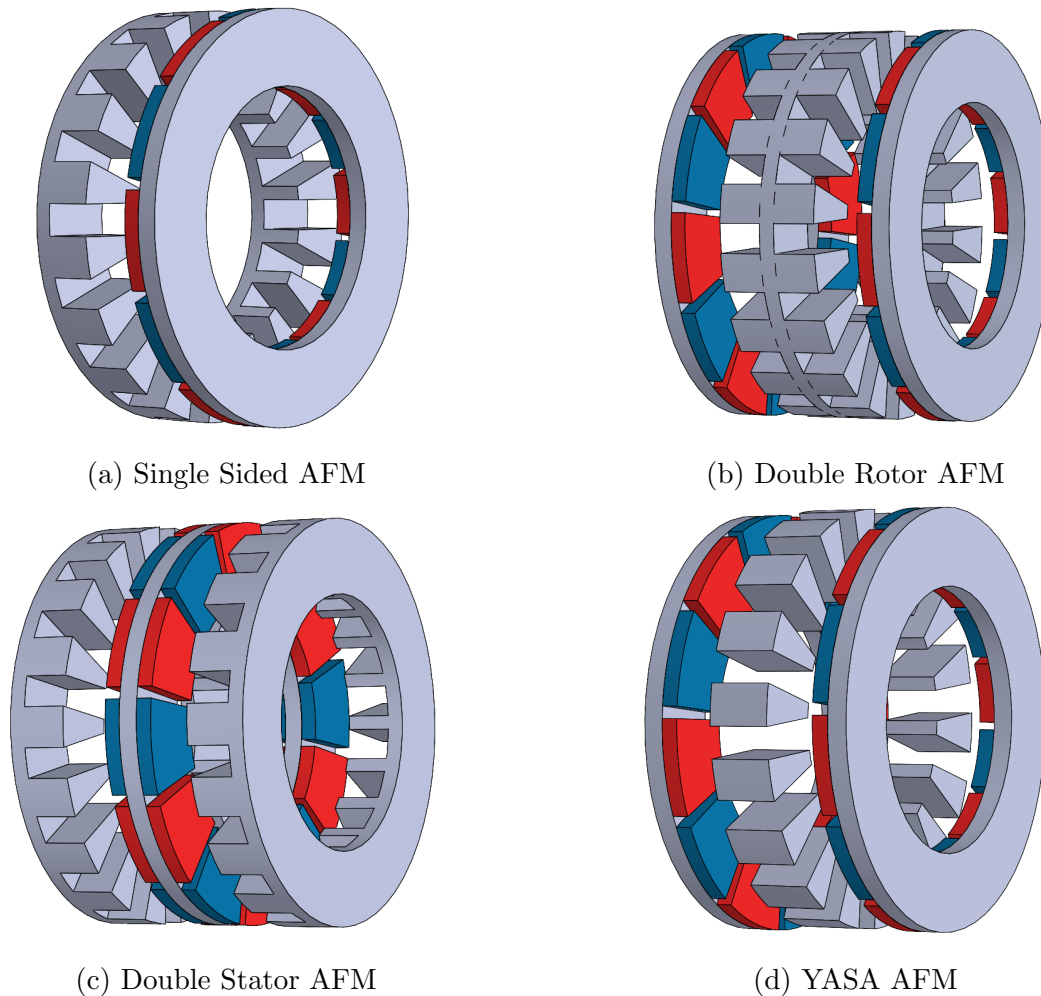(c) Double Stator AFM

(d) YASA AFM
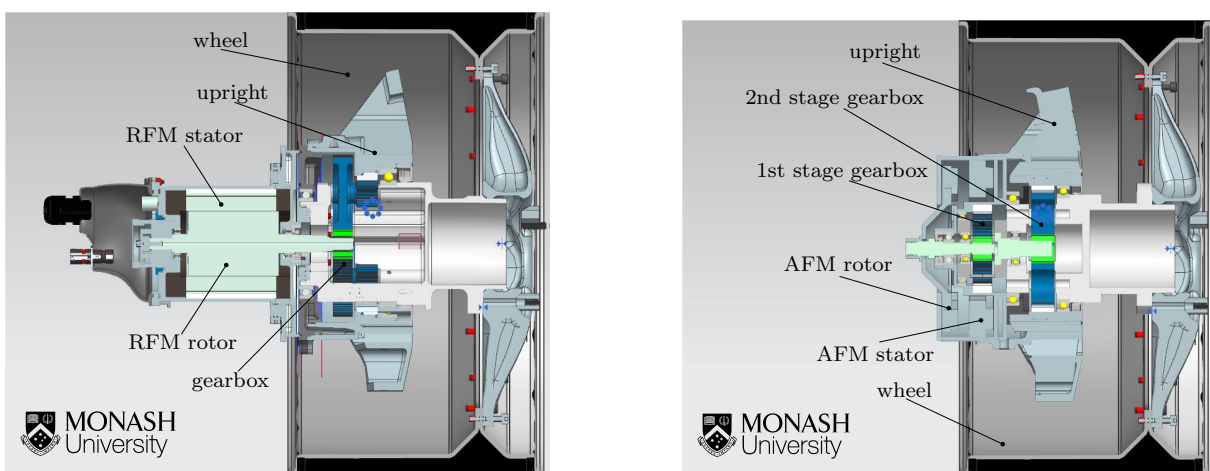
Figure 2.11: Different AFM topologies

Axial flux machines have a shorter axial length compared to radial flux machines due to their characteristic design. This fact is especially true for single-sided machine designs. When used as a traction drive in a car's wheel hub, a machine with a shorter axial length can be particularly beneficial, as it protrudes less into the air stream, resulting in increased aerodynamic efficiency.

Two different powertrain concepts are depicted in Fig. **??**. Both designs work similarly, they transfer the torque from a motor through a gearbox to the racecar's wheel. Fig. 2.12a shows an outboard concept of a radial flux machine with a planetary gearbox mounted to an upright inside the wheel.

Fig. 2.12b shows a possible concept of a single-sided axial flux machine with a two-stage planetary gearbox and upright inside a wheel. An additional smaller planetary gearbox is placed inside the inner diameter of the machine. This space is typically only used for the rotor shaft and bearings. Utilising this space for a first-stage gearbox increases the achievable reduction ratio while not increasing the machine's axial length. A higher gearbox reduction ratio allows an increased motor speed, and due to the relation between power P, speed ω and torque T

$$P = T \cdot \omega \tag{2.19}$$

results in an increased output power. As mentioned above, placing the first stage gearbox inside the machine does not increase the overall length and therefore does not penalise aerodynamic efficiency. However, the two-stage gearbox poses some engineering challenges in the construction process and during operation due to the limited space and necessary lubrication.

(a) Radial flux machine

(b) Axial flux machine

Figure 2.12: Outboard concepts with two different machine topologies

2.5 Air Gap Variation in Axial Flux Machines

Axial flux machines often utilise surface-mounted permanent magnets (SPMs), which are beneficial for manufacturing but generally have poor field-weakening capabilities and therefore a small CPSR [13]. However, axial flux machines' distinctive geometry allows for an interesting concept for extending the CPSR. By changing the air gap width between the rotor and stator, the machine's characteristics can be influenced as follows:

In the magnetic circuit from Fig. 2.13a, assuming a coil with N turns and the current i, the total mmf $\mathcal{F}$ can be calculated by
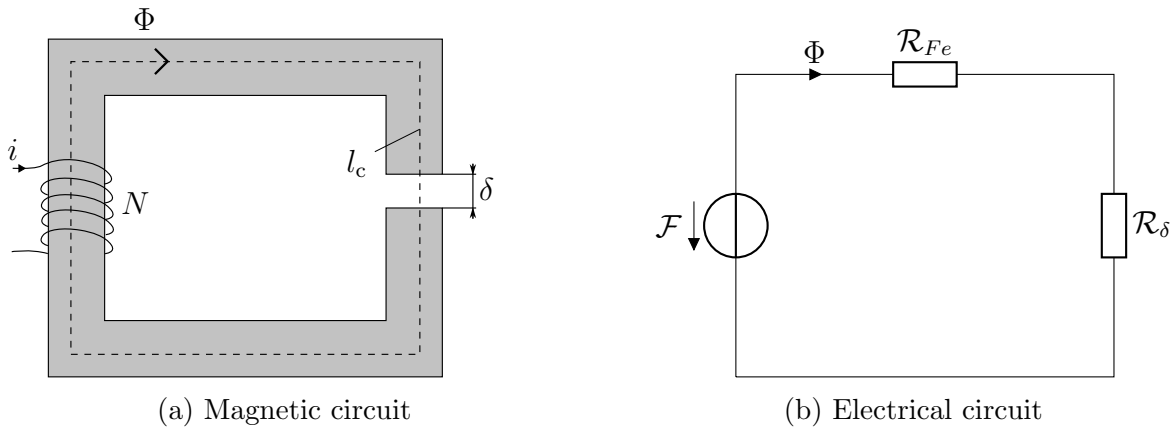
$$\mathcal{F} = Ni \ . \tag{2.20}$$

(a) Magnetic circuit

(b) Electrical circuit

Figure 2.13: Simple magnetic circuit and equivalent electrical circuit

For an air gap δ, total flux path length l_c, iron path length $l_{Fe} = l_\mathrm{c} - \delta$, and constant cross sectional area A, the reluctance of iron core and air gap are

$$\mathcal{R}_{Fe} = \frac{l_{Fe}}{\mu_0 \mu_{r,Fe} A} \ , \tag{2.21}$$

and

$$\mathcal{R}_\delta = \frac{\delta}{\mu_0 A} \ . \tag{2.22}$$

The relation between flux Φ, mmf and reluctance is

$$\mathcal{F} = \mathcal{R}\Phi \ , \tag{2.23}$$

with

$$\mathcal{R} = \mathcal{R}_\delta + \mathcal{R}_{Fe} \ . \tag{2.24}$$

Due to the fact that for a not saturated material $\mu_{r,Fe} \gg \mu_0$, $\mathcal{R}_{Fe}$ can be ignored and the total air gap flux results to

$$\Phi = \frac{\mathcal{F}}{\mathcal{R}_\delta} \ . \tag{2.25}$$

The total flux linkage can be expressed as

$$\psi = N\Phi = N^2 \frac{\mu_0 A}{\delta} i \tag{2.26}$$

Considering the equations above, it can be noted that the air gap flux linkage is inversely proportional to the air gap width.

In the previous section the high axial attraction force between rotor and stator was mentioned. To derive this force, the simple magnetic actuator in Fig. 2.14 is used.
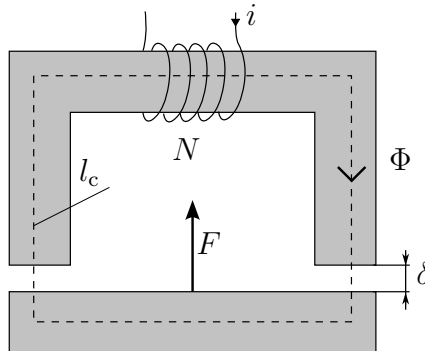

Figure 2.14: Simple magnetic actuator

Assuming a small displacement $d\delta$ of the movable armature, constant flux Φ and no losses, the law of energy conservation between mechanical W_m and magnetic field energy W_f is

$$dW_m + dW_f = 0 \ . \tag{2.27}$$

The change of mechanical energy through the displacement is dependant on the force F

$$dW_m = F \cdot d\delta \ . \tag{2.28}$$

The change in magnetic field energy depends on the magnetic flux density B, magnetic field strength H and change in volume dV

$$dW_f = -\frac{B\,H}{2} \cdot dV \ . \tag{2.29}$$

Assuming a linear relationship between B and H

$$B = \mu_0\,H \tag{2.30}$$

which is strictly only true in a vacuum, and a constant cross section area A gives

$$dW_f = -\frac{B^2}{2\mu_0} \cdot 2\,A\,d\delta \ . \tag{2.31}$$

With the relation between flux density B and flux Φ assuming no stray flux in the air gap

$$\Phi = B \cdot A \ , \tag{2.32}$$

and by inserting equations (2.28) and (2.31) into equation (2.27) gives

$$F = \frac{\Phi^2}{\mu_0\,A} \ . \tag{2.33}$$

Considering equations (2.25), (2.20) and (2.22) gives the resulting attraction force

$$F = N^2 \mu_0 A\,\frac{i2}{\delta^2} \ . \tag{2.34}$$

Consequently the axial force is dependant on the current squared and inversely dependant on the air gap width squared.

In a PMSM, the producible torque depends directly on the magnet flux linkage as equation (2.9) shows. High rotor flux linkage increases the permanent magnet torque (cf. equation 2.13), but also makes it more difficult to operate the machine at high speeds due to the high back-emf. This necessitates the use of field weakening, as illustrated in Fig. 2.5.

Field weakening operation is very inefficient as a current is introduced, which creates losses but for a machine with no saliency has no effect on torque. Equation (2.26) shows that by increasing the air gap between the rotor and stator, the magnet flux linkage can be reduced. Fig. 2.15 shows two vector diagrams for the machine. The left diagram shows the machine for a specific operating point, in analogy to the left diagram of Fig. 2.5. The

right plot shows a reduction in stator voltage through a reduction of the magnet flux ψ_F. The result is similar to the right diagram of Fig 2.5. However, no direct axis current was needed and thus efficiency is increased.

Another benefit of air gap variation is that the time-changing magnetic field, responsible for AC losses, is also reduced (cf. Section 2.2.3). This means, losses at high speed are reduced, and in turn, efficiency is further increased.
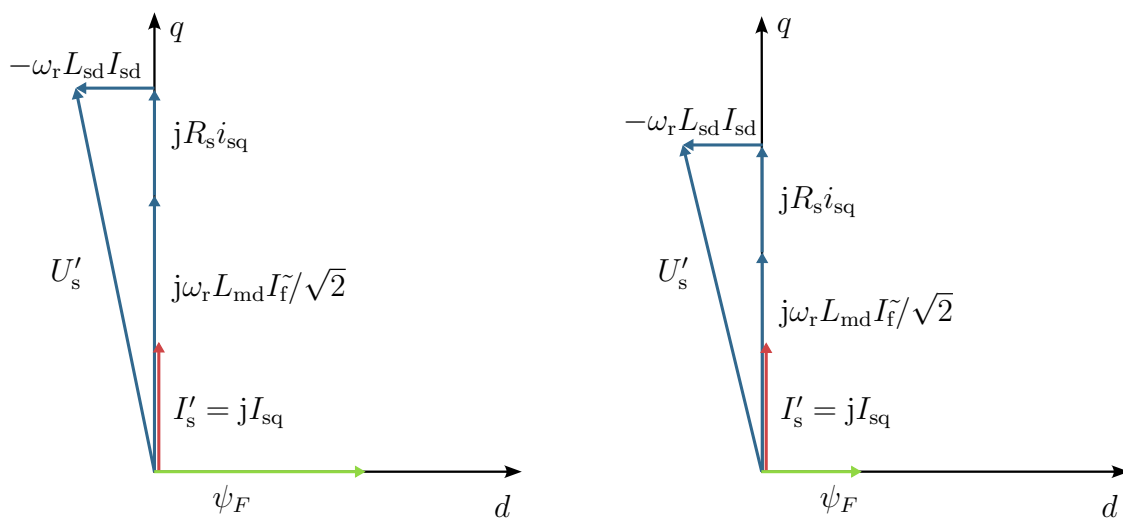

Figure 2.15: Phasor diagram of voltages for a PMSM during low-speed operation on the left and with reduced rotor flux linkage on the right

A viability investigation into air gap variation of AFMs for traction applications, as well as a concept mechanism to achieve dynamic air gap variation, are presented in the paper by Heins et al. [14]. The increase in operating range for an axial flux machine can be seen in Fig 2.16. The blue line shows the operating envelope for specific power electronics with no air gap variation and no direct axis current. The maximum torque and speed for the presented motor and inverter is roughly 27 Nm and 2500 rpm. The green line shows the reachable operating points for the same motor when air gap variation is allowed but still without the use of direct axis current. The higher torque is reached through a decrease of the nominal air gap width and higher speeds are achieved by increasing the air gap width. Fig. 2.17 shows the speed-torque map of the proposed machine, with contour lines for required air gap widths to achieve optimal efficiency.
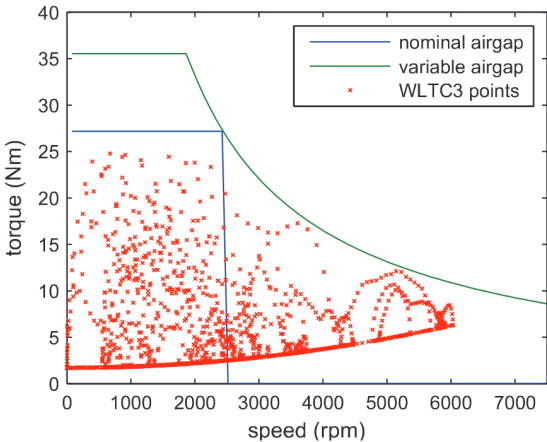
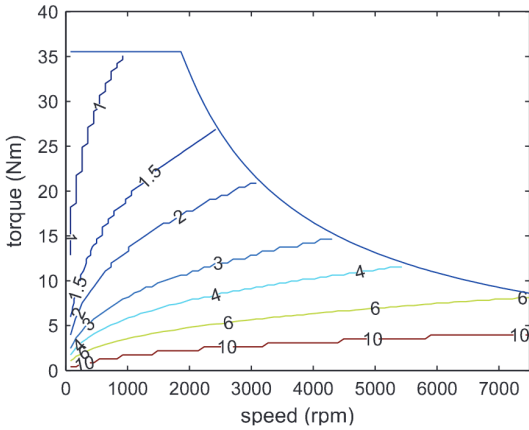Figure 2.16: Possible increase in operating range through air gap variation [14].

Figure 2.17: Air gap width for optimal efficiency [14].

3 Computationally Efficient Machine Evaluation Concept

3.1 Importance of Reducing Computational Cost

Apart from the machines used for electric vehicle traction, there are numerous other electric motors used in a typical BEV today, e.g. for the wipers, washers or window lifts. Most of these operate only at a single speed and torque operating point. This means that selecting an optimal design is fairly easy as you optimise only for that specific operating point.

Machines for electric traction however are required to operate efficiently at a variety of operating points and conditions. In addition, the penalty for an inefficient traction drive is high as the more energy is wasted, the more accumulator mass must be added to the vehicle to provide the same cruising range.

Finding an optimal machine design depends on the quality of optimisation, which depends, amongst other things, on the number of evaluated designs. For this reason, it is essential to reduce computational cost when modelling these machines to allow the evaluation of a significant number of designs in a reasonable time.

3.2 Geometry Transformation and Simplification

The axial flux machine topology by nature has a three-dimensional flux path. The flux moves axially along the air gap, tangentially through the yoke and radially through the teeth of the machine. For this reason, the most accurate way to quantify the machine's performance is to utilise three-dimensional FEA. However, 3D FEA is very computationally expensive and thus it takes a long time to analyse a whole electrical period for a given design at hand. To minimise the overall optimisation runtime, it is crucial to avoid the use of 3D analyses and facilitate the utilisation of 2D FEA.

3.2.1 Linear Machine Model

To avoid using computationally expensive 3D FEA, the axial flux machine can be converted to a two-dimensional geometry and solved with 2D FEA. For this, a cylindrical computation plane is selected at the average diameter

$$d_{avg} = \frac{d_o + d_i}{2} \tag{3.1}$$

of the machine (cf. Fig. 3.2). Different methods of creating a 2D model, like the Inner Rotor-, Outer Rotor- and Linear Motor Modelling Approach (LMMA) were investigated by Gulec et al. [15], with the LMMA performing well on average. For this thesis and the following investigations, the LMMA method is chosen. Fig. 3.1 shows the three different modelling approaches.
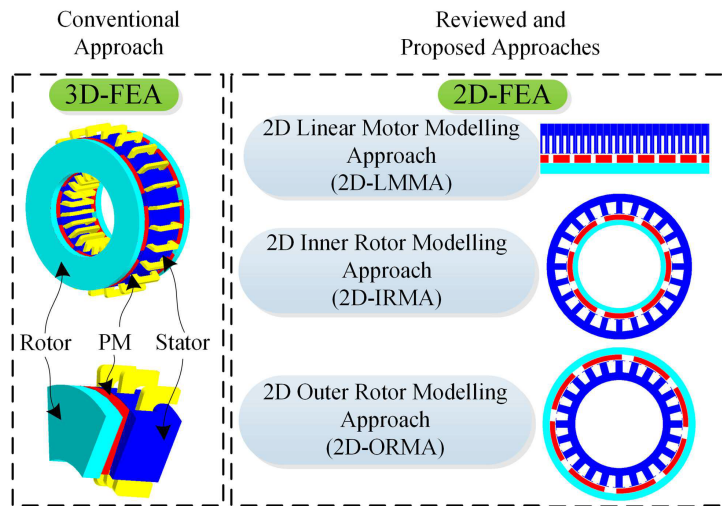

Figure 3.1: Different 2D modelling approaches [15]

The two-dimensional geometry's dimensions depend on the slice diameter d_{slice}, with the pole pitch τ_p and slot pitch τ_s being defined as

$$\tau_p = \frac{\pi \cdot d_{slice}}{2 \cdot p_z} \tag{3.2}$$

and

$$\tau_s = \frac{\pi \cdot d_{slice}}{N_s} \tag{3.3}$$

respectively. N_s represents the number of stator slots and p_z is the number of pole pairs.

In the resulting geometry, the flux is constrained to move only in two dimensions. This assumption is generally valid. However, when the core material saturates, the magnetic flux no longer moves solely in the desired direction, resulting in a significant decrease in accuracy.

This model allows for the use of two-dimensional FEA to characterise the machine. Figure 3.2 shows the computation plane in the 3D model and the resulting 2D geometry.
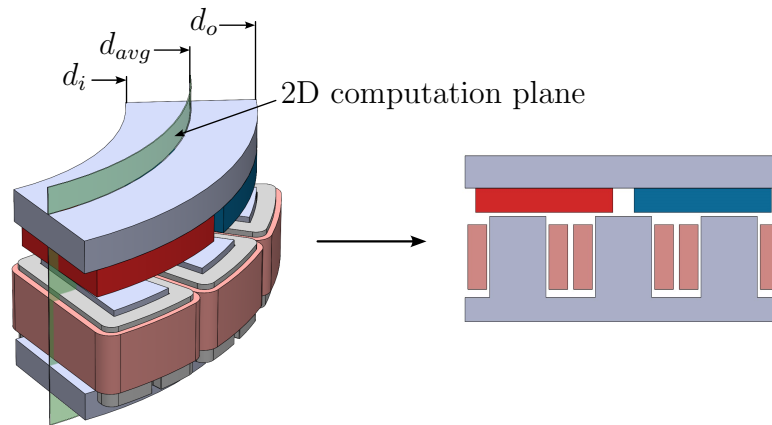

Figure 3.2: Transformation of a 3D axial flux machine to a 2D geometry

3.2.2 Quasi-3D Machine Model

The linear machine modelling approach presented in the previous subsection reduces computational cost substantially but relies on the assumption that the entire behaviour of the machine can be characterised by evaluating a single slice for a specified diameter. This of course is not true and can lead to non-negligible errors in machine analysis. For this reason, a quasi-3D model of the axial flux machine can be created.
Quasi-3D modelling utilises multiple two-dimensional models at different radii. FEA is performed on every slice and the results of all planes are averaged. By doing this, it becomes possible to consider geometry variations along the radius, e.g. when using triangular-shaped magnets. Figure 3.3 shows three cut planes in the three-dimensional model as well as the resulting 2D linear machine models at the three diameters.

The diameter d_{sl} of every computation plane i with z total planes is calculated by [16]

$$d_{sl,i} = d_o - (2 \cdot i - 1)\frac{l_s}{z},$$

(3.4)

with l_s being the core's length given by

$$l_s = \frac{d_o - d_i}{2}.$$

(3.5)

This approach allows a more accurate evaluation of axial flux machines. Nevertheless, it does not represent the three-dimensional flux behaviour of the machine, e.g. radial stray flux [16, 17].
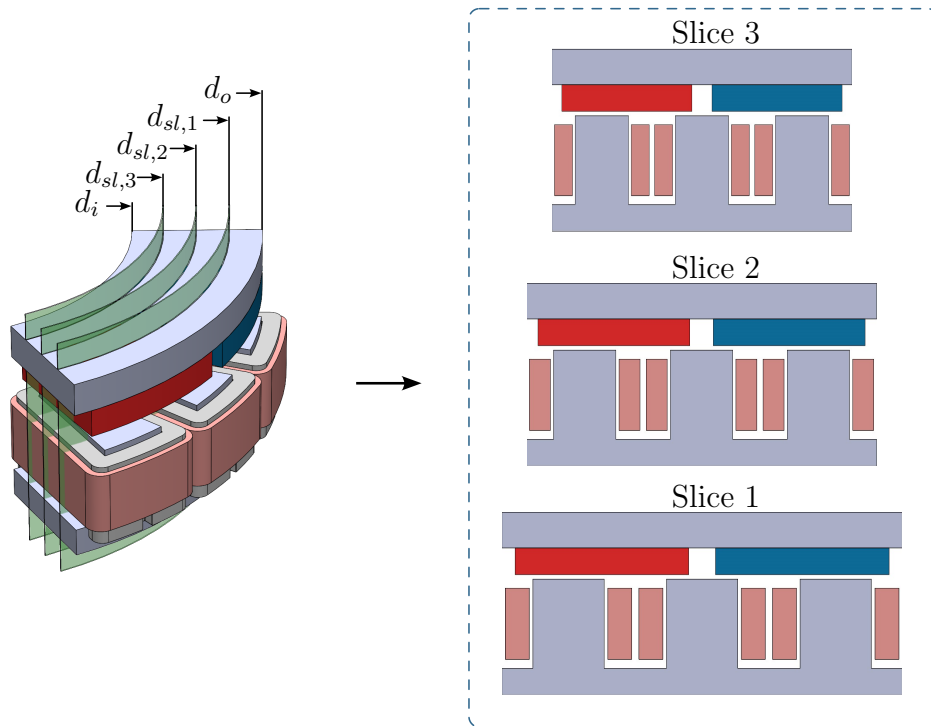

Figure 3.3: Transformation of a 3D axial flux machine to multiple 2D geometries

3.3 PMSM Motor Model

Evaluating a machine's performance for a specific driving cycle by running every speed and torque operating point in FEA would take excessive computation time. Likewise, a different driving cycle would necessitate reevaluating the machine in FEA, further increasing computational cost. For this reason, a flux-based PMSM motor model [18] is created for the machine under investigation.

A back-emf simulation is conducted to determine the position of the rotor fixed, direct and quadrature axes (cf. Section 2.2.1). The flux linkage and necessary q-axis current for a nominal operating point are also determined. Following this, different load cases, consisting of d-axis and q-axis current combinations (fig. 3.4), are evaluated using FEA and the results from all 2D models are averaged for every single combination. The averaged results from the individual simulations are utilised to train a radial basis function (RBF) surrogate model. More detailed information on surrogate models, including methods for training and testing, is presented in Section 4.3. In short, the surrogate model interpolates the scattered data to estimate the machine's results for any required load case. Inverter power limitations are taken into account in the model by restricting the DC-link voltage level and setting a current limit. The model yields all the characteristics of the axial flux machine necessary for further investigation like efficiency, currents, losses, etc. [19].
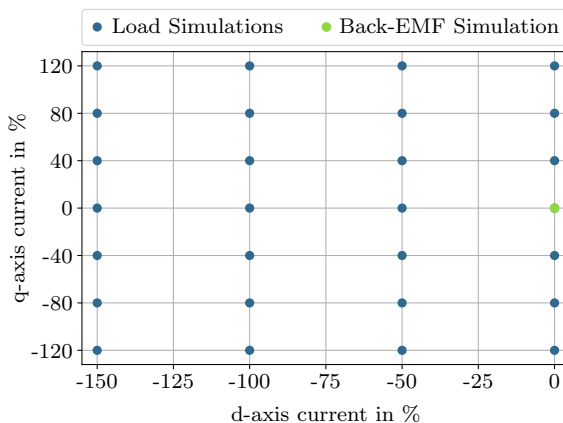

Figure 3.4: Computed grid of $d-$ and $q-$axis currents in percent of the nominal current

3.4 Extension for Air Gap Variation

A finite number of air gap widths is evaluated for a machine design using FEA. The motor model is then created separately for every air gap width. The machine's efficiency is derived and given as a function dependent on speed n, torque T and air gap δ

$$\eta = f(T, n, \delta) \tag{3.6}$$

The individual motor models are combined, by searching for the air gap with the highest efficiency for every operating point in the efficiency map of the studied machine. For the air gap width with the highest efficiency at the given condition, all necessary values (air gap width, currents, voltages, losses, power factor, etc.) are stored as the combined motor model. Another RBF model is then used to compute a function that yields the machine's efficiency at optimal air gap width

$$\eta_{opt} = f(T, n) \text{ at } \delta . \tag{3.7}$$

This means, that for every operating point defined by speed and torque, a specific air gap can be set to achieve optimal efficiency.

Fig. 3.5a shows an efficiency map created by the motor model for an example machine with an air gap width of 1 mm. It can be seen that the low-speed, high-torque region has a relatively high efficiency. This is to be expected, as the low air gap width results in a high rotor flux linkage and thus magnet flux (for which no current is needed) is the main contributor to the machine's torque. (cf. equation (2.9)).

Fig. 3.5d shows the efficiency map of the same motor with an air gap width of 10 mm. In this case, the rotor flux linkage is reduced due to the high reluctance of the air gap. The remaining rotor flux linkage is no longer sufficient to reach the desired torque value in the constant torque region and the efficiency in this region is decreased significantly. The upside, however, is that due to the decreased rotor flux linkage, the stator voltage vector is also decreased. This has the effect that less or even no negative direct axis current is needed to reach the high-speed operating points and therefore machine efficiency is significantly increased in that region.

The cases for air gap widths of 2 mm and 5 mm are depicted in Fig. 3.5b and 3.5c respectively. Fig. 3.5e shows the combined efficiency map of the variable air gap motor model, created by combining several static air gap models. It can be seen, that not only the efficiency, but also the operating envelope of the machine is increased substantially.
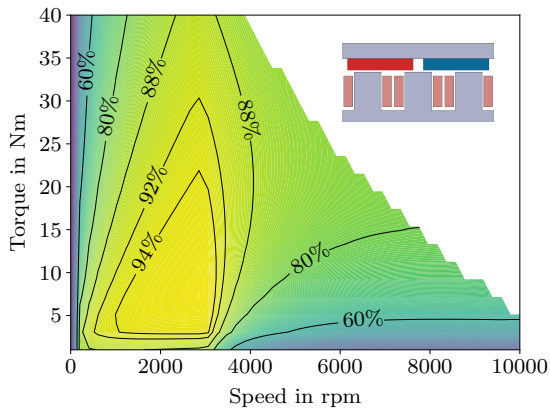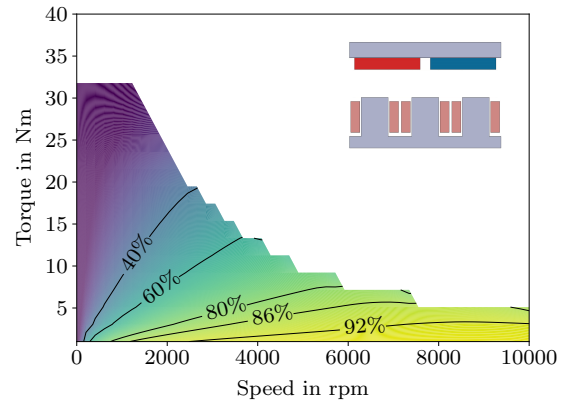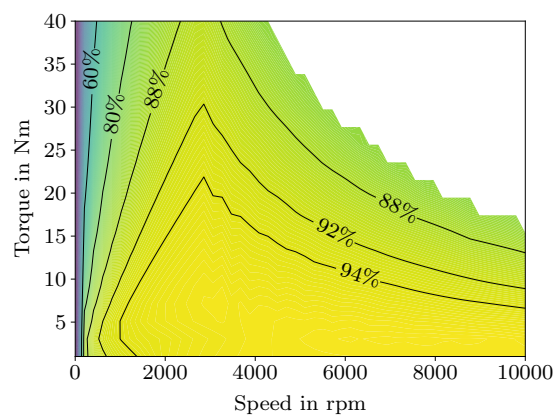
(a) Machine with 1 mm air gap width
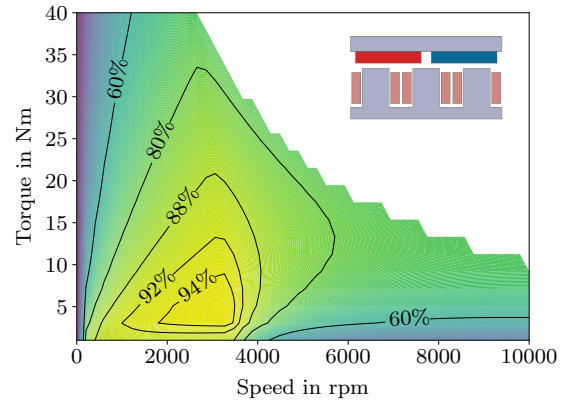
(b) Machine with 2 mm air gap width
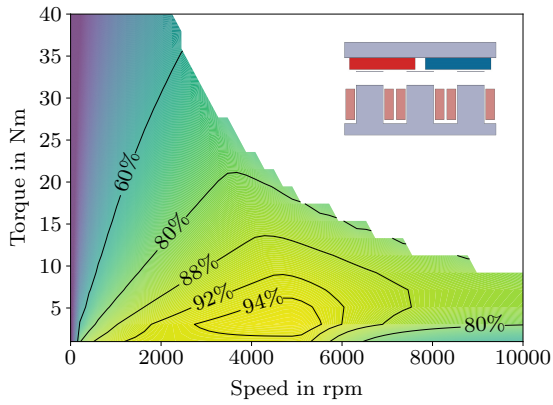
(c) Machine with 5 mm air gap width

(d) Machine with 10 mm air gap width

(e) Machine with combined air gaps

Figure 3.5: Efficiency Maps for a single machine at different air gaps

3.5 Driving Cycle Evaluation

Using the combined motor model, it is possible to calculate the machine's energy consumption for any driving cycle without requiring any additional finite element analysis. The driving cycles used here are specific for the student racing series, for which the traction drive is being designed. Two different cycles are used, one for the Formula Student Germany (FSG) and one for the Formula SAE Australasia (FSAE-A) racetrack.

Fig. 3.6a shows the speed-time diagram of the racecar for a flying lap of the FSG circuit. The maximum speed reached on the straights is limited to approximately 90 km/h while the minimum speed in the corners lies around 28 km/h. The root-mean-square (RMS) speed for this cycle is 60,8 km/h. The speed-time requirements for the car can be converted into speed-torque requirements for the motors using a vehicle model [8]. Due to acceleration, braking, and cornering, every wheel on a car experiences slightly different loads at any given moment during the lap. For this reason, speed-torque requirements for every single motor are derived through vehicle dynamics simulations. The speed-torque requirements for all motors during a lap of the FSG racetrack are shown in Figs. 3.6b and 3.6c. The RMS motor speed is 9810 rpm and the average RMS torque requirement is 16,0 Nm. Fig. 3.6d and 3.6e show torque over time for both sides of the vehicle for a specific part of the FSG driving cycle.

The speed-time diagram for the FSAE-A cycle can be seen in Fig. 3.7a. The maximum speed of 90 km/h is reached more frequently while the minimum speed is about the same with 28 km/h. The RMS speed is slightly higher at 66,4 km/h. Fig. 3.7b and 3.7c show the speed-torque requirements for a lap of this racetrack. The RMS motor speed is slightly higher at 10720 rpm and the average RMS torque is slightly lower than for the FSG cycle at around 14,7 Nm. Fig. 3.7d and 3.7e show torque over time for both sides of the vehicle for a specific part of the FSAE-A driving cycle.
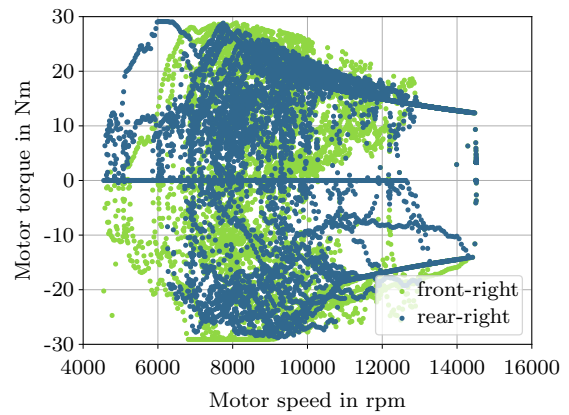
The flowchart in Fig. 3.8 depicts the full machine evaluation process described in this chapter. An investigation into the computation time and accuracy of this model, compared to three-dimensional FEA is performed in the upcoming Chapter 5.
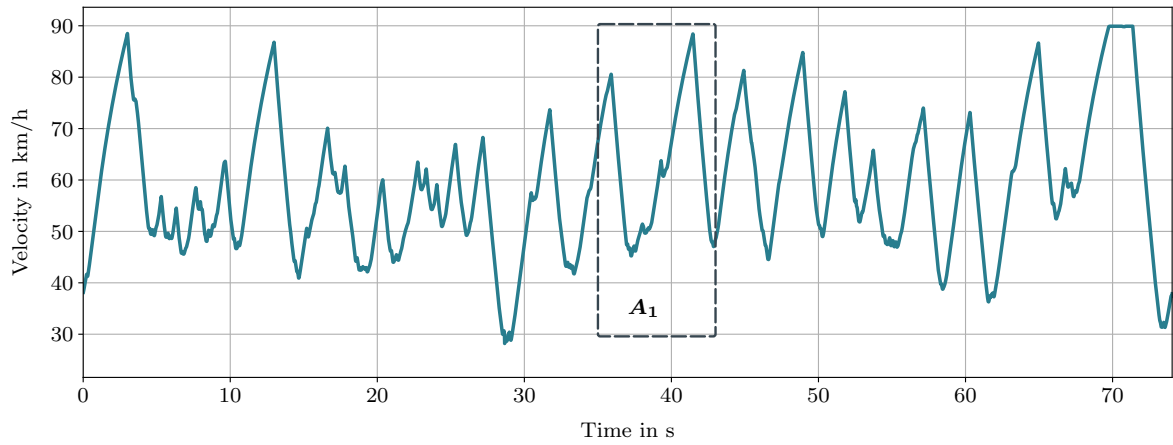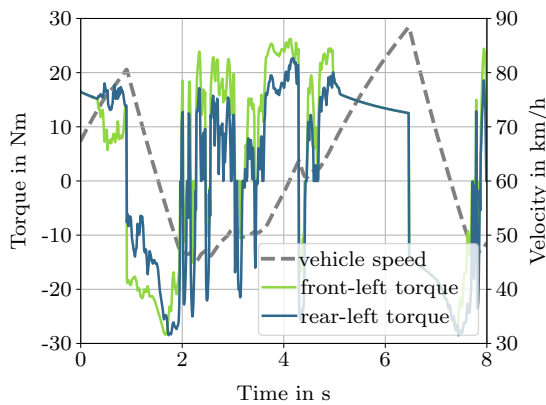
(a) Vehicle speed for the FSG racetrack
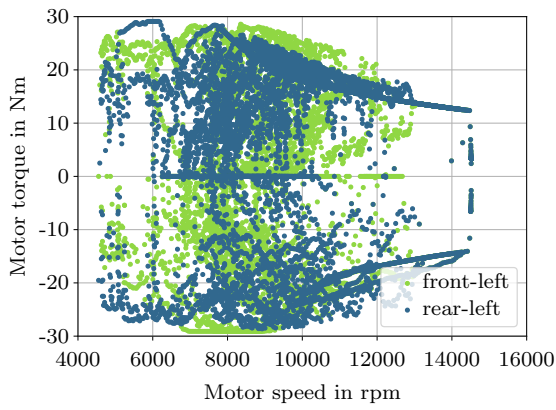
(b) Motor torque and speed for the left side of the vehicle

(c) Motor torque and speed for the right side of the vehicle

(d) Motor torque and vehicle speed over time for the left side of the vehicle and area A_1

(e) Motor torque and vehicle speed over time for the right side of the vehicle and area A_1

Figure 3.6: Vehicle speed and motor torque during the FSG driving cycle

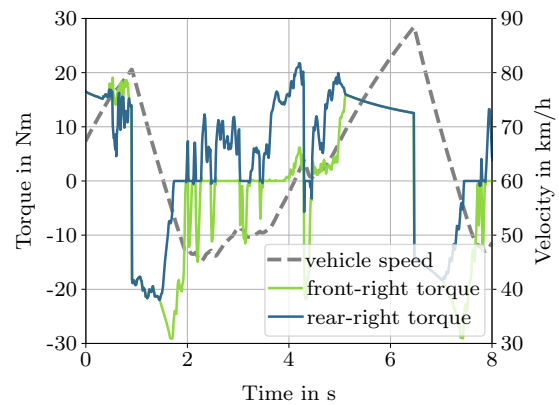(a) Vehicle speed for the FSAE-A racetrack

(b) Motor torque and speed for the left side of the vehicle

(c) Motor torque and speed for the right side of the vehicle
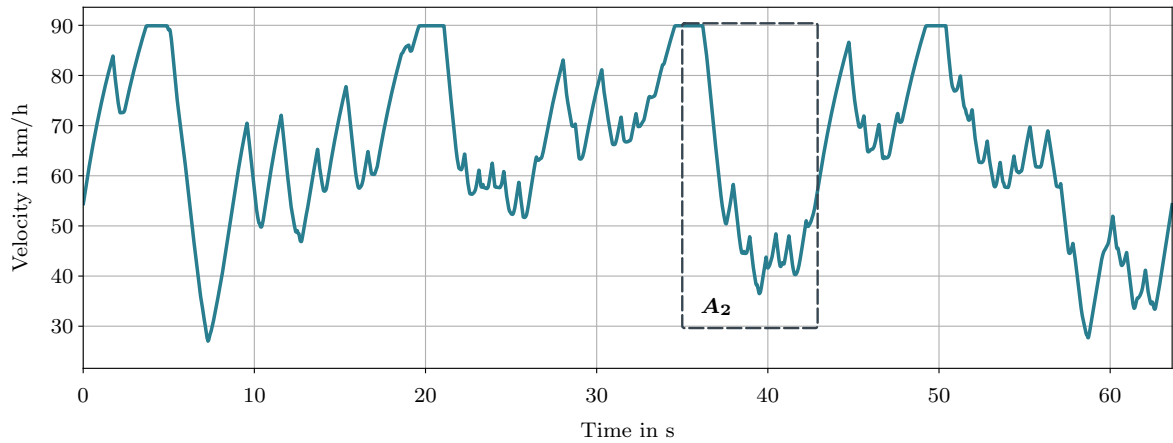

(d) Motor torque and vehicle speed over time for the left side of the vehicle and area A_2
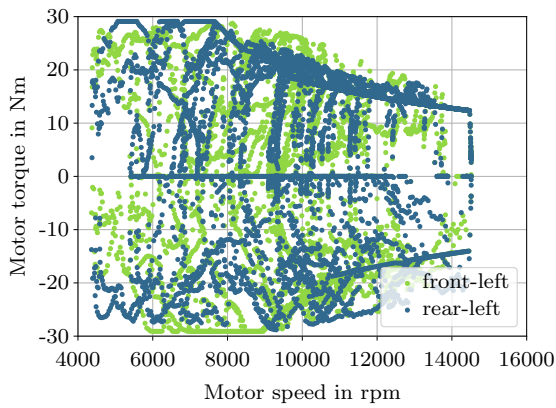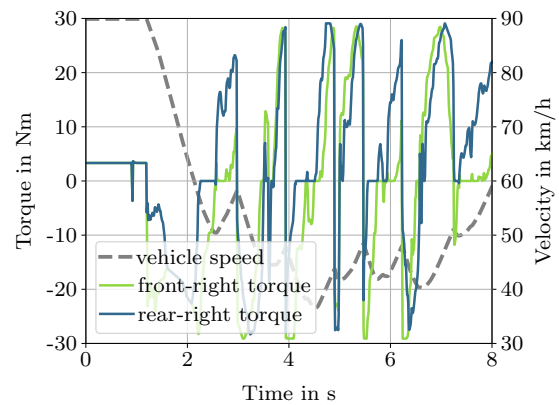

(e) Motor torque and vehicle speed over time for the right side of the vehicle and area A_2
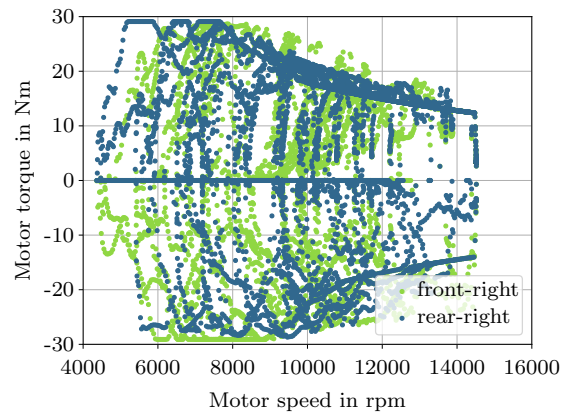
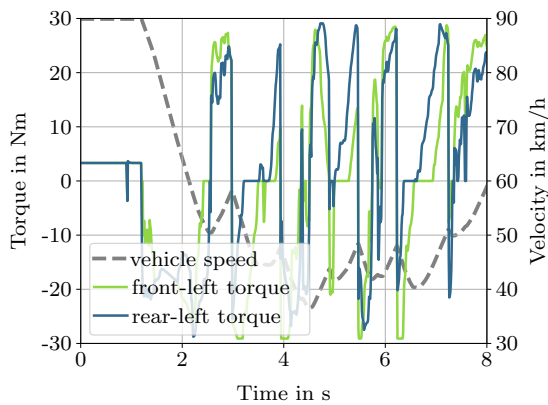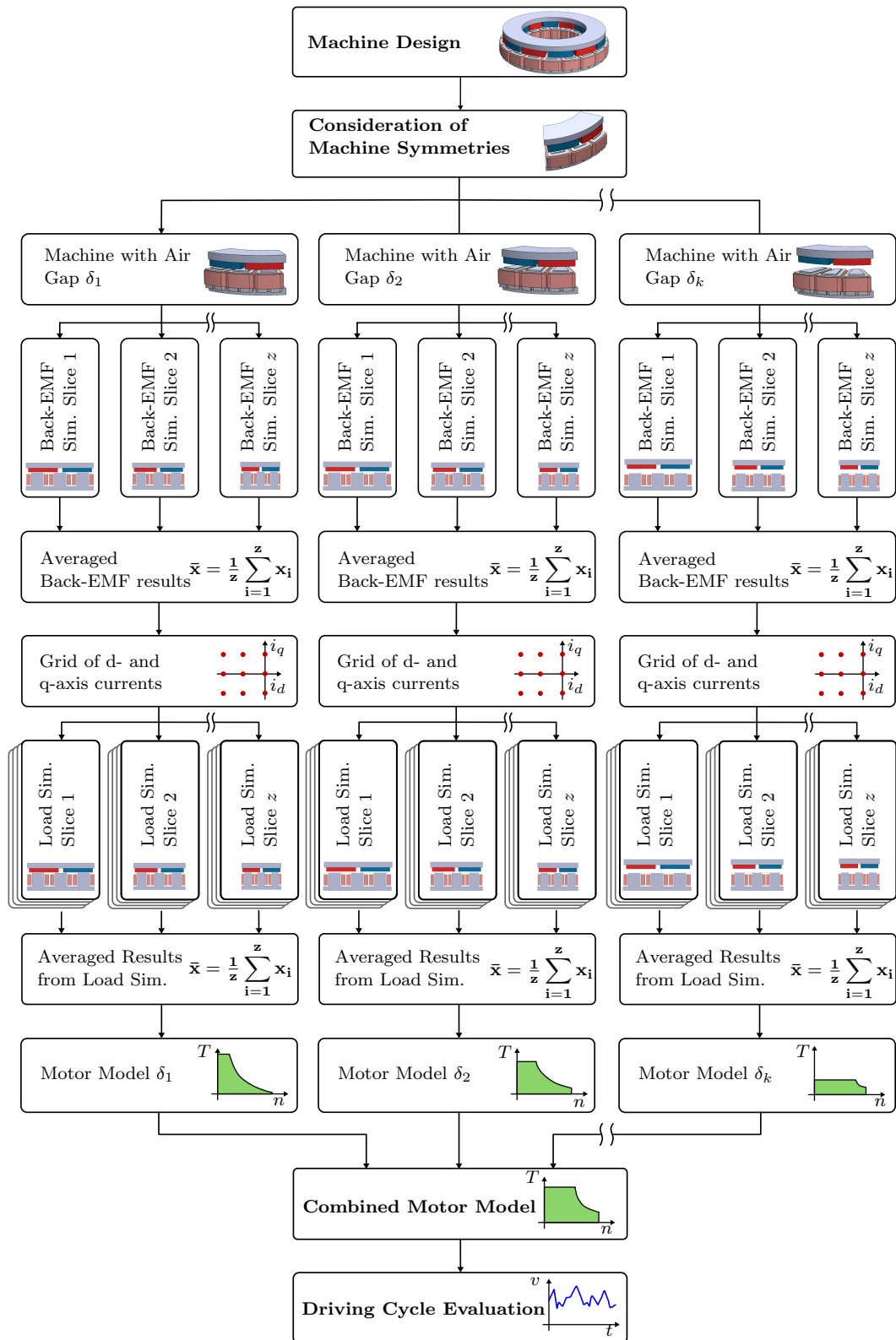Figure 3.7: Vehicle speed and motor torque during the FSAE-A driving cycle

Figure 3.8: Evaluation of a single machine design with z computation planes and k air gap widths

4 Design Scenario

4.1 Two Distinct Scenarios

Optimising the machine's geometry is essential to finding the most suitable design for a given application. Optimising an electric machine is a complicated task, as multiple variables impact the machine performance. Because of this, it is necessary to evaluate a significant number of designs, which should be done in a reasonable time.

Traditionally, electric machines have often been designed and optimised for a single operating point [12]. This kind of method of designing and optimising electric machines is fairly simple, but less suitable for the evaluation of variable air gap machines, especially when used as traction drives [20, 21].

To evaluate the modelling concept introduced in Chapter 3, two different design scenarios are presented and the results are compared in the following sections.

The first scenario utilises a very basic, single air gap, single slice model and is optimised for one operating point. The idea behind this scenario is to get a baseline design for a prototype motor that will be built and tested. This scenario is performed for two different machine topologies. The first has 18 stator slots and 12 magnet poles (18-12 machine) and the second has 12 stator slots and 10 magnet poles (12-10 machine).

Both machines have different benefits and drawbacks. For example, the 18-12 machine has considerably higher-order voltage subharmonics when compared to the 12-10 design. On the other hand, 12-10 machines typically have higher mass due to the necessity of thicker yokes. For this reason, both topologies are considered in the first design scenario.

The second scenario uses the multiple slice, variable air gap model with driving cycle evaluation described in Chapter 3. The results of this scenario will indicate how significantly the optimal machine designs from both optimisations differ and how much performance can be gained.

4.2 Requirements and Setup of the Optimisation

It is the goal to use the investigated machine as a traction drive for a racecar. To increase performance, the total mass of the vehicle should be reduced as much as possible. For this, there are two things to consider: The combined weight of the four machines on the car and the weight of the accumulator. Machines with higher mass may lead to lower energy consumption over the driving cycle, which means there is a lesser need for battery mass and, as a result, overall mass is reduced. This trade-off has to be balanced, which is the objective of the optimisation.

The material used for the rotor and stator core is Silicon-Iron (SiFe) electrical steel, specifically 20JNEH1200 by JFE Steel. The magnets are made from neodymium-iron-boron (NdFeB) N48SH by Arnold Magnetics. The stator coils will be wound onto a bobbin, in the simulation this is accounted for as an air gap between the core and coils. Further details about the used materials and the construction process can be found in the following Chapter 5.

The design variables with their respective limits are listed in Table 4.1 and are highlighted in Fig. 4.1. As the considered application as an in-hub traction drive, the maximum outer diameter including the end turns has to be constrained to 140 mm. For this reason, the calculated coil width and bobbin thickness are subtracted from the maximum outer diameter to get the core's outer diameter.

Table 4.1: Design variables used in optimisation

Variable	Description	Min	Max
h_{s}	slot depth in mm	12.5	19.5
h_{ry}	rotor yoke thickness in mm	3.5	6.5
h_{sy}	stator yoke thickness in mm	3.5	6.5
h_{m}	magnet thickness in mm	4.5	7.5
k_{ds}	split ratio $= \frac{d_{\mathrm{o,r}}}{d_{\mathrm{i,r}}}$	0.59	0.85
k_{sw}	slot width to slot pitch ratio $= \frac{w_{\mathrm{s}}}{\tau_{\mathrm{s}}}$	0.38	0.62
p_{p}	pole arc to pole pitch ratio $= \frac{\tau_{\mathrm{pa}}}{\tau_{\mathrm{pp}}}$	0.65	0.95
$d_{\mathrm{o,s}}$	outer diameter in mm	100	140

As mentioned above, the core's outer diameter $d_{\mathrm{o,r}}$ depends on the total outer diameter $d_{\mathrm{o,s}}$ and the slot width w_{s}

$$d_{\mathrm{o,r}} = d_{\mathrm{o,s}} - w_{\mathrm{s}} \ , \tag{4.1}$$

with the slot width defined by the slot pitch τ_{s} and the slot width to slot pitch ratio

$$w_{\mathrm{s}} = k_{\mathrm{sw}} \cdot \tau_{\mathrm{s}} \ . \tag{4.2}$$

The inner core diameter $d_{\mathrm{i,r}}$ is calculated with the split ratio as

$$d_{\mathrm{i,r}} = d_{\mathrm{o,r}} \cdot k_{\mathrm{ds}} \ . \tag{4.3}$$

The magnet pole arc τ_{pa} depends on the pole pitch τ_{p} and pole arc to pole pitch ratio

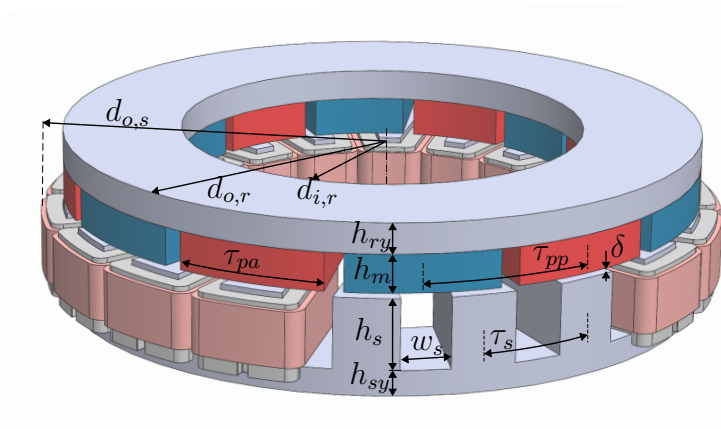$$\tau_{\mathrm{pa}} = \tau_{\mathrm{p}} \cdot p_{\mathrm{p}} \ . \tag{4.4}$$

Figure 4.1: Machine geometry and respective variables

4.3 Scenario 1: Optimisation for Static Air Gap and Single Operating Point

In the first design scenario, the machine's geometry is optimised for a single operating point and a static 1mm air gap width. The operating point is defined by setting a speed of 10000 rpm and q-axis current density of $40\,\text{A/mm}^2$. A surrogate model based optimisation method is chosen for this evaluation. The surrogate model creation and machine optimisation are explained in the following subsections.

4.3.1 Surrogate Model Setup

A surrogate model, also known as an approximation model, approximates the input-output response of a specific system. This significantly reduces the computation time of otherwise expensive simulation models, as no more FEA evaluations need to be performed [22]. However, it is necessary to generate an initial dataset with FEA to train and test the model. The surrogate model accepts the parameters from Table 4.1 as the input values and yields the machine's torque as well as core- and copper loss as output values.

Many different types of surrogate models are applied today, with some examples being polynomial response surface (PRS) models, kriging models, or radial basis function (RBF) models. RBF surrogate models are chosen for this problem as it has been observed that they show good quality for nonlinear problems [22].

A radial function utilises the Euclidean distance between a specific point and the sample point as its independent variable. If a model is constructed using linear superposition and utilises radial functions as its basis function, it is referred to as a radial basis function. For n sample points, an RBF proxy model is expressed as

$$f(\boldsymbol{x}) = \sum_{i=1}^{n} \beta_i \cdot \phi(r^i) \tag{4.5}$$

where β_i are the weight coefficients, $\phi(r)$ is a radial function and $r^i = ||\boldsymbol{x} - \boldsymbol{x^i}||$ is the Euclidean distance between the point $\boldsymbol{x}$ to be measured and the sample point $\boldsymbol{x^i}$. This means that the RBF surrogate model needs a certain number of sample points to accurately estimate the system's output [22]. This training data set is created using FEA simulation.

The first step in creating the training data set is to use a design of experiments (DOE) method to discretise the design space from Table 4.1 into a finite number of sample points which are required to be evaluated. This is done using the Latin Hypercube Sampling (LHS) method.

LHS is a sampling method that samples a multi-dimensional parameter space to ensure an even and representative coverage of the design space. The design space is divided into a pre-determined number of samples. In two-dimensional space, LHS would result in a latin square, where only one sample exists for every row and column in the grid.

Using LHS, 3000 different machine design samples were created and evaluated for one representative operating point using Ansys Maxwell and the linear machine model from Section 3.2.1. The operating point is defined by setting the speed and q-axis current density specified above. The machine's torque, core loss and copper loss are saved for every design. As a two-dimensional simulation is used to acquire the torque and loss data, the end-turn winding volume with its associated end-turn copper loss would not be included. To account for this, the end-turn volume is geometrically approximated and the end-turn are loss calculated using equation (2.18).

The optimisation is done for both the 18-12 and 12-10 machines. Both machine topologies' total loss over torque and mass are shown in Figs. 4.2a and 4.2b.
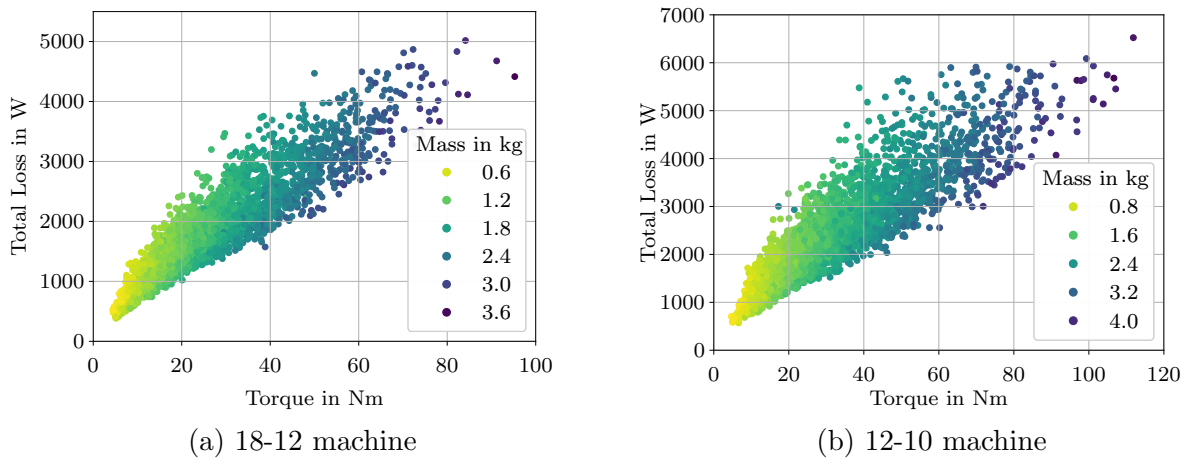

(a) 18-12 machine

(b) 12-10 machine

Figure 4.2: Simulation results for both machine types

With this set of training samples, the RBF model can be created. Before the surrogate model is used, its performance has to be evaluated. The position and number of sample points directly influence how well the model estimates an output. To check the correlation between the surrogate model and FEA output, some known sample points are compared

to the surrogate model's output. For this the sample set is divided into training data and test data. The achieved accuracy is quantified by calculating the Pearson correlation coefficient (PCC). The PCC measures the strength of the linear relationship between two samples and is defined for a sample size of n as [23]

$$r_{xy} = \frac{\sum_{i=1}^{n}(x_i - \bar{x})(y_i - \bar{y})}{\sqrt{\sum_{i=1}^{n}(x_i - \bar{x})^2}\sqrt{\sum_{i=1}^{n}(y_i - \bar{y})^2}} \tag{4.6}$$

with x_i, y_i being the individual sample points and $\bar{x}$, $\bar{y}$ the mean value of all samples. The correlation between FEA results and the predicted RBF model output is shown for two different RBF models in Figs. 4.3a and 4.3b respectively.

(a) RBF with 99.9 % correlation

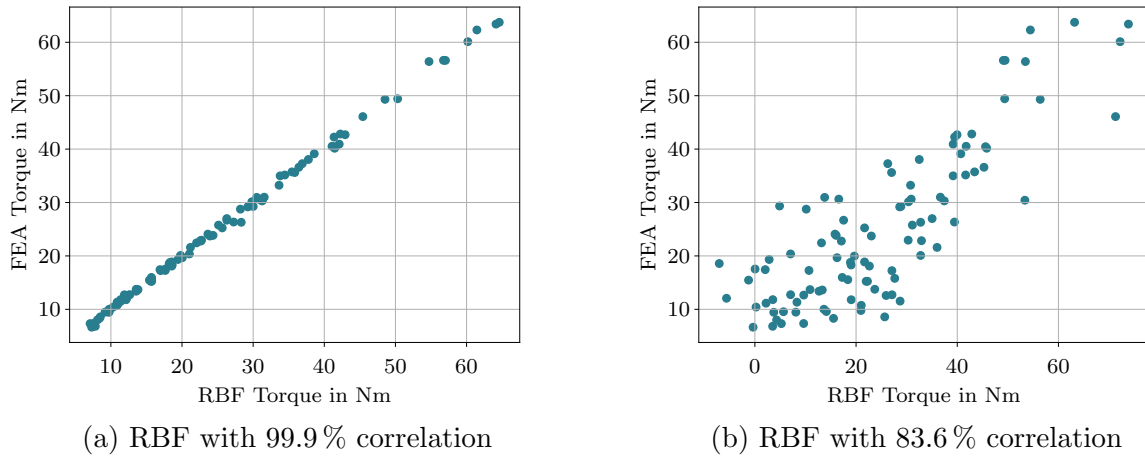(b) RBF with 83.6 % correlation

Figure 4.3: Correlation for two different RBF kernel functions

The same data set is used for both figures, the only difference is the different radial basis function used, when evaluating equation (4.5). In the case of Fig. 4.3a, a multiquadric function

$$\phi(r) = \sqrt{\left(\frac{r}{\varepsilon}\right)^2 + 1} \tag{4.7}$$

is used, while in Fig. 4.3b the radial function is the inverse multiquadric function

$$\phi(r) = \frac{1}{\sqrt{(\frac{r}{\varepsilon})^2 + 1}} \tag{4.8}$$

with constant ε. A suitable kernel function is chosen and the correlation is evaluated for both machine surrogate models over the entire sample set. The 3000 sample points

are divided into 30 disjointed subsets of equal size. The model is trained 30 times using all the subsets except one, which is the test set for calculating the correlation according to equation (4.6). The result of this cross-validation test for both machine topologies is shown in Fig. 4.4a and Fig. 4.4b respectively.

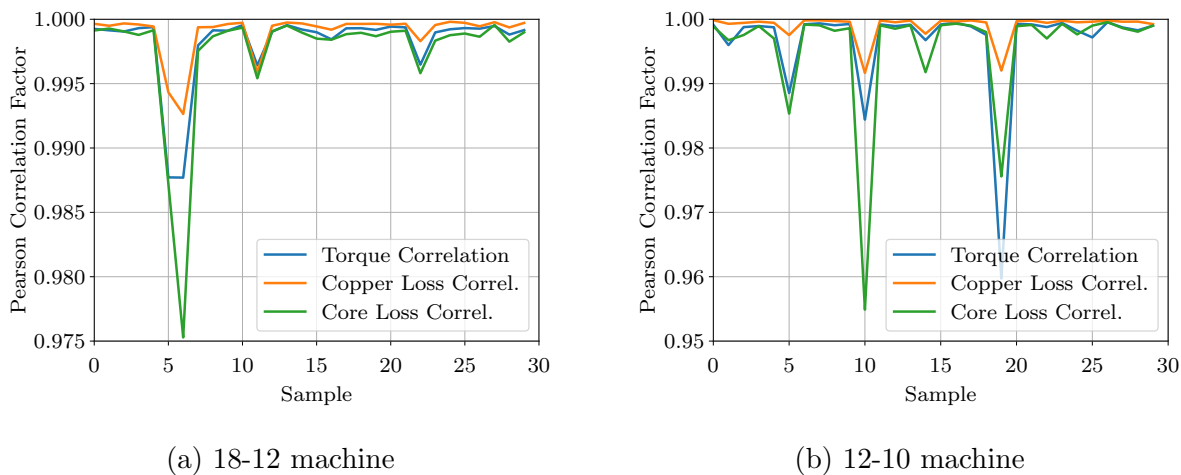

(a) 18-12 machine

(b) 12-10 machine

Figure 4.4: Surrogate model cross correlation for both machine types

The plots show that the results correlate well overall. However, one set in the case of the 18-12 and two sets in the case of the 12-10 machine do not correlate well. A reason for this could be that the sample values for those sets may lie further out on the edge of the interval. To diminish this problem, the parameter intervals for the optimisation are selected to be slightly smaller than the intervals used for training the surrogate model. The mean correlation over all sets is still approximately 99.7 % for both surrogate models, which means they can be used for optimisation.

4.3.2 SyMSpace Integration

The surrogate models are integrated into SyMSpace [24] for easier evaluation. The structure of the SyMSpace project is depicted in Fig. 4.5. The geometry of the machine is specified in the "Design Variables" tab. After training and testing the surrogate models for copper loss, core loss, and torque they are saved as separate Pickle files. These files are incorporated into SyMSpace in the "RBF Models" tab with a Python function.

The machine's mass is calculated by geometrically approximating the corresponding volumes with another Python function in the "Motor Mass" tab. The derivation of the volume approximation can be found in the Appendix. Finally, another Python function

is used to implement the cost function, taking the mass and losses as input parameters and returning a score, based on a cost function, for that specific machine.
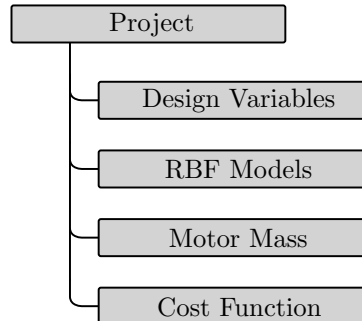

Figure 4.5: Structure of the SyMSpace project

4.3.3 Optimisation

With the surrogate models from the previous chapter, the machine's geometry can be optimised with almost no computational effort. A cost function is used to evaluate the machine's performance with a point-loss method. An ideal machine with zero mass and zero loss would result in zero points. A mass of $1\,\mathrm{kg}$ is equivalent to 1.5 points and $1\,\mathrm{kWh}$ of losses equals 8 points. Mass and loss are weighted to increase point loss for increasing mass or loss. The cost function is based on the mass-energy equivalence for Formula Student, proposed by Klink [25]. This means that the optimisation objectives are reduced to minimising point loss while maximising torque.
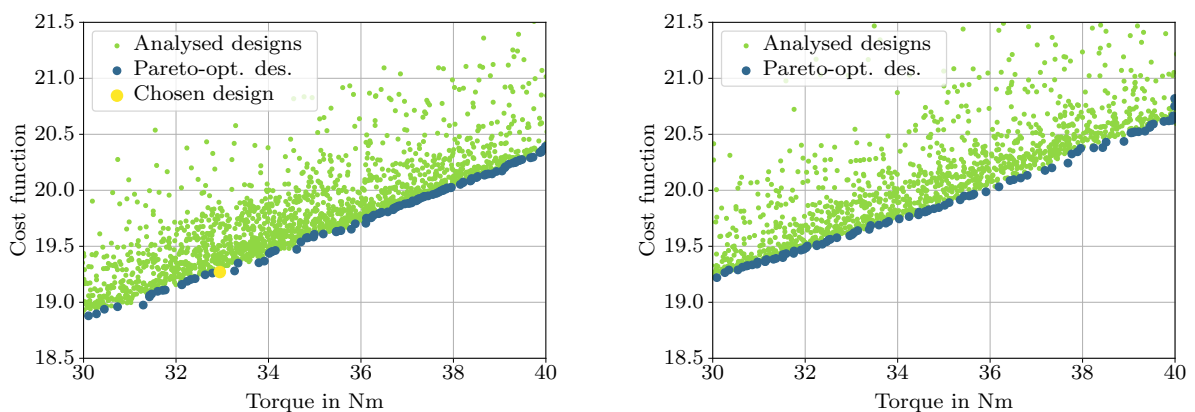
(a) 18-12 machine

(b) 12-10 machine

Figure 4.6: Optimisation results from Design Scenario 1

Figs. 4.6a and 4.6b show, that the 18-12 machine has a minor advantage over the 12-10 configuration. The goal is to select a design that produces around 30 Nm of torque. Previous work indicated that the single slice 2D LMMA overestimated torque by about 5 - 10 %. For this reason, an 18-12 machine design with approximately 33 Nm is chosen for the remaining studies and as the prototype design.

4.4 Scenario 2: Optimisation for Variable Air Gap and Multiple Operating Points

The second scenario utilises the proposed concept from Chapter 3. The machine is represented by three slices and analysed for five air gap widths at 1 mm, 2 mm, 5 mm, 10 mm, and 15 mm. Two different driving cycles are used in this scenario and each cycle has separate speed-torque requirements for every wheel. The objective is to minimise the racecar's energy consumption for both driving cycles and minimise the machine's mass.

4.4.1 SyMSpace Integration

The evaluation method from Chapter 3 is implemented in SyMSpace into two separate projects. The resulting project structures are highlighted in Fig. 4.8. The first project, here referred to as the sub-project, is constructed and processed in the following order: First, the machine's rated speed and torque values are set together with the inverter limitations and material definitions in the "Specification" and "Material" tab respectively. The machine's geometry and winding are specified in "Model Setup". Parameters like the $dq-$grid of relative currents, the number of steps in the simulation or the mesh parameters are defined in the "Simulation Setup" tab.

Separate 2D machine geometries are created by a LUA script for every considered slice diameter in "AFM Model". A back-emf simulation determines the position of the rotor fixed $d-$axis and $q-$axis and the flux linkage is derived for each slice. The nominal flux linkage is calculated by averaging the individual slice results in "Noload Simulations". The necessary quadrature axis current to achieve the desired nominal torque is then calculated by using equation 2.9.

Load simulations defined through the $dq-$grid of currents are performed for every slice and
the results of all slices are again averaged in the "Load Simulations" tab. All results are
gathered in the "Motor Results". The grid of averaged results from the load simulations
are used to fit an RBF model. Fig. 4.7 shows this grid of currents with contour lines of
the evaluated torque for an example machine. These results are interpolated and saved as
a file defined as the motor characteristics of the machine in the "Motor Characteristics"
tab. Finally, the machine's mass is calculated and some parameters like current density in
the windings or armature current load are evaluated in the "Masses" and "Performance
Parameters" tab respectively. The entire evaluation is performed for a specific air gap
width.

The second project is the superordinate project, where the design variables for the in-
vestigated machine are defined in "Design Variables". This project calls the sub-project
with the given set of variables and a specific air gap. The sub-project is evaluated and
the motor characteristics file is yielded to the superordinate project. This is done for the
air gap widths 1 mm, 2 mm, 5 mm, 10 mm and 15 mm. A Python function then takes
the motor characteristics files from all air gaps, looks for the value with the highest effi-
ciency for all operating points and creates a new motor characteristics function in "Motor
Characteristics Optimal". Some necessary parameters of the racecar are specified in "Car
Parameters". Finally, another Python Function is utilised to evaluate the energy con-
sumption of that machine for both driving cycles in "FSAE Driving Cycle" and "FSG
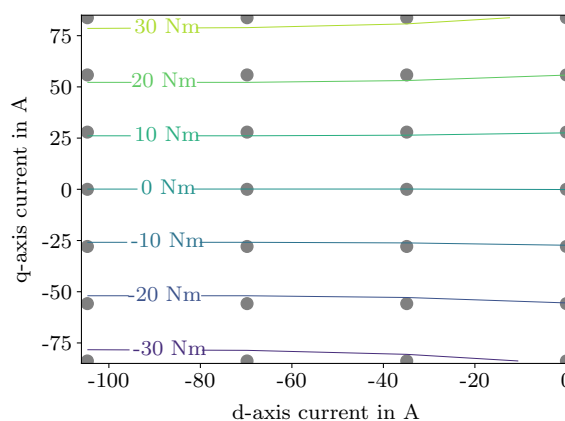Driving Cycle".

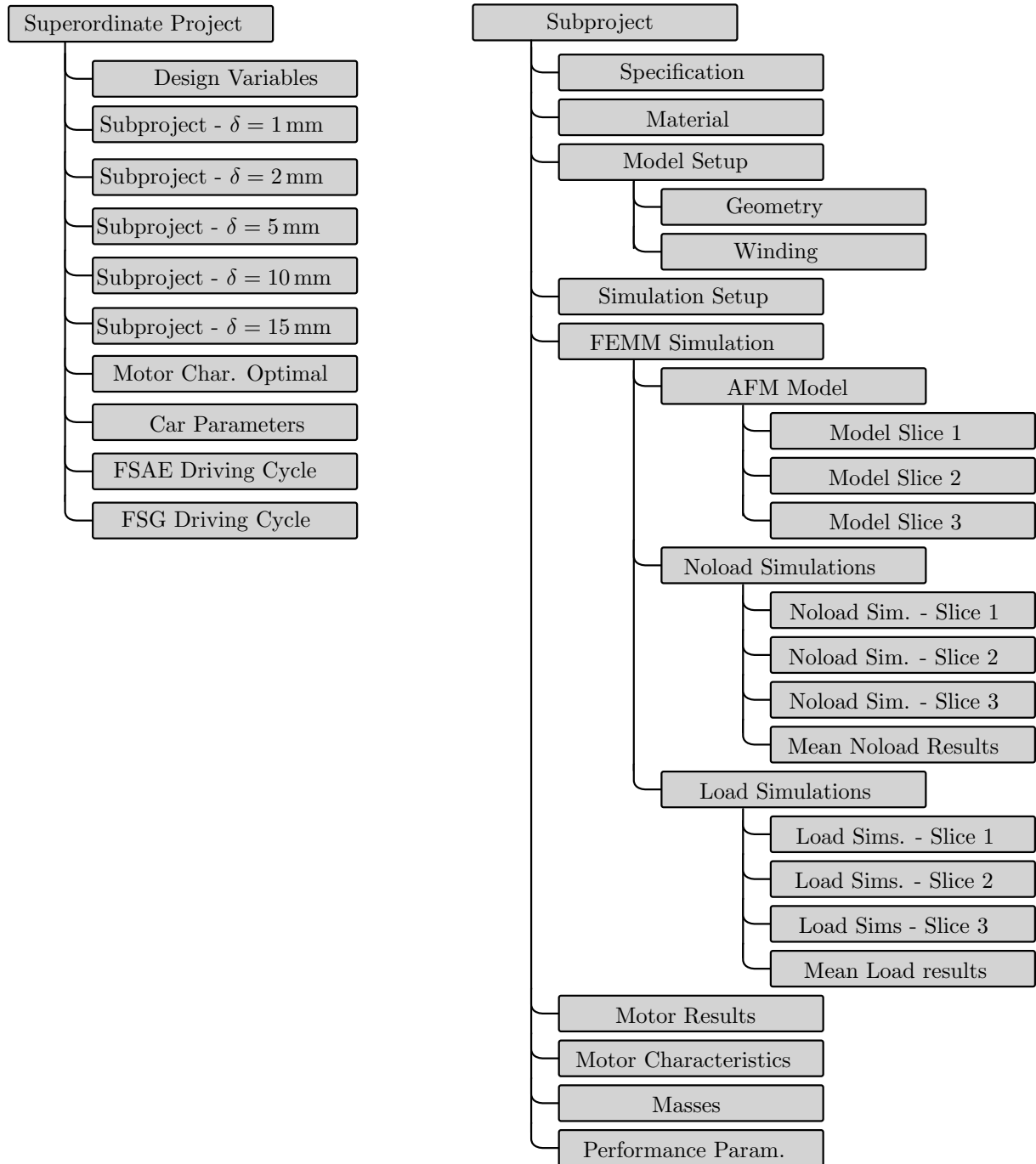Figure 4.7: Torque of an example machine for different d- and q-axis currents

Figure 4.8: Structure of the two SyMSpace projects

4.4.2 Optimisation

Due to the nature of the multi-objective optimisation, conflicting targets may exist. For this reason, a multiobjective evolutionary algorithm, in particular the differential evolution based coevolutionary multi-objective optimization (DECMO) algorithm [24], is chosen.

To speed up the optimisation process, tasks are parallelised and distributed on a computer cluster with 500 cores [21] using SyMSpace. Not all evaluated designs are valid as they do not satisfy the requirements of the given driving cycle. The evaluated, valid designs and Pareto-optimal results are shown in Figs. 4.9a, 4.9b and 4.9c.

The results from Figs. 4.9a and 4.9b are as expected: Higher mass machines follow a reduced energy consumption. Fig. 4.9c reveals that the optimal machines for both driving cycles do not significantly differ. The machine with the lowest energy consumption is selected for further investigation.

It should be noted that the results shown are for the case of no energy regeneration during braking. However, regenerative braking was considered in the optimisation but did not lead to any significant difference in the optimal machine design. The results for the case of full regenerative breaking can be found in the Appendix.
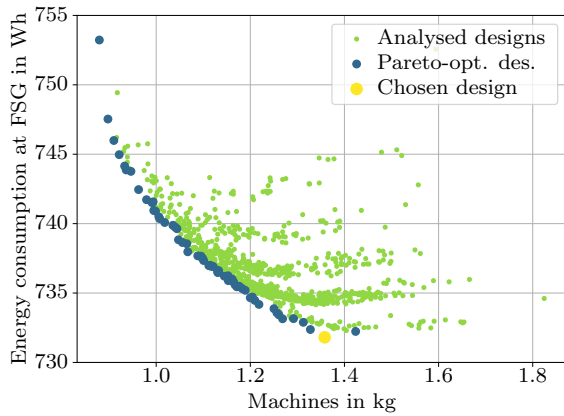
(a) Energy consumption over mass for the FSG cycle
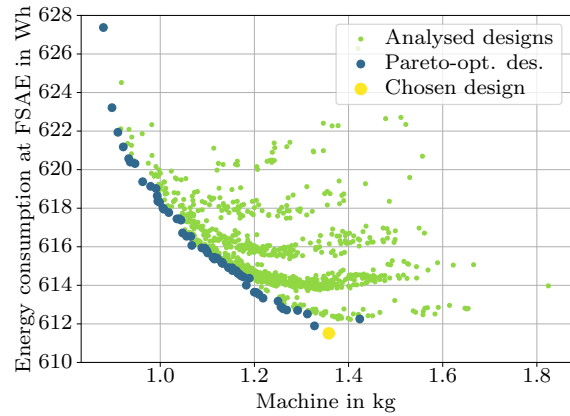
(b) Energy consumption over mass for the FSAE-A cycle
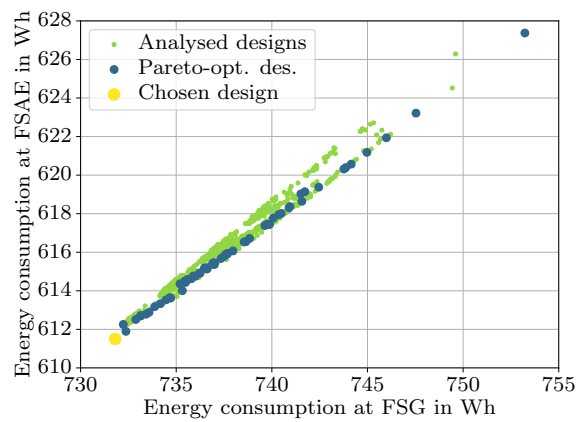
(c) Energy consumption for both driving cycles

Figure 4.9: Optimisation results from the second design scenario

4.5 Results and Comparison

The results for a chosen design from both scenarios are shown in Table 4.2. Both optimisations push the outer diameter to the upper limit of the interval. Rotor and stator yoke thicknesses are similar for both, as is the magnet volume.

A significant difference lies in the slot volume, due to increased slot depth and slightly higher slot width to slot pitch ratio. The most significant difference, however, lies in the larger split ratio. This increased split ratio results in a thinner, and therefore lighter machine with a mass saving of almost 20 % for the second optimisation.

Table 4.2: Optimisation variables and results

| Variable	Description	Min	Max	Opt. 1	Opt. 2
h_s	slot depth in mm	12.5	19.5	15	18.5
h_ry	rotor yoke thickness in mm	3.5	6.5	6	5
h_sy	stator yoke thickness in mm	3.5	6.5	6	6
h_m	magnet thickness in mm	4.5	7.5	7	7.5
k_ds	split ratio $= \frac{d_\mathrm{o,r}}{d_\mathrm{i,r}}$	0.59	0.85	0.71	0.81
k_sw	slot width to slot pitch ratio $= \frac{w_\mathrm{s}}{\tau_s}$	0.38	0.62	0.48	0.6
p_p	pole arc to pole pitch ratio $= \frac{\tau_{pa}}{\tau_{pp}}$	0.65	0.95	0.85	0.81
$d_\mathrm{o,s}$	outer diameter in mm	100	140	140	140
$d_\mathrm{o,r}$	core diameter in mm			130.6	127.9
δ	air gap in mm			1	1 - 15
m	machine's mass in kg			1.69	1.36

The efficiency maps for the machines from both design scenarios are shown in Figs. 4.10a and 4.10c respectively. The operating region in Fig. 4.10c is larger and the efficiency higher for a greater area than in Fig. 4.10a. It demonstrates how significant the difference between an air gap actuated machine and a static gap design can be. The comparison however is not fair, as the machine with mechanical rotor flux linkage control will always have an advantage. To account for this, Fig. 4.10b shows the efficiency map of the machine optimised for a static air gap but now analysed with air gap variation applied. Comparing Fig. 4.10c and Fig. 4.10b shows that the machine from Scenario 2 still has an edge over the static gap optimised design, even when air gap variation is incorporated.
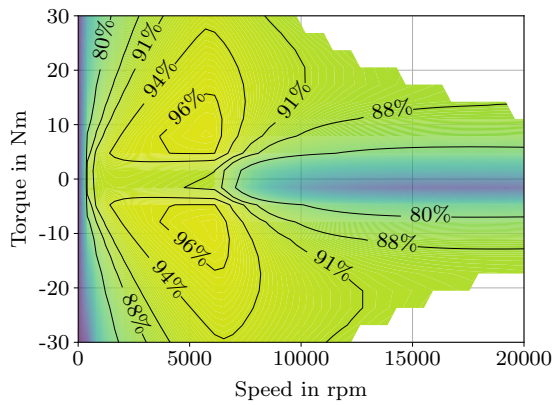
(a) Machine from Scenario 1 with $\delta = 1\,\mathrm{mm}$
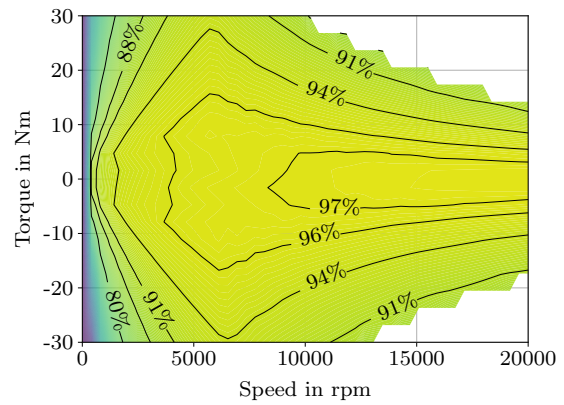
(b) Machine from Scenario 1 air gap variation applied
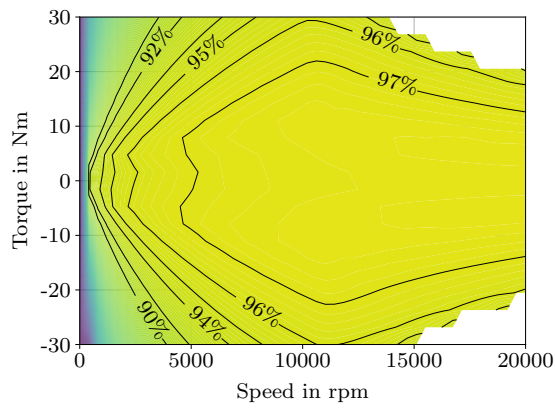
(c) Machine from Scenario 2

Figure 4.10: Efficiency Maps for the machines from both design scenarios

5 Validation Design

5.1 Design Selection

A single validation design is chosen, based on the results from Optimisation Scenario 1 from Section 4.3. Due to manufacturing reasons, a slightly different design was chosen.

The resulting geometry variables of the chosen design are highlighted in Table 5.1. Some changes were made to the magnets' grade and geometry for the prototype. The impact of these changes are evaluated and some additional, more in-depth investigations are performed in the following section.

Table 5.1: Geometry variables of the prototype machine

Variable	Description	Prototype
h_s	slot depth in mm	14
h_ry	rotor yoke thickness in mm	6
h_sy	stator yoke thickness in mm	5
h_m	magnet thickness in mm	7.5
k_ds	split ratio $= \frac{d_\mathrm{o,r}}{d_\mathrm{i,r}}$	0.63
k_sw	slot width to slot pitch ratio $= \frac{w_\mathrm{s}}{\tau_s}$	0.53
p_p	pole pitch to pole arc ratio $= \frac{\tau_{pa}}{\tau_{pp}}$	0.89
$d_\mathrm{o,s}$	outer diameter in mm	135.5
$d_\mathrm{o,r}$	core outer diameter in mm	126
$d_\mathrm{i,r}$	core inner diameter in mm	79.4
w_s	slot width in mm	9.5
m	machine's mass in kg	1.85

From this design, a prototype motor with mechanical flux linkage control is built and tested. The prototyping process is highlighted and the prototype machine is tested under different conditions and air gap widths.

5.2 Further Investigations for the Selected Design

5.2.1 Effect of Magnet Grade and Geometry

The magnet material was changed from N48SH to N45UH due to supply availability. The main difference between the two magnet grades is a slightly lower nominal remanence of $1.35\,\text{T}$ instead of $1.39\,\text{T}$ and a slightly lower nominal coercivity of $1023\,\text{kA/m}$ instead of $1038\,\text{kA/m}$. The resulting efficiency map of the prototype machine with the new magnets for an air gap width of $1\,\text{mm}$ is shown in Fig. 5.1a. The red markers are operating points used later in this chapter. A comparison of the simulated efficiency maps of the machine for both magnet types shows that the reduction of magnet grade has very little effect on the machine's performance. For rotor speeds between 0 and $2000\,\text{rpm}$ and a torque range of 10 to $30\,\text{Nm}$, the efficiency of the machine is decreased by approximately $1\,\%$. In the high speed and low torque area, the efficiency is increased by about $2\,\%$. However, this has no benefit, as the efficiency in this area is increased through air gap actuation anyway. The efficiency map for the prototype machine under consideration of air gap variation is depicted in Fig. 5.1b.
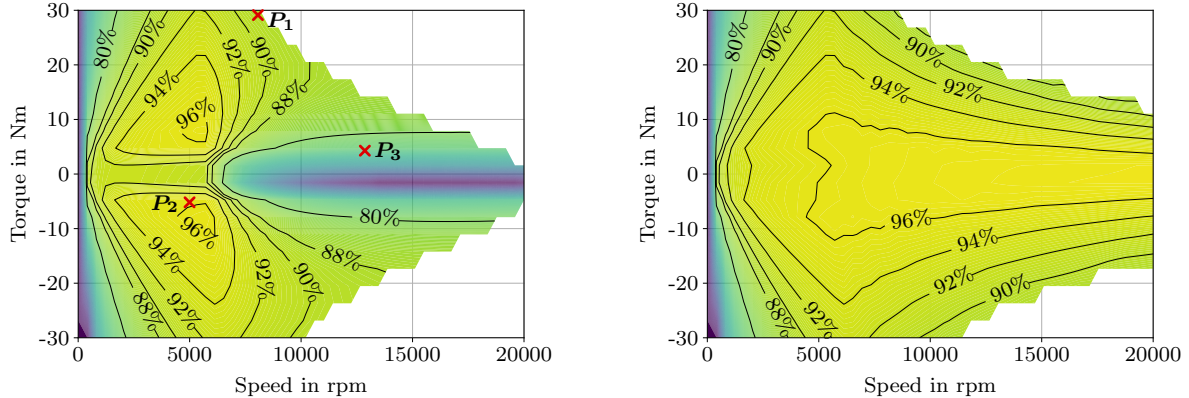
(a) Efficiency map of the prototype motor for the minimum air gap width of $\delta = 1\,\text{mm}$

(b) Efficiency map of the prototype motor for variable air gap width

Figure 5.1: Simulated efficiency maps of the prototype motor

The magnet shape was also changed slightly for future research purposes at Monash University. Fig. 5.2a shows the original magnet shape and Fig. 5.2b shows the magnet shape used for the prototype motor. The magnets' inner and outer edges are no longer rounded to follow the shape of the yoke. Instead, the edges are flat which results in the magnets sticking out over yoke on the inner and outer diameter. Due to the difference in

shape, the magnet volume increases by approximately $6.5\,\%$. As this change in geometry cannot be accounted for in 2D FEA, a 3D simulation is performed.

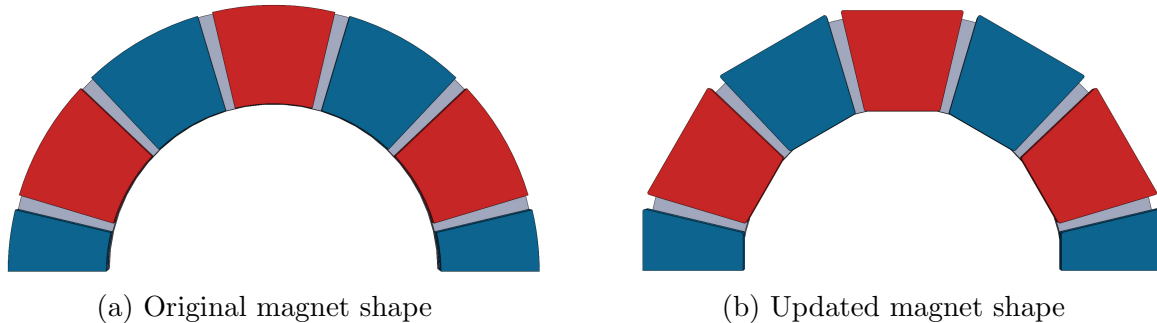(a) Original magnet shape   (b) Updated magnet shape

Figure 5.2: Different magnet shapes on a rotor

Due to the computational cost of three-dimensional FEA simulations, the evaluation is performed for only one operating point by setting a speed of $8000\,\text{rpm}$ and a $q-$axis current density of $38\,\text{A/mm}^2$. This results in the operating point P_1 shown in Fig. 5.1a. Through the increase of the magnet volume, the machine's output torque increases from $29.0\,\text{Nm}$ by $1.4\,\%$ to $29.4\,\text{Nm}$ for this operating point.

5.2.2 Evaluation of Computation Times and Accuracy

As described in Chapter 3, characterising axial flux machines based on three-dimensional FEA delivers more accurate results than 2D simulations, at the cost of lengthy evaluation times. A single 3D evaluation of the chosen design takes about 900 seconds for one electrical period, while a single 2D simulation only takes around 20 seconds

For the same speed and current density to achieve operating point P_1, the error in torque between the 3D model and the 2D LMMA models is calculated. For a fair comparison, the 3D simulation is performed with the new magnet material but with the original magnet shape from Fig. 5.2a. Table 5.2 shows the simulated torque of the 3D model and the 2D models with different slice numbers. The error between the single slice Linear Motor Modelling Approach and the 3D model is $5.0\,\%$. Using a quasi-3D model with three slices, this error is reduced by 30 percentage points to $3.5\,\%$.

The investigated machine design uses trapezoidal magnets, where the geometry does not change significantly along the radius. The effect of quasi-3D modelling is expected to be more significant for magnet shapes that change considerably over the radius, e.g. when considering triangular-shaped magnets. [19, 26]

Table 5.2: Torque output for different FEA configurations

Model	Torque in Nm	Diff. in %
3D	28.99	0.00
1 Slice	30.52	5.01
3 Slices	30.04	3.49
5 Slices	30.00	3.38
10 Slices	29.99	3.34

5.2.3 AC Loss Evaluation

As described in Section 2.2.3, alternating current losses appear in the presence of a time-changing magnetic field. In the case of conductors, the time-changing magnetic field induces eddy currents which lead to skin and proximity effects, resulting in additional loss.

Non-ideal sinusoidal flux distribution results in harmonics being present in the field of an electric machine. These harmonics induce eddy currents in the rotor, leading to AC magnet loss, which is dominantly present in high-conductivity materials like neodymium-iron-boron (NdFeB).

To evaluate the AC winding losses for the prototype motor, the individual conductors are modelled in Ansys Maxwell. The individual conductors are defined as solid objects and the eddy current effects are evaluated. The resulting FEA model is provided in Fig. 5.3. Different methods of calculating AC winding losses in axial flux PM machines are presented in the paper by Taran et al. [27].
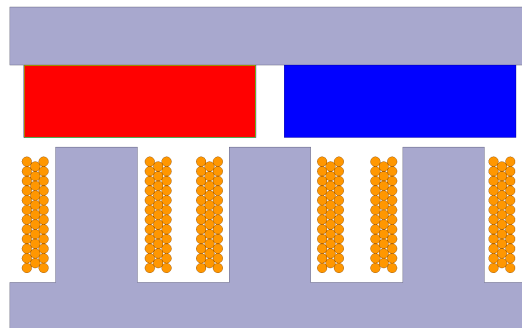

Figure 5.3: FEA model for simulation of eddy currents

The AC magnet and winding losses for the prototype design and an unsegmented magnet are evaluated for the same operating point P_1 defined by $q-$axis current density and rotor speed as above and an air gap range of one to ten millimetres. The DC copper loss for this operating point is approximately $790\,\mathrm{W}$, the AC loss adds an additional $350\,\mathrm{W}$ to the DC copper loss. The AC magnet loss is around $700\,\mathrm{W}$.

The results shown in Fig. 5.4 are normalised to a $1\,\mathrm{mm}$ air gap width. The AC winding losses reduce by about $17\,\%$ at an air gap of $10\,\mathrm{mm}$. The AC magnet losses decrease very quickly to a value of only $10\,\%$ at a $5\,\mathrm{mm}$ air gap. One reason for this is likely the very thick magnets ($7.5\,\mathrm{mm}$), together with the low permeability and high conductivity of NdFeB materials.
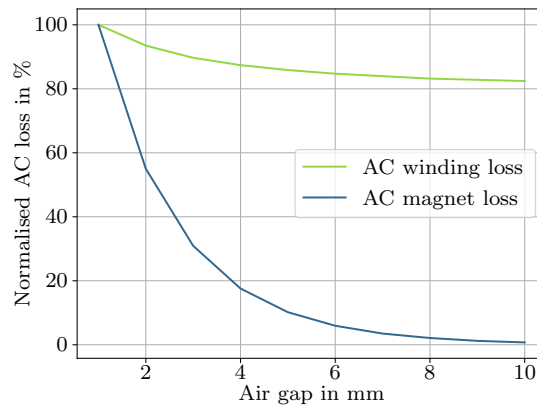
Figure 5.4: AC losses for different air gap widths

AC magnet losses can also be reduced by segmenting the magnet (cf. Section 2.2.3). Each magnet used for the prototype motor is made up of 14 segments (Fig. 5.5). 3D FEA shows that the AC magnet losses are reduced by more than $90\,\%$ through magnet segmentation. However, this many segments make the NdFeB magnets very expensive.

Figure 5.5: Segmented magnet used in the prototype motor

5.2.4 Axial Attraction Force

As described in Section 2.4, the distinct shape of single-sided axial flux machines results in a high axial attraction force acting between the rotor and stator. This force does not contribute to torque and can pose challenges, as the bearings have to deal with a high load. This leads to increased wear and can result in premature failure.

An investigation into the axial attraction force for different air gaps is performed, the results are shown in Fig. 5.6 for the machine with no load. Equivalent to the flux linkage, the attraction force decreases with increasing air gap width.

The axial force reaches more than $2000\,\mathrm{N}$ at an air gap width of $1\,\mathrm{mm}$ and halves at approximately $4\,\mathrm{mm}$. At an air gap width of $15\,\mathrm{mm}$, only a very small axial force is left. Equation (2.34) shows, that the force is inversely proportional to the air gap width squared.
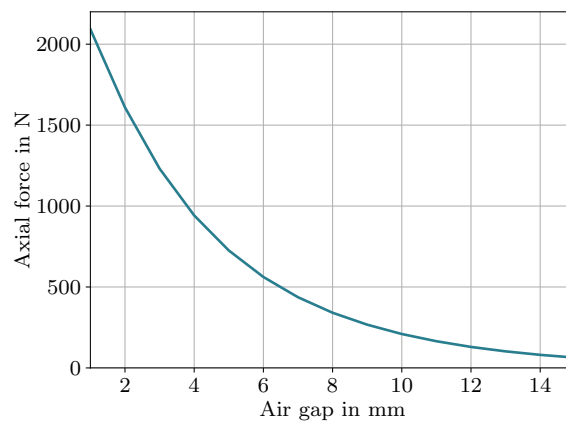
Figure 5.6: Axial attraction force for increasing air gap width

The attraction force can also be manipulated with direct axis current. As described in Chapter 2, the d-axis is aligned with the permanent magnet's flux vector. Assuming no saliency, the d-axis current does not produce any torque. However, it does affect the magnet flux linkage, which enables field weakening. For this reason, d-axis current also directly impacts the axial attraction force. Fig. 5.7 shows the axial attraction force for different d-axis current densities with a logarithmic scaling of the current. From equation (2.34) it is clear that the force is proportional to the current squared.
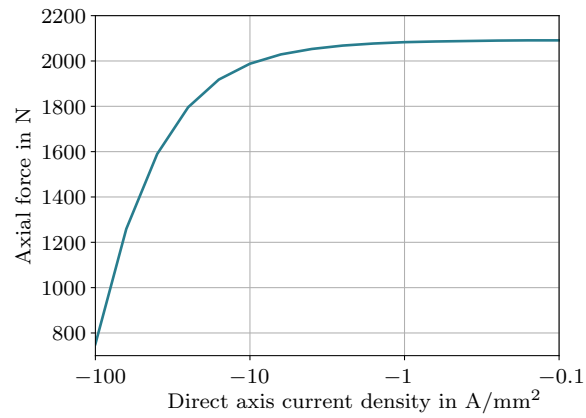
Figure 5.7: Axial attraction force over negative direct axis current density

5.2.5 Air Gap for Optimal Efficiency

An investigation of the air gap width to achieve optimal efficiency leads to the results shown in Fig. 5.8. The air gap width is varied from 1 mm to 15 mm and the efficiency for the entire operating region is derived. Simulation results show that for the given design, the maximum air gap width, where an increase in efficiency can be observed is 13 mm.
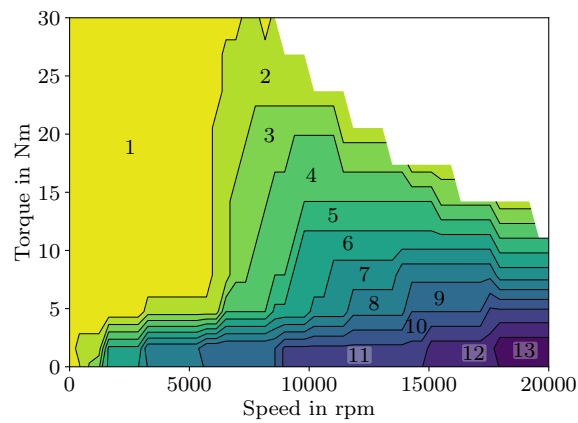

Figure 5.8: Air gap width to achieve optimal efficiency

5.2.6 Air Gap Interpolation

The machine evaluation process described in Chapter 3 combines the individual motor models to create a single motor model for all air gaps. The model however only considers air gaps that have been evaluated by FEA. This means the optimal air gap for the machine could only be $1\,\mathrm{mm}$, $2\,\mathrm{mm}$, $5\,\mathrm{mm}$, $10\,\mathrm{mm}$ or $15\,\mathrm{mm}$. However, the optimal air gap for a given operating point could lie somewhere between these values. Being able to consider this would greatly increase the quality of the machine evaluation.

An idea to incorporate this is to train an RBF model that interpolates the efficiency between the evaluated air gaps. The assumption was, that five computed points would be enough to fit a function. This fact, however, turned out not to be true. Fig. 5.9a and 5.9b show the machine's efficiency for two different operating points and for the air gap widths stated above. One operating point has a speed of $5000\,\mathrm{rpm}$ and a torque of $-5\,\mathrm{Nm}$. The other operating point is at $13000\,\mathrm{rpm}$ and $2\,\mathrm{Nm}$. Both operating points are highlighted in Fig. 5.1a as P_2 and P_3 respectively. Different RBF kernel functions are tested, but the interpolation does not yield any sensible results. The following figures show the RBF model with a multiquadric function (equation (4.7)), a thin plate spline function

$$\phi(r) = r^2 \cdot \log(r), \tag{5.1}$$

and a linear kernel function

$$\phi(r) = r \ . \tag{5.2}$$

Using more than five computed points for training the model should deliver better results. For this reason, the machine was evaluated with air gap widths from $1\,\mathrm{mm}$ to $15\,\mathrm{mm}$ in steps of $1\,\mathrm{mm}$. The results for the same operating points but with fifteen computed points can be seen in Fig. 5.9c and 5.9d.

One problem however persists. As described in Section 4.3, the RBF model is good at interpolation, but loses accuracy when approximating values at the outer limit of the interval. For this reason, the edges are extended with points along a linear function, with the gradient depending on the two outermost values. The RBF model is then trained with the extended values, the results are shown in Fig. 5.9e and 5.9f. Based on these results, the RBF model could be used, the number of necessary computation points however makes it impractical.
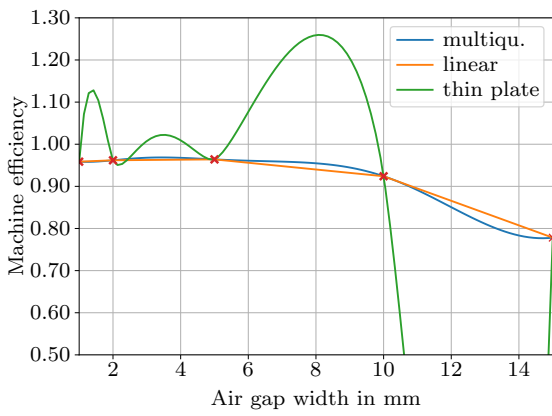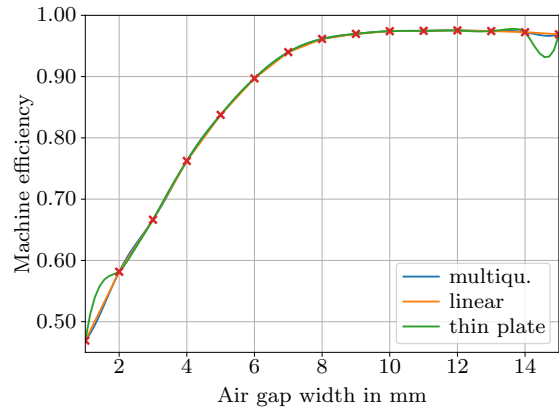
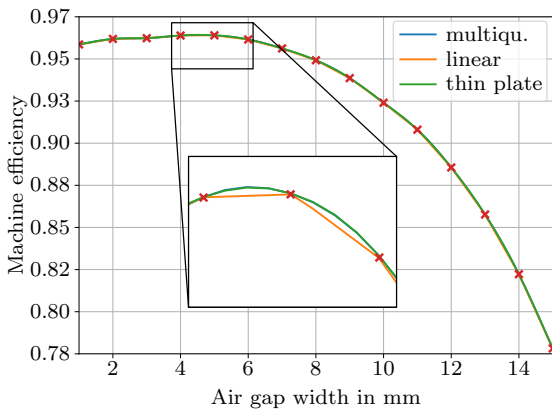(a) Poorly correlating RBF model for operating point P_2
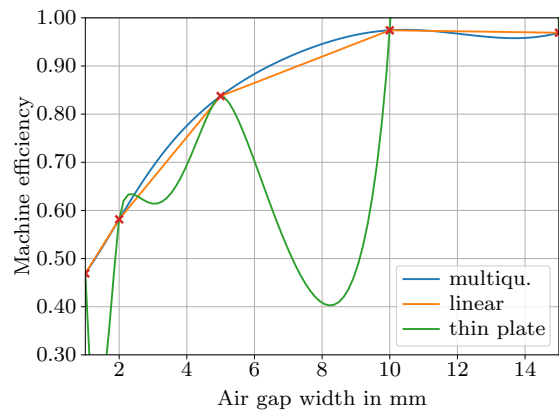
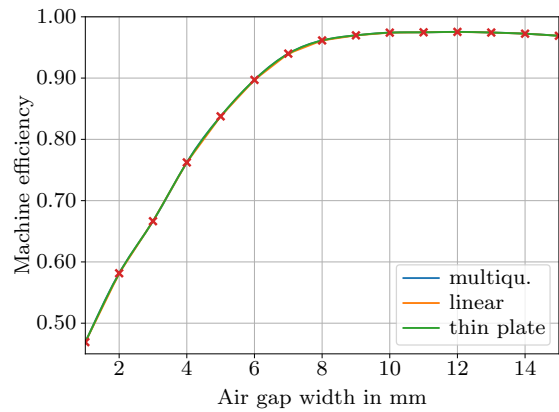(b) Poorly correlating RBF model for operating point P_3
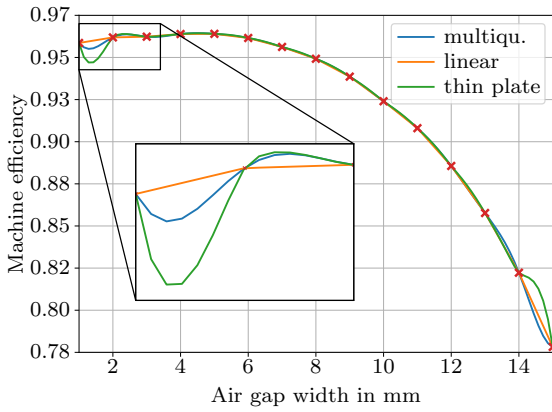
(c) RBF model with bad correlation at the edges for operating point P_2

(d) RBF model with bad correlation at the edges for operating point P_3

(e) RBF model with good correlation for operating point P_2

(f) RBF model with good correlation for operating point P_3

Figure 5.9: Efficiency over air gap width for different RBF models and operating points

5.3 Prototype Motor

The process of designing electric machines is heavily dependent on the use of simulations. However, simulations are based on a set of mathematical rules and assumptions, that may or may not be true in a real-world scenario. For this reason, prototyping is an essential step to verify the accuracy of simulations. The following sections describe the necessary steps to build a prototype axial flux machine with a mechanical air gap variation system.

5.3.1 Winding Arrangement

The prototype machine has 18 coils on the stator, which results in six coils per phase. There are four different winding arrangements for such a motor. All six coils could either be connected in series (6S) or parallel (6P). There could also be two or three parallel paths (3S2P and 2S3P respectively), with the other coils being in series. Normally, these phase connections of a motor are done inside the stator housing during the manufacture of the motor. However, this does not allow any change in the winding arrangement after assembly.

For this reason, it was decided that all the coil and phase connections would be done on the outside of the motor. This has some benefits for testing the prototype, as different winding arrangements can be tested. Another benefit is that it should be possible to detect any rotor eccentricities, as the induced voltage of every coil can be measured separately. If a part of the rotor rotates past the stator at a smaller axial distance, the induced voltage will increase, as it is inversely proportional to the air gap width.

However, the number of turns and therefore the copper wire diameter depends on the winding configuration. For this reason, a 3S2P design with a star connection is chosen as the baseline configuration. The different winding arrangements from SyMSpace are illustrated in Figs. 5.10 to 5.13.

The 3S2P winding arrangement results in a necessary copper wire diameter of 1.03 mm and 34 turns per coil. The derivation of these values can be found in the Appendix.
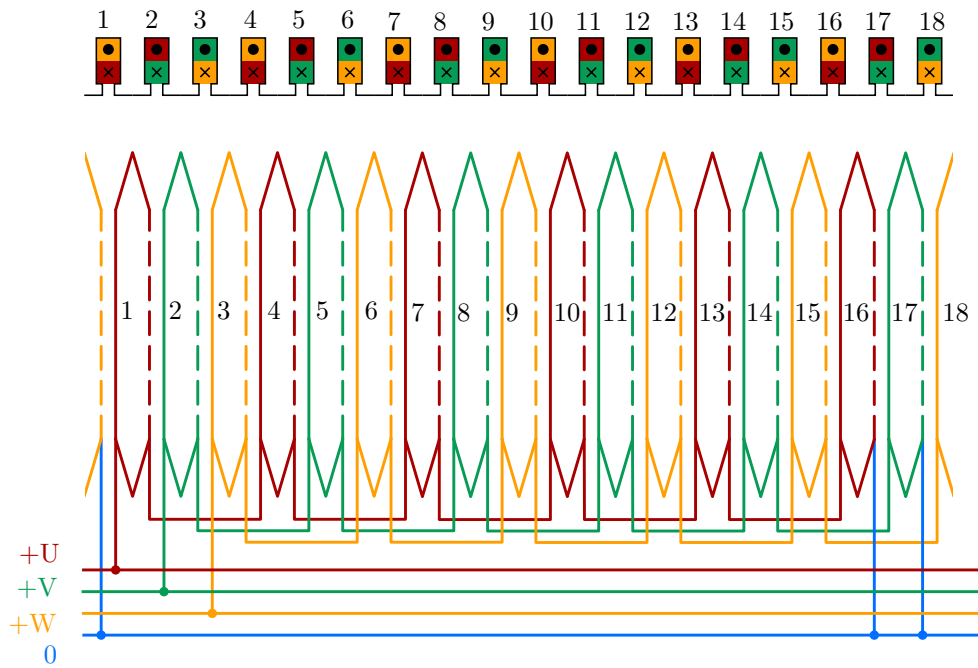
Figure 5.10: 6S winding arrangement for an 18-12 machine
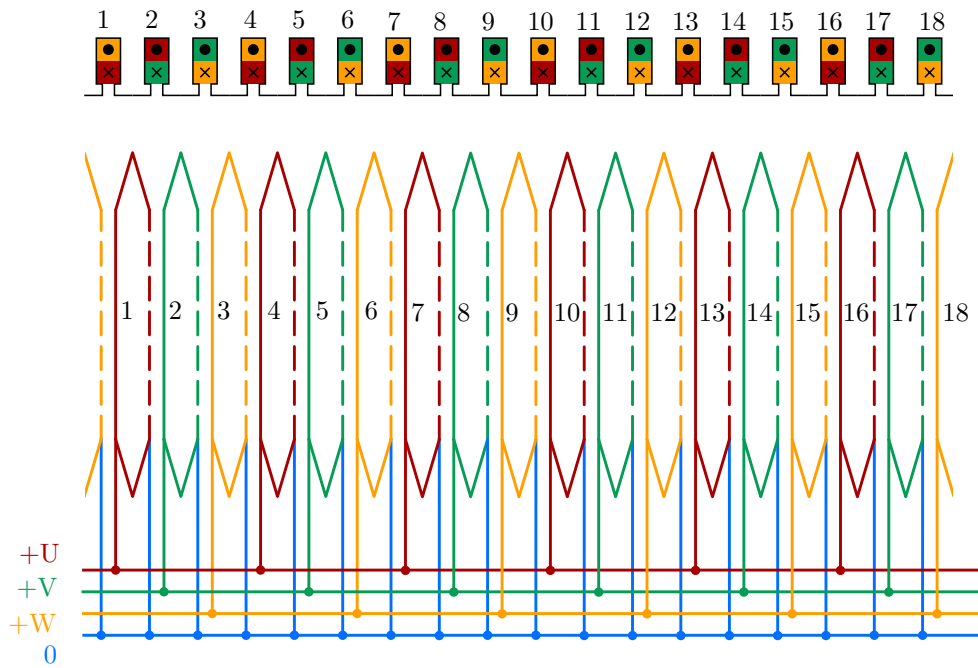

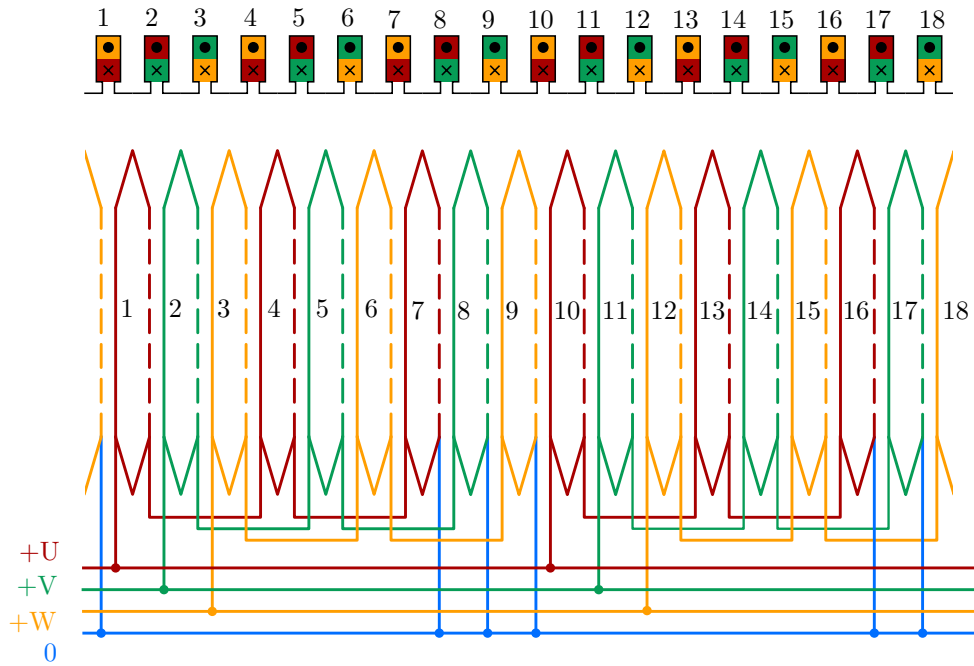Figure 5.11: 6P winding arrangement for an 18-12 machine

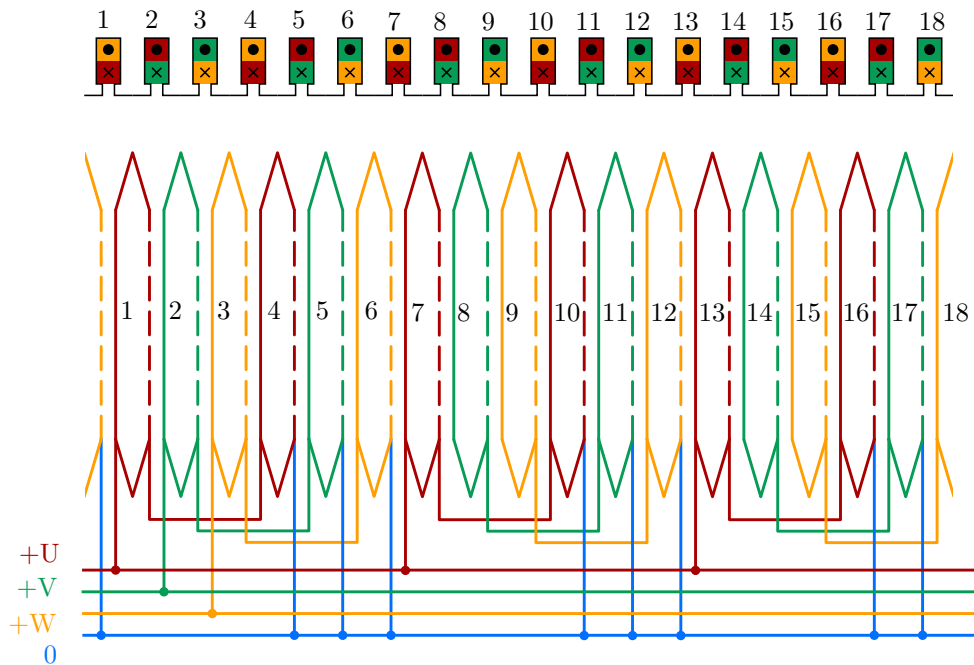Figure 5.12: 3S2P winding arrangement for an 18-12 machine

Figure 5.13: 2S3P winding arrangement for an 18-12 machine

5.3.2 Coil Winding and Testing

For this project, the first step of building the prototype machine is to wind the coils for the stator core. To achieve this, it was necessary to create a winding procedure for concentric, bobbin-wound coils. To make the bobbins capable of withstanding the heat produced in the stator, they are 3D-printed from a nylon material.

A jig was constructed and 3D-printed from the relatively cheap Polyethylene terephthalate glycol (PETG) as there are no special material requirements for this part. The jig is mounted on the winding machine for winding the copper wire around the bobbin. Figs. 5.14a and 5.14b respectively show an exploded and a fully constructed view of the jig assembly. The mandrel connects the shaft and spacer, with the bobbin on the opposite end. The compression plate is used for stabilisation and axially compresses the windings after the first layer, in order to eliminate any gaps between the individual windings.

The bobbins are only 0.8 mm thick and, as a result of the high tension of the copper wire during winding, the material can get warped and thus gets compressed onto the mandrel. This results in a high amount of force required to remove the wound coil after the winding process. For this reason, an aluminium shim is used to pull the wound bobbin off the mandrel. It should be noted that during the winding process a 3D-printed shim is used to not damage the copper wire insulation. After finished winding, the 3D-printed shim is carefully replaced with the aluminium version to pull off the coil without damaging the insulation.

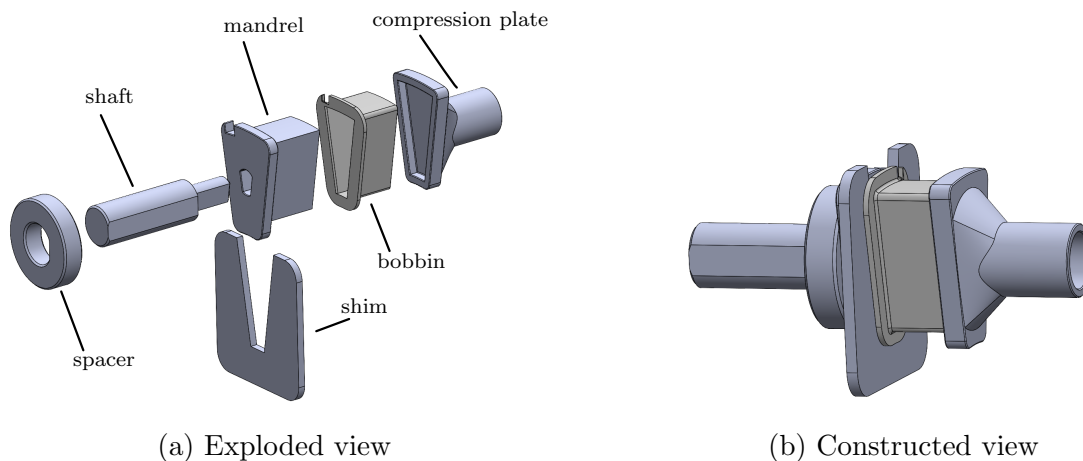(a) Exploded view   (b) Constructed view

Figure 5.14: Coil winding jig

During the winding process, the copper wire does not follow the shape of the mandrel and bobbin perfectly. A bulge forms on the sides of the coil. To mitigate this, two compression plates that are mounted on a vice are built (Fig. 5.15a). The coil is compressed with this method before it is pulled off the bobbin. The result can be seen in Fig. 5.15b. The left coil has not yet been compressed and has a bulge in it, that wastes space in the slot. The coils were wound with an AWG 19 wire with 35 turns per coil.

(a) Compression plates for the coils

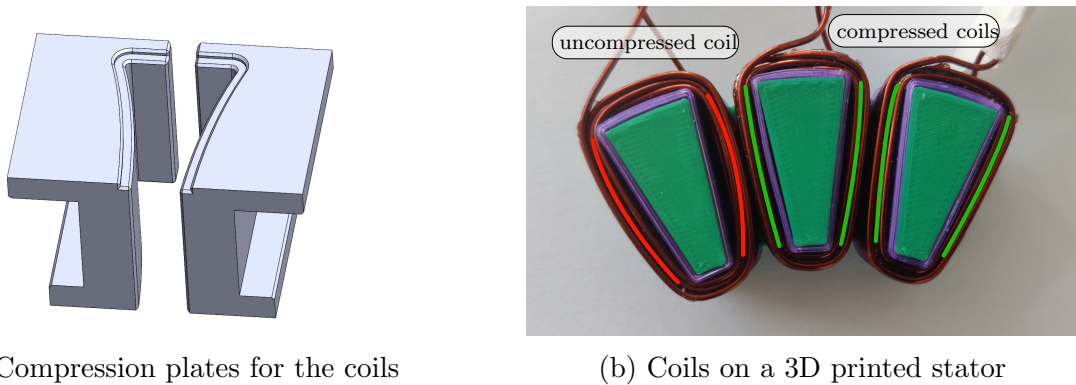(b) Coils on a 3D printed stator

Figure 5.15: Wound coils and compression plates to reduce wasted space in the slot.

The wound coils are then placed on each tooth of the stator core and are tested for any faults. The first check is done using an impulse tester (Tonghui TH2883), to verify there are no insulation defects between the coil windings. The principle of an impulse tester is shown in Fig. 5.16. The capacitance C_1 is charged via the source V_{DC} and a voltage pulse is released into the circuit. This oscillation circuit is made up of the capacitance C_2 as well as the inductance L_x and resistance R_x located in the device under test (DUT). Through analysing the waveform of the ring-down voltage $V_0(t)$, insulation defects can be found.
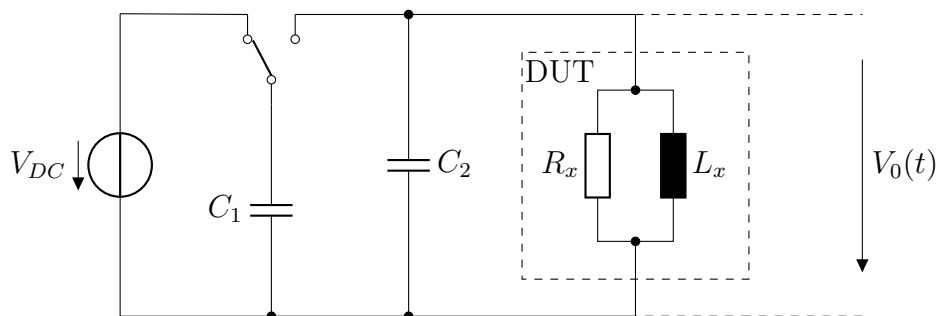

Figure 5.16: Simplified principle diagram of impulse testing

Fig. 5.17a shows the ring-down voltage of a coil that passed the test with a peak voltage of 2000 V. Fig. 5.17b shows a coil that was tested at 2500 V. The electric field in the insulation exceeded the breakdown voltage and a corona discharge appeared. Some of the first coils failed, as the aluminium shim was left on the mandrel during the winding process, thereby damaging the insulation.
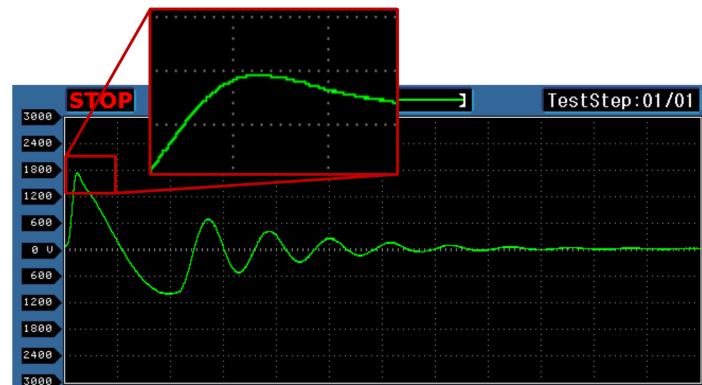
(a) Voltage waveform with no insulation breakdown
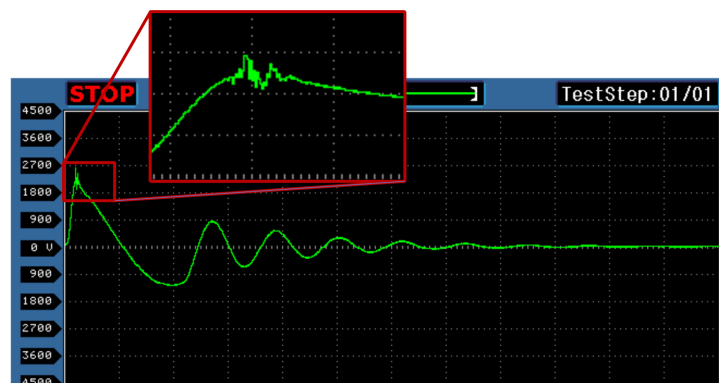
(b) Voltage waveform with corona discharge

Figure 5.17: Ring down of the voltage $V_0(t)$ over time

The insulation of the coils to the stator core was also tested using an insulation tester (RS Pro IIT-1500). An insulation tester works by applying a high DC voltage to the tested object and measuring the leakage current. Passing coils have a resistance larger than 22 GΩ between the coil and the core. However, multiple different coils on the same tooth showed a significantly lower resistance value. The reason for this was most probably a burr on the stator tooth, which damaged the nylon bobbin. This could be fixed by removing the burr on the stator tooth.

5.3.3 Stator Assembly

The next step is to build a housing for the stator. To dissipate the heat produced in the stator during operation, two cooling channels are machined into the back of the stator housing. The cooling system is sealed off by two o-rings and a backplate. Fig. 5.18a shows the aluminium stator housing and Fig. 5.18b shows the stator core with the assembled coils. Due to the cooling channels, there was no space for the coil terminals at the back of the machine. For this reason, cut-outs were spaced equidistant radially along the stator housing. The 18-12 machine has 18 coils with two ends each results in 36 copper wires. To save space, there are twelve cutouts in the housing and the beginning and end of a coil from each phase share a cutout. To be able to distinguish the phases, the coil terminals are colour coded and insulated. The stator core and coils are placed inside the housing and glued down. Four thermocouples were glued to various locations on a coil. The cut-outs were filled with silicone to prevent leakage and the stator housing was filled with an epoxy resin. Fig. 5.19a shows the stator at this stage.
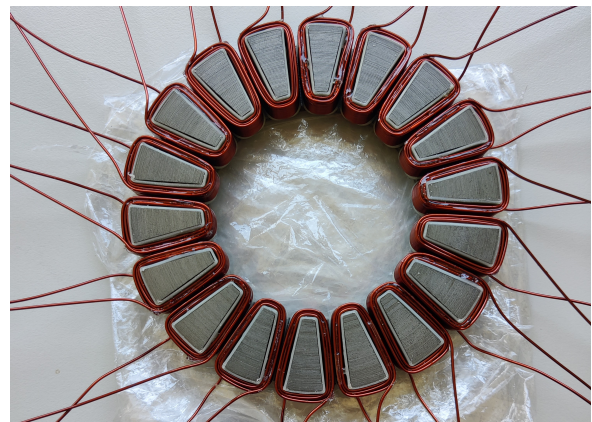

(a) Stator housing   (b) Stator with coils

Figure 5.18: Stator housing and core with assembled coils

A sleeve that could be mounted around the stator housing was 3D printed. In this sleeve, the coil wires are connected to ring terminals, which in turn are placed on a bolt. This allows access to every coil connection and strain-relieves the wires, mitigating the risk of tearing off the connection and making the motor unusable. Fig 5.19b shows a CAD view of the 3D printed sleeve and Fig. 5.19c shows the built stator with the phase connections.
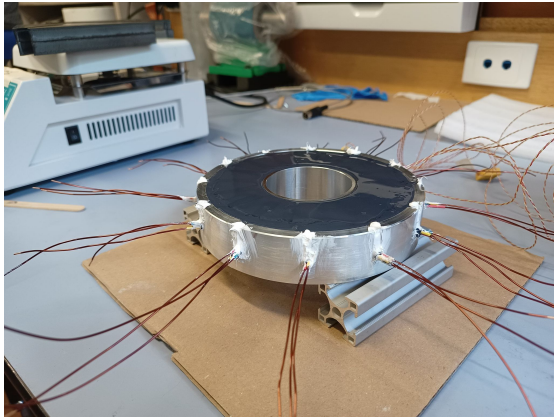
(a) Stator filled with epoxy resin


(b) CAD of the stator sleeve
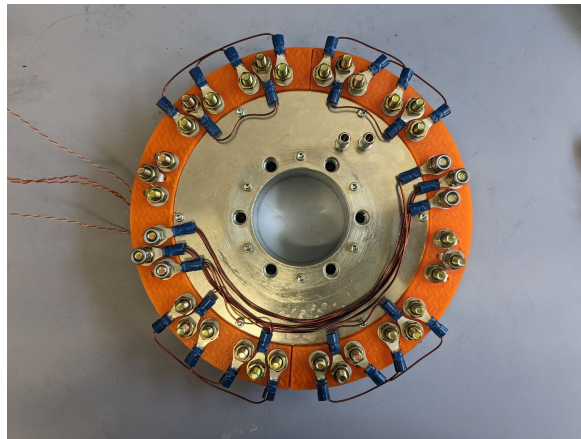
(c) Assembled stator

Figure 5.19: Stator assembly and components

5.3.4 Rotor Assembly

An aluminium rotor core housing was designed and manufactured. The rotor core is glued into the housing with a heat-curing glue. To position the magnets on the rotor and to prevent the magnets from attracting each other, a spacer was 3D printed from a nylon material. The spacer (Fig. 5.20a) made it relatively easy to position the magnets on the core until the glue hardened.

The polarity of the magnets must be carefully checked when placing them on the core. It is also important to note that a steel plate must be put onto the magnets to short-circuit the flux path before placing them in the oven to cure the glue. Otherwise, it is possible to demagnetise the magnets. The axial attraction force of 12 NdFeB magnets should also not be underestimated when placing the plate on the assembled rotor (cf. Section 5.2.4). The final rotor can be seen in Fig. 5.20b.
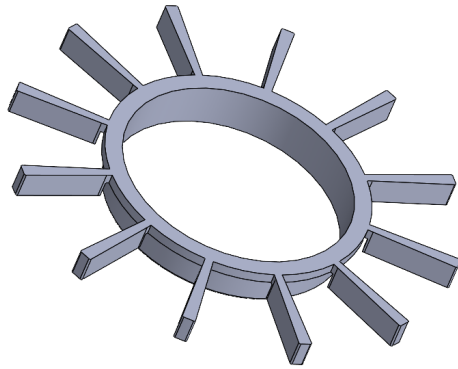
(a) Magnet spacer

(b) Assembled rotor

Figure 5.20: Assembled rotor and the spacer used while glueing the magnets

5.3.5 Test bench with Air Gap Actuation

The assembled prototype motor can be seen in Fig. 5.21a. The test configuration has been modified based on an existing setup. Next to the parts described above, an encoder mounting had to be incorporated into the setup. The rotor shaft moves when varying the air gap, so the encoder also has to move the same distance. For this reason, an encoder mount is 3D printed that sits on the positioning screw and thus moves the same axial distance. Fig. 5.21b shows a cut view of the encoder mount.
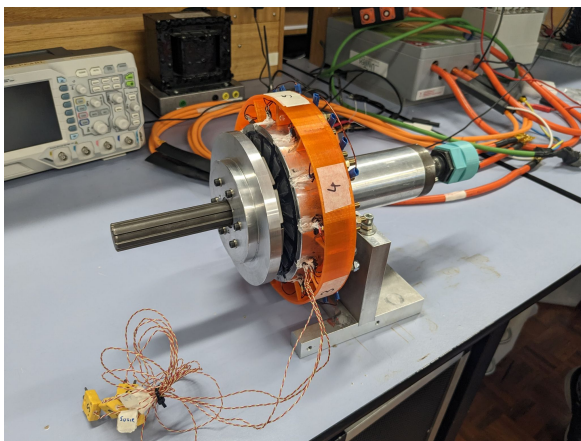
(a) Assembled prototype motor
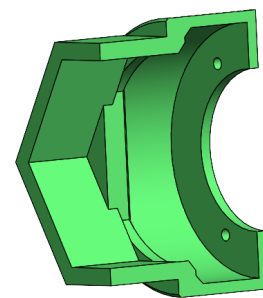
(b) Encoder mount

Figure 5.21: Fully assembled test bench and mounting for the encoder

Figs. 5.22, 5.23a and5.23b show different CAD views of the test bench. Mechanical rotor flux linkage control is made possible by turning the positioning screw on the right side of the machine. The other end of this positioning screw is pressed onto bearing B1. This bearing is in contact with bearing B2 via a spacer along the outer diameter. Bearing B2 in turn is pressed onto the rotor shaft. This allows for pushing the rotor away from the stator. When releasing the positioning screw, the axial attraction force pulls the rotor back to the stator. This allows a wide range of air gap actuation. However, the air gap width can only be set while the motor is not in motion.
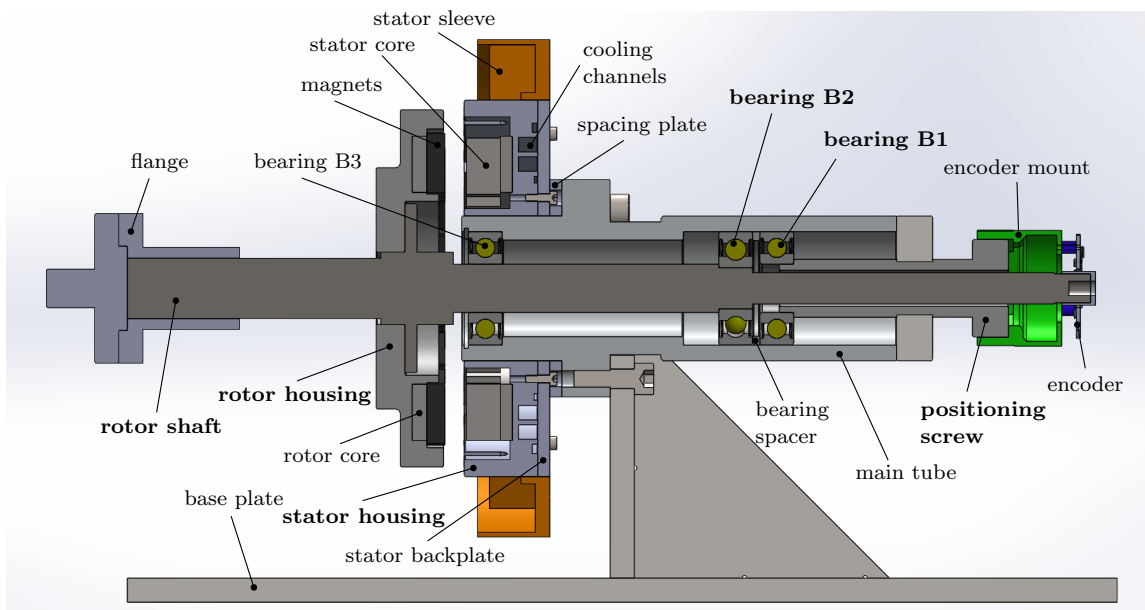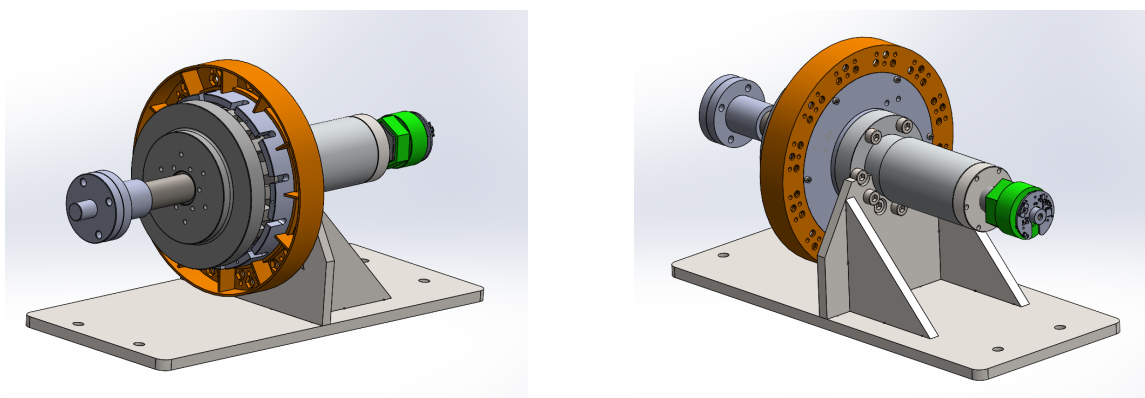

Figure 5.22: Cut view of the prototype motor

(a) Front view

(b) Rear view

Figure 5.23: CAD images of the constructed prototype

5.4 Comparison of Measurement and Simulation Results

5.4.1 Back-EMF and Spin-Down Test

The induced voltage for a fixed speed is measured and leads to the results shown in Fig. 5.24. The induced voltage is shown for three single coils, not the entire phases of the machine.
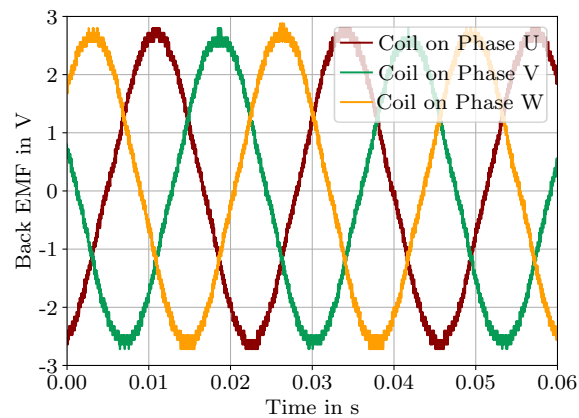

Figure 5.24: Back emf of the prototype motor

By measuring the back-emf for different motor speeds, the back-emf and torque constants of the machine can be calculated for different air gap widths. An efficient way to quickly achieve various speeds and induced voltages is by conducting a spin-down test. The external motor accelerates the DUT to a specific speed via a friction drive before being disconnected with a clutch. The induced coil voltage is then measured as the rotor decelerates. The resulting waveform for the machine at a 1 mm air gap width is depicted in Fig. 5.25a. The air gap was measured with a brass feeler gauge.

By measuring the peaks and zero-crossings, numerous voltage and speed points are derived. A linear function is fitted to the data points, of which the gradient describes the back-emf constant of the machine. Fig 5.25b shows the rms phase voltages over the speed, as well as the fitted linear function. To obtain the phase voltage, the induced coil voltage is multiplied by three since three coils are connected in series for each phase, following the 3S2P winding arrangement.
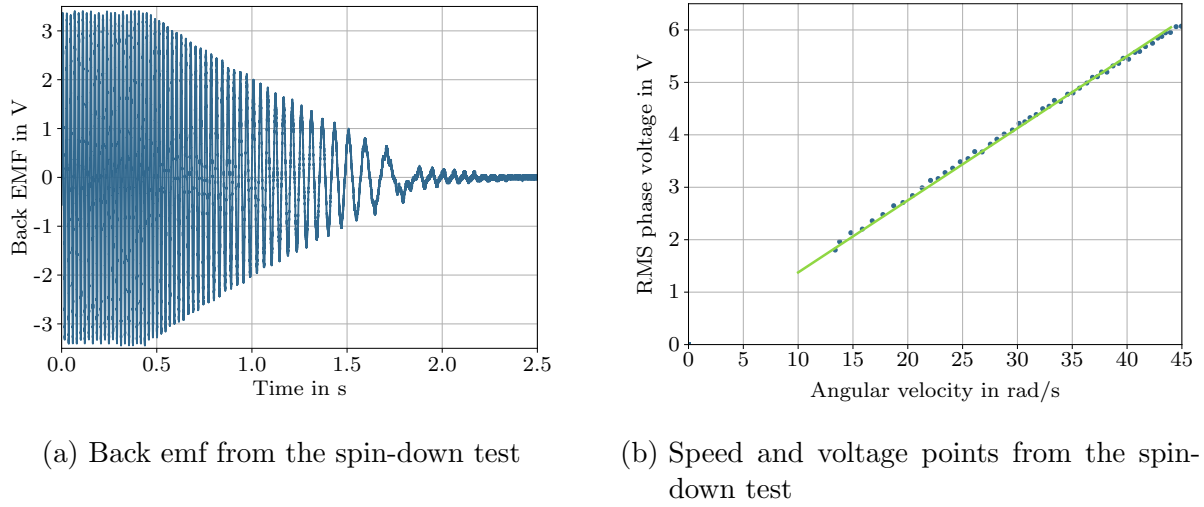
69

(a) Back emf from the spin-down test

(b) Speed and voltage points from the spin-down test

Figure 5.25: Spin-down test data of the prototype machine for an air gap width of $1\,\mathrm{mm}$.

The relation between the back-emf and torque constant can be shown by the power equation for phase voltage U, phase current I, torque T and speed ω

$$P = T \cdot \omega \approx 3 \cdot U \cdot I \ . \tag{5.3}$$

Rearranging the equation results to

$$\underbrace{\frac{T}{I}}_{k_\mathrm{t}} \approx 3 \cdot \underbrace{\frac{U}{\omega}}_{k_\mathrm{e}} \tag{5.4}$$

and therefore the relation between torque constant k_t and back-emf constant k_e is

$$k_\mathrm{t} \approx 3 \cdot k_\mathrm{e} \ . \tag{5.5}$$

The torque constant for different air gap widths is shown for simulated and experimental data in Fig. 5.26. Overall, the results look as expected. With increasing air gap width, the machine's torque constant decreases due to the reduction of permanent magnet flux linkage. However, the simulation overestimates the torque constant by approximately $25\,\%$. A reason for this could be the use of two-dimensional FEA and the resulting inaccuracy. Another reason could be the tolerance of the permanent magnet's remanence or coercivity. Another explanation could be inaccuracies in the measurement of the air gap width, which was measured with a brass feeler gauge.
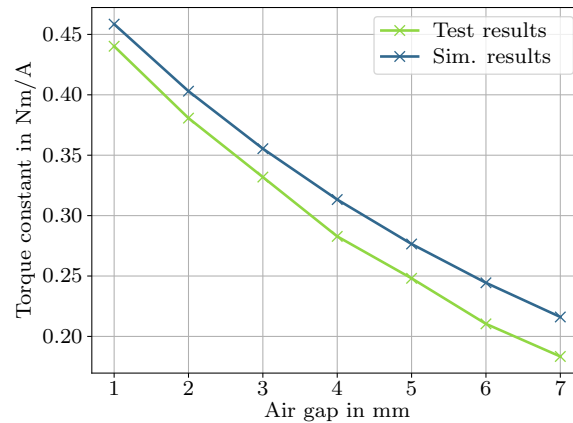
Figure 5.26: Torque constant of the prototype machine for different air gaps

5.4.2 Free Spinning Loss Test

A free spinning loss test is performed at different air gap widths by setting a specific speed with no load machine connected to the motor. The loss is measured with a power analyser (Yokogawa WT500) for different motor speeds. The results for $1\,\mathrm{mm}$ and $4\,\mathrm{mm}$ air gap widths are shown in Figs. 5.27a and 5.27b, respectively.
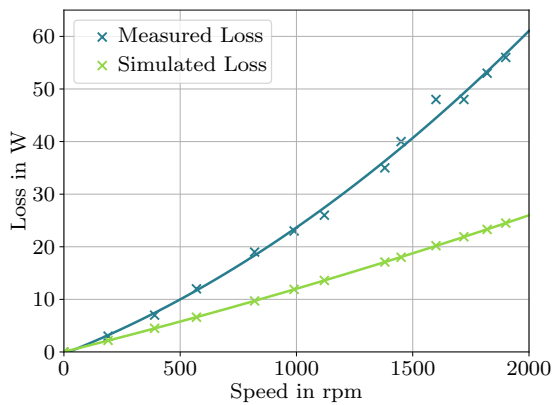
(a) Spinning Loss at $\delta = 1\,\mathrm{mm}$
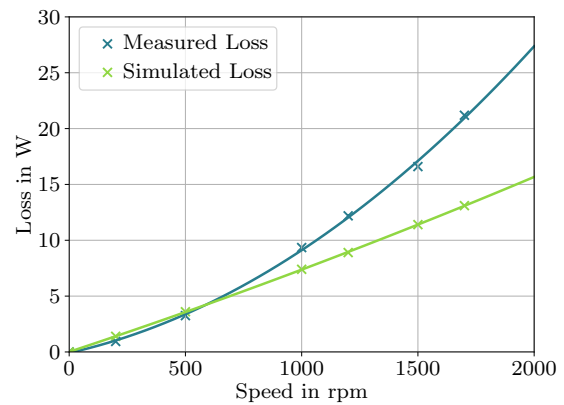
(b) Spinning Loss at $\delta = 4\,\mathrm{mm}$

Figure 5.27: Spinning Loss for increasing speed and two different air gap widths

The results show that the loss increases significantly with speed and is substantially higher than simulation results would suggest. One reason for this could be the negligence of alternating current losses (cf. Section 2.2.3 and Section 5.2.3) in the simulation. Another reason could be the saturation of the core material in the stator teeth or the yokes. When

magnetic material saturates, it could cause an increased stray flux in radial direction, therefore increasing core loss substantially due to the formation of eddy currents in the unlaminated direction.

A third possible explanation could be non-uniformity in the air gap through rotor excentricities or different winding resistances. Both could cause circulating currents, resulting in increased loss. The line-to-line resistances were slightly different with $277.4\,\Omega$, $277.5\,\Omega$ and $282.1\,\Omega$.

5.4.3 Load Test

The motor is connected to a load machine and tested at different speed and torque operating points and different air gap widths. Losses are measured via a power analyser and the motor efficiency is calculated. Fig. 5.28 shows the experimental and simulated results for a load of $9\,\mathrm{Nm}$ and motor speeds of $500\,\mathrm{rpm}$ and $2000\,\mathrm{rpm}$, respectively.
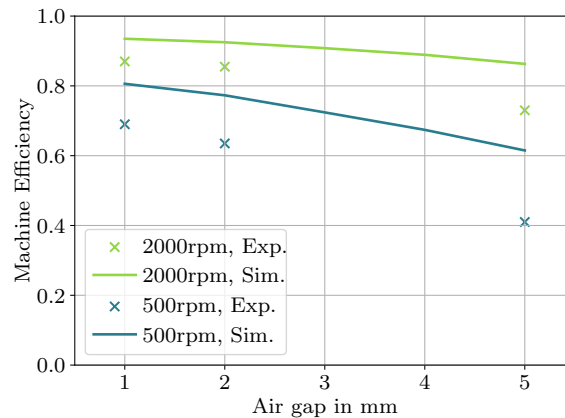
Figure 5.28: Efficiency of the machine for different air gap widths

As with the unloaded test, the results from the loaded test are unfortunately very far from the simulated values. Fig. 5.28 shows that the most significant difference between simulation and experimental results is at low speed and high air gap width. However, more operating options must be assessed to be able to draw a conclusion.

It is highly likely that the reasons for the discrepancies can be attributed to the same factors mentioned in the previous subsection. In addition, the losses of the load machine could further increase the problem.

6 Conclusion and Outlook

The world is moving towards the electrification of personal transport at a rapid pace. With electric motors already accounting for roughly 70 % of all the consumed energy in the EU [3], it is imperative to increase the energy conversion efficiency of electric machines.

The goal of this project was to investigate and design a new electric traction concept for a Formula Student racecar. The proposed electric motor is a single-sided AFM with surface-mounted magnets. This kind of machine topology has a high torque density, but often a bad CPSR.

However, a distinct advantage of this machine topology is that the air gap width between the rotor and stator can be varied during operation. Varying the air gap width can significantly increase the machine's efficiency but comes with some additional challenges.

A major difficulty lies in the design and optimisation process of the machine. Air gap variation essentially introduces an additional degree of freedom in the machine design process. In the past, electric machines were often designed and optimised for a single operating point. However, for a variable air gap machine used as a traction drive, this kind of design and optimisation method does not suffice. To find the most energy-efficient design, the machine must be optimised specifically for those operating conditions it will face during operation. For this reason, the evaluation concept introduced in this thesis aims to reduce computation time to a minimum to allow for a driving cycle based analysis.

The optimised design results in a highly efficient and light machine featuring 22.1 Nm/kg. Compared to a static air gap design, the machine's operating range and efficiency increase significantly when air gap variation is incorporated. A difference between simulation results and experimental data was observed when evaluating the prototype machine. Further investigation should be carried out to find the exact reason for these inconsistencies and the simulation model is required to be adapted to incorporate the respective factors.

Another challenge arises from the complex actuation mechanism together with the significant axial load acting on the machine's bearings. Bearing life is not a significant factor for racing applications, but it becomes very important in commercial vehicles.

The actuation mechanism proposed is suitable for the prototype, but does not allow for dynamic air gap variation during operation. Different concepts to achieve dynamic air gap variation exist, for example using a worm drive and a linear actuator or controlling the axial attraction force by varying the direct axis current. In any case, the lifespan of bearings must be considered.

The dynamics and energy consumption of the actuation mechanisms should also be taken into account during the design and optimisation process. This will indicate the full efficiency gain of such machines. The proposed machine design showed significant benefits, however, further research is required to assess the true potential of variable air gap machines.

In this thesis, it was shown that the proposed machine topology is a good candidate for future traction drives. The presented results form a solid basis for future research to build upon.

Bibliography

[1] L. Senn-Kalb and D. Mehta, *eMobility - In-depth Market Insights and Data Analysis*, Statista Std., Jun. 2022.

[2] IEA (8. August 2023), "Global EV Data Explorer," IEA, Paris. [Online]. Available: https://www.iea.org/data-and-statistics/data-tools/global-ev-data-explorer

[3] H. Gavrila, V. M. (Paltanea), G. Paltanea, G. Scutaru, and I. Peter, "New Trends in Energy Efficient Electrical Machines," *Procedia Engineering*, vol. 181, pp. 568–574, 2017.

[4] J.-P. Skeete, "The obscure link between motorsport and energy efficient, low-carbon innovation: Evidence from the UK and European Union," *Journal of Cleaner Production*, vol. 214, no. a, pp. 674–684, mar 2019.

[5] W. Cai, X. Wu, M. Zhou, Y. Liang, and Y. Wang, "Review and Development of Electric Motor Systems and Electric Powertrains for New Energy Vehicles," *Automotive Innovation*, vol. 4, no. 1, pp. 3–22, feb 2021.

[6] D. Hanselman, *Brushless Motors Magnetic Design, Performance, and Control of Brushless DC and Permanent Magnet Synchronous Motors.* E-Man Press LLC.

[7] G. R. Slemon, *Electric Machines and Drives.* Addison-Wesley Pub. Co., 1992.

[8] A. Emadi, *Advanced Electric Drive Vehicles.* Taylor & Francis Group, 2014.

[9] P. Vas, *Vector Control of AC Machines.* Clarendon Press, 1990.

[10] J. F. Gieras, *Axial Flux Permanent Magnet Brushless Machines.* Springer, 2008.

[11] N. Taran, G. Heins, V. Rallabandi, D. Patterson, and D. Ionel, "Torque Production Capability of Axial Flux Machines with Single and Double Rotor Configurations." IEEE, 2018.

[12] N. Taran, D. Klink, G. Heins, V. Rallabandi, D. Patterson, and D. M. Ionel, "A Comparative Study of Yokeless and Segmented Armature Versus Single Sided

Axial Flux PM Machine Topologies for Electric Traction," *IEEE Trans. on Ind. Applicat.*, vol. 58, no. 1, pp. 325–335, Jan. 2022, number: 1. [Online]. Available: https://ieeexplore.ieee.org/document/9629276/

[13] F. G. Capponi, G. D. Donato, and F. Caricchi, "Recent Advances in Axial-Flux Permanent-Magnet Machine Technology," *IEEE Transactions on Industry Applications*, vol. 48, no. 6, pp. 2190–2205, nov 2012.

[14] G. Heins, M. Thiele, D. Patterson, and N. Lambert, "Increase in Operating Range and Efficiency for Variable Gap Axial Flux Motors," in *2014 IEEE Energy Conversion Congress and Exposition (ECCE)*. Pittsburgh, PA, USA: IEEE, Sep. 2014, pp. 5870–5876. [Online]. Available: http://ieeexplore.ieee.org/document/6954207/

[15] M. Gulec and M. Aydin, "Implementation of different 2D finite element modelling approaches in axial flux permanent magnet disc machines," *IET Electric Power Applications*, vol. 12, no. 2, pp. 195–202, Feb. 2018, number: 2. [Online]. Available: https://onlinelibrary.wiley.com/doi/10.1049/iet-epa.2017.0434

[16] A. Parviainen, M. Niemela, and J. Pyrhonen, "Modeling of Axial Flux Permanent-Magnet Machines," *IEEE Trans. on Ind. Applicat.*, vol. 40, no. 5, pp. 1333–1340, Sep. 2004, number: 5. [Online]. Available: http://ieeexplore.ieee.org/document/1337061/

[17] O. Niemimäki and S. Kurz, "Quasi 3D modelling and simulation of axial flux machines," *COMPEL: The International Journal for Computation and Mathematics in Electrical and Electronic Engineering*, vol. 33, no. 4, pp. 1220–1232, Jul. 2014, number: 4. [Online]. Available: https://www.emerald.com/insight/content/doi/10.1108/COMPEL-11-2012-0352/full/html

[18] G. Weidenholzer, S. Silber, G. Jungmayr, G. Bramerdorfer, H. Grabner, and W. Amrhein, "A flux-based PMSM motor model using RBF interpolation for time-stepping simulations." IEEE, 4673.

[19] G. Weissitsch, D. Klink, G. Bramerdorfer, and G. Heins, "Computationally efficient driving cycle based design and optimisation for variable air gap axial flux machines," unpublished - Accepted for 2023 IEEE Energy Conversion Congress and Exposition (ECCE).

[20] G. Bramerdorfer and E. Marth, "Computationally Efficient System-Level Evaluation of Battery Electric Vehicles," in *2021 IEEE Workshop on Electrical Machines Design, Control and Diagnosis (WEMDCD)*. Modena, Italy: IEEE, Apr. 2021, pp. 311–317. [Online]. Available: https://ieeexplore.ieee.org/document/9425674/

[21] G. Bramerdorfer, J. A. Tapia, J. J. Pyrhonen, and A. Cavagnino, "Modern Electrical Machine Design Optimization: Techniques, Trends, and Best Practices," *IEEE Trans. Ind. Electron.*, vol. 65, no. 10, pp. 7672–7684, Oct. 2018. [Online]. Available: https://ieeexplore.ieee.org/document/8280552/

[22] X. Shao, P. Jiang, and Q. Zhou, *Surrogate Model-Based Engineering Design and Optimization.* Springer-Verlag GmbH, Nov. 2019. [Online]. Available: https://www.ebook.de/de/product/38112633/xinyu_shao_ping_jiang_qi_zhou_surrogate_model_based_engineering_design_and_optimization.html

[23] T. A. Runkler, *Data Analytics Models and Algorithms for Intelligent Data Analysis.* Springer Vieweg, 2020.

[24] S. Silber, W. Koppelstätter, G. Weidenholzer, G. Segon, and G. Bramerdorfer, "Reducing Development Time of Electric Machines with SyMSpace," Tech. Rep. which, 2023.

[25] D. Klink, "Design, manufacture and testing of an in-hub Axial Flux motor for a Formula Student Racecar," Master's thesis, Monash University, 2020.

[26] S. Amin, S. Madanzadeh, S. Khan, S. S. H. Bukhari, F. Akhtar, and J.-S. Ro, "Effect of the magnet shape on the performance of coreless axial flux permanent magnet synchronous generator," *Electrical Engineering*, vol. 104, no. 2, pp. 959–968, jul 2021.

[27] N. Taran, D. M. Ionel, V. Rallabandi, G. Heins, and D. Patterson, "An Overview of Methods and a New Three-Dimensional FEA and Analytical Hybrid Technique for Calculating AC Winding Losses in PM Machines," *IEEE Trans. on Ind. Applicat.*, vol. 57, no. 1, pp. 352–362, Jan. 2021, number: 1. [Online]. Available: https://ieeexplore.ieee.org/document/9242250/

Appendix

Calculation of Machine Mass

To calculate the machine's mass, the volume of each part is approximated geometrically. The mass of the machine is then calculated by multiplying the respective volume with the associated density. The geometry variables are introduced in Section 4.2.
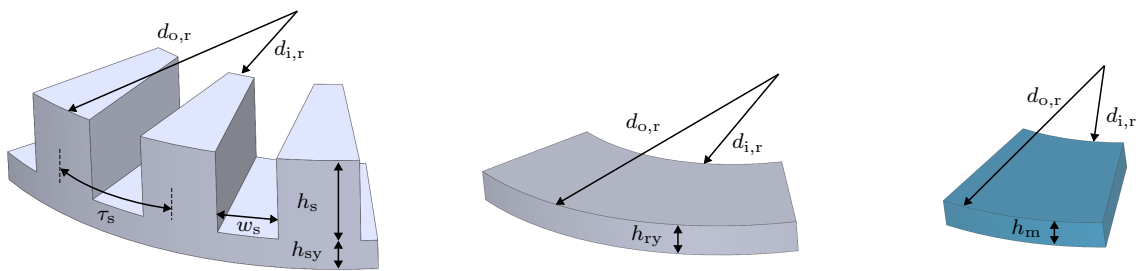

Figure 6.1: Geometry of the stator, rotor and magnet

Rotor Yoke Volume

The volume of the rotor yoke is given by the formula of an annulus

$$V_{\text{rotor}} = \frac{d_{\text{o,r}}^2 - d_{\text{i,r}}^2}{4} \cdot \pi \cdot h_{\text{ry}} \tag{6.1}$$

with

$$d_{\text{i,r}} = d_{\text{o,r}} \cdot k_{\text{ds}} \tag{6.2}$$

Appendix

Stator Yoke Volume

The volume of the stator yoke is given by the volume of an annulus with height $h_{sy} + h_s$ minus the volume of the slots.

$$V_{\text{stator}} = V_{\text{annulus}} - V_{\text{slots}} \tag{6.3}$$

The volume of the annulus is

$$V_{\text{annulus}} = \frac{d_{\text{o,r}}^2 - d_{\text{i,r}}^2}{4} \cdot \pi \cdot (h_{\text{sy}} + h_{\text{s}}) \ . \tag{6.4}$$

The exaggerated geometry of the slots is shown in Fig. 6.2. The volume of the slots can be approximated by three rectangles (A_1, A_2 and A_5) and two circle segments (A_3 and A_4)
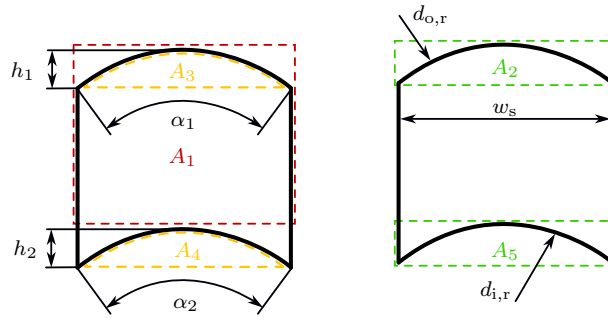

Figure 6.2: Geometry of a stator slot

$$V_{\text{slots}} = (A_1 - A_2 + A_3 - A_4 + A_5) \cdot h_{\text{s}} \cdot N_{\text{s}} \tag{6.5}$$

with N_{s} slots and

$$A_1 = w_{\text{s}} \cdot \frac{d_{\text{o,r}} - d_{\text{i,r}}}{2} \ . \tag{6.6}$$

For the rectangle A_2 and circle segment A_3, the formula is

$$A_3 = \frac{d_{\text{o,r}}^2}{8} \cdot (\alpha_1 - \sin(\alpha_1)) \ , \tag{6.7}$$

and

$$A_2 = w_{\text{s}} \cdot h_1 \; , \tag{6.8}$$

with

$$\alpha_1 = 2 \cdot \arcsin\left(\frac{w_{\text{s}}}{d_{\text{o,r}}}\right) \; , \tag{6.9}$$

$$w_{\text{s}} = \frac{d_{\text{o,r}} + d_{\text{i,r}}}{2} \cdot \frac{\pi \cdot k_{\text{sw}}}{N_{\text{s}}} \text{ and} \tag{6.10}$$

$$h_1 = \frac{d_{\text{o,r}}}{2} \cdot \left(1 - \frac{\cos(\alpha_1)}{2}\right) \; . \tag{6.11}$$

In the same way the calculation works for A_4 and A_5 with

$$A_5 = \frac{d_{\text{i,r}}^2}{8} \cdot (\alpha_2 - \sin(\alpha_2)) \; , \tag{6.12}$$

$$A_4 = w_{\text{s}} \cdot h_2 \; , \tag{6.13}$$

$$\alpha_2 = 2 \cdot \arcsin\left(\frac{w_{\text{s}}}{d_{\text{i,r}}}\right) \text{ and} \tag{6.14}$$

$$h_2 = \frac{d_{\text{i,r}}}{2} \cdot \left(1 - \frac{\cos(\alpha_2)}{2}\right) \; . \tag{6.15}$$

Magnet Volume

The magnet volume can also be calculated with the formula for an annulus under consideration of the pole arc to pole pitch ratio p_p

$$V_{\text{magnets}} = \frac{d_{\text{o,r}}^2 - d_{\text{i,r}}^2}{4} \cdot \pi \cdot h_{\text{m}} \cdot p_p \; . \tag{6.16}$$
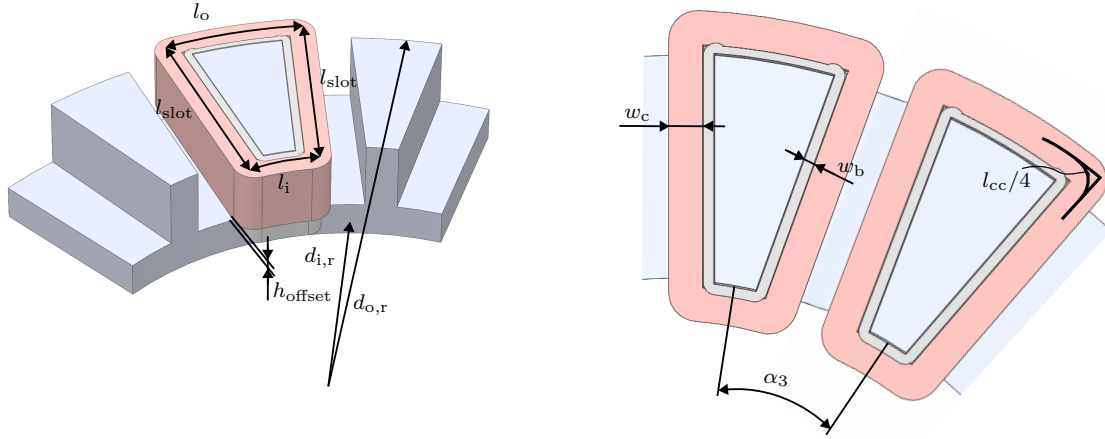
Winding Volume

Figure 6.3: Simplified geometry of a coil

To approximate the copper volume, the mean length of the coil is calculated. The length on the inside and outside of stator core are

$$l_i = d_{r,i} \cdot \sin\left(\frac{\alpha_3}{2} - w_b - w_c\right) \ , \tag{6.17}$$

and

$$l_o = d_{r,o} \cdot \sin\left(\frac{\alpha_3}{2} - w_b - w_c\right) \tag{6.18}$$

with the bobbin width w_b, coil width

$$w_c = \frac{w_s - 3 \cdot w_b}{2} \ , \tag{6.19}$$

and angle

$$\alpha_3 = \frac{2 \cdot \pi}{N_s} \ . \tag{6.20}$$

The length in the slot is

$$l_{slot} = \frac{d_{o,r} - d_{i,r}}{2} + 2 \cdot w_b + w_c \tag{6.21}$$

As the coil does not turn in a sharp corner, a corner correction factor

$$l_{cc} = 4 \cdot w_c - \pi \cdot w_c \tag{6.22}$$

is applied. The copper volume results to

$$V_c = (l_i + l_o + 2 \cdot l_{slot} - l_{cc}) \cdot w_c \cdot h_c \ . \tag{6.23}$$

The coil height

$$h_c = (h_s - h_{offset} - w_b) \cdot k_{ff} \tag{6.24}$$

depends on slot height, bobbin width, the offset of the coil from the stator yoke h_{offset} and the fill factor k_{ff}.
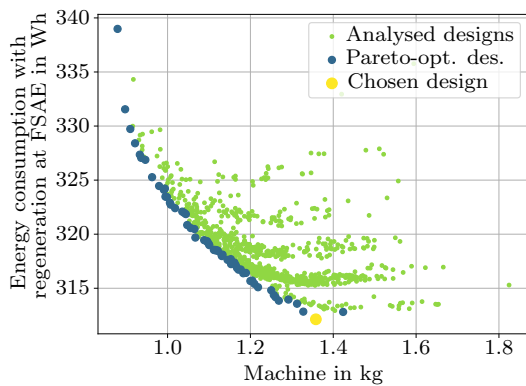
Optimisation Results

When the combustion-engined car decelerates, it uses its brake discs to convert the kinetic energy into heat. Electric vehicles, however, can use their motors as generators during braking to recharge the accumulator. This reduces energy consumption and is an important fact to consider in the optimisation process. Fig. 6.4 shows the results from the second optimisation scenario, including energy regeneration. In this case, energy regeneration does not have a huge impact on the optimal machine design.
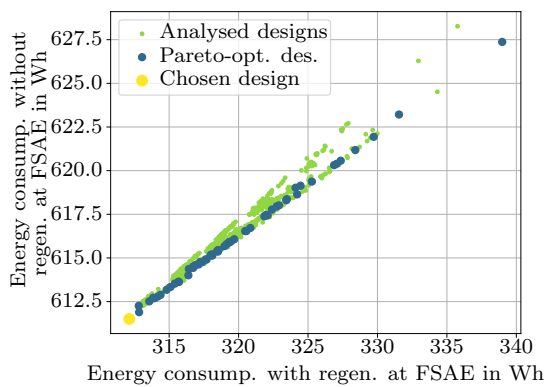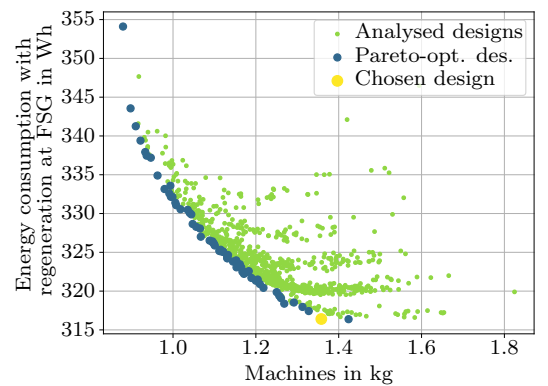

(a) Energy consumption with and without energy regeneration for the FSAE cycle
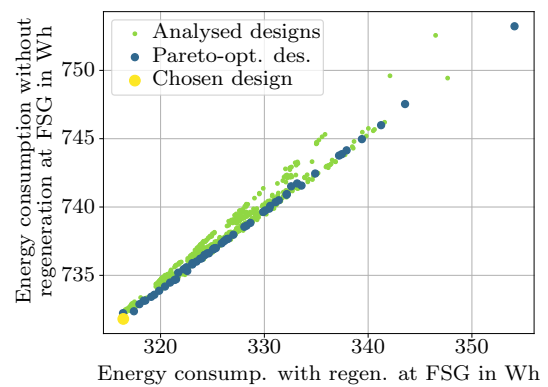
(b) Energy consumption with and without energy regeneration for the FSAE cycle

(c) Energy consumption with regeneration over mass for the FSAE cycle

(d) Energy consumption with regeneration over mass for the FSG cycle

Figure 6.4: Optimisation results considering regenerative breaking

Calculation of Wire Diameter and Turns

The copper wire diameter and number of turns depends on the winding arrangement of the machine. The following section derives these values. The derivation is based on achieving a similar torque constant as a reference motor.

Assuming an rms accumulator voltage of

$$V_{\mathrm{rms}} = 178.5\,\mathrm{V}\ ,$$

and aiming for a base speed of

$$\omega_{base} = 11600\,\mathrm{rpm}\ ,$$

the use of equation (5.4) results in a back-emf constant of

$$k_{\mathrm{e}} = \frac{V_{\mathrm{rms}}}{\omega_{base}} = 0.147\,\frac{\mathrm{V}}{\mathrm{rad/s}}\ ,$$

and a torque constant of

$$k_{\mathrm{t}} = 3 \cdot k_{\mathrm{e}} = 0.441\,\frac{\mathrm{Nm}}{\mathrm{A}}\ .$$

To achieve a torque of

$$T = 30\,\mathrm{Nm}$$

with this torque constant, an rms phase current of

$$I_{\mathrm{rms}} = \frac{T}{k_{\mathrm{T}}} = 68\,\mathrm{A}$$

is necessary. In general the relationship between current I and current density J in a conductor with the area A is

$$I = J \cdot A\ . \tag{6.25}$$

Considering this, the necessary MMF can be calculated for the area of a of one coil A_{coil} with equation (2.20)

$$\mathcal{F} = N \cdot I_{\mathrm{rms}} = A_{\mathrm{coil}} \cdot J\ . \tag{6.26}$$

Rearranging the equation gives the necessary number of turns

$$N = \frac{A_{\text{coil}} \cdot J}{I_{\text{rms}}}.$$

(6.27)

Equation 6.27 assumes all the coils to be in series and therefore has to be adapted to consider n_{p} parallel paths

$$N = \frac{n_{\text{p}} \cdot A_{\text{coil}} \cdot J}{I_{\text{rms}}}.$$

(6.28)

Assuming a current density of

$$J = 40 \, \frac{\text{A}}{\text{mm}^2} \, ,$$

and a coil area of

$$A = 28.45 \, \text{mm}^2 \, ,$$

the calculation for all possible winding arrangements gives:

$$N_{\text{6S}} = 17 \, ,$$

$$N_{\text{3S2P}} = 34 \, ,$$

$$N_{\text{2S3P}} = 51 \, , \text{ and}$$

$$N_{\text{6P}} = 102 \, .$$

Finally, the diameter d of the copper wire can be calculated by rearranging the formula of the area of a circle to

$$d = \sqrt{\frac{4 \cdot A_{\text{coil}}}{\pi}} \, ,$$

(6.29)

resulting in

$$d_{\text{6S}} = 1.46 \, \text{mm} \, ,$$

$$d_{\text{3S2P}} = 1.03 \, \text{mm} \, ,$$

$$d_{\text{2S3P}} = 0.84 \, \text{mm} \, , \text{ and}$$
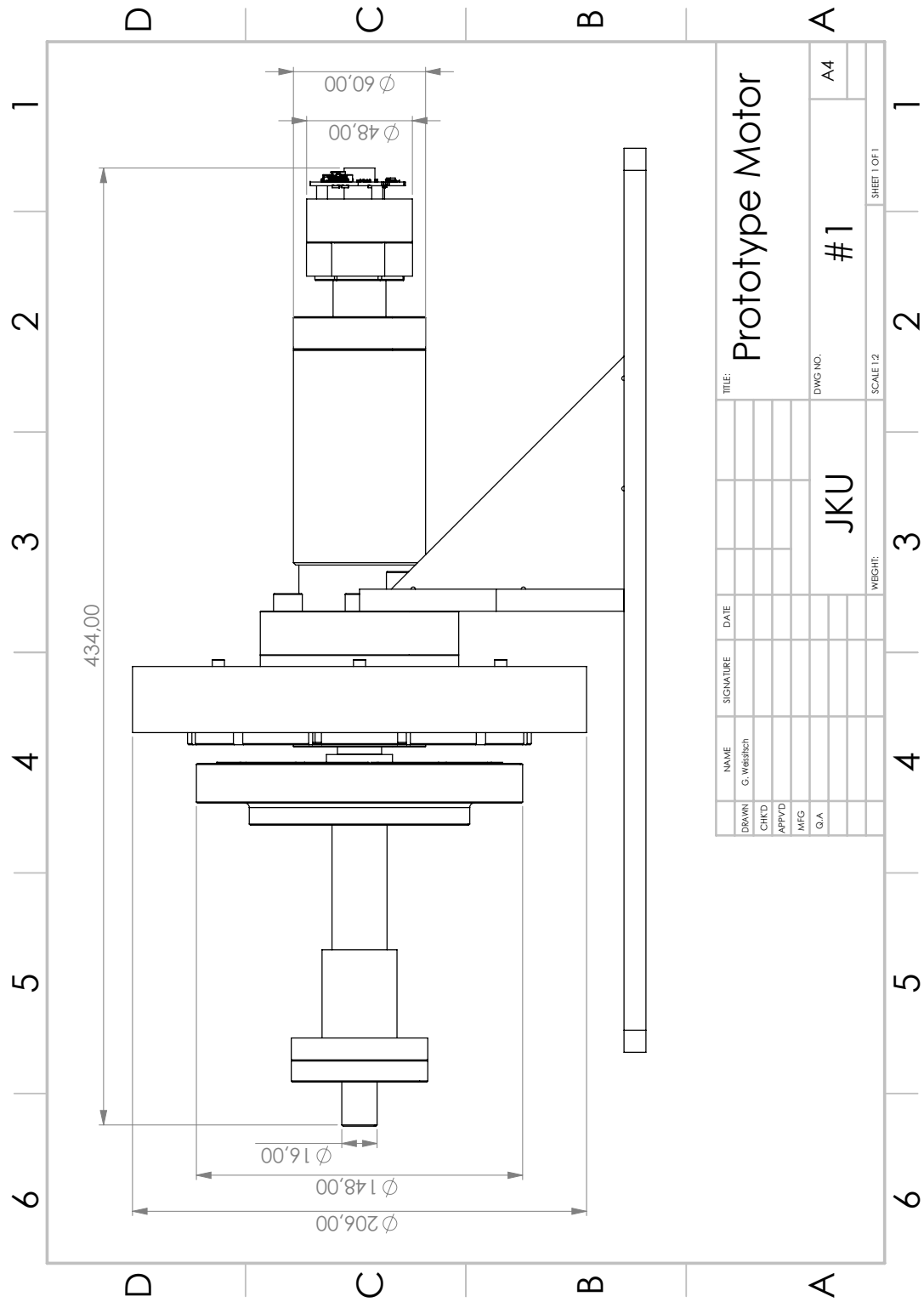
$$d_{\text{6P}} = 0.60 \, \text{mm} \, .$$

Prototype Motor Dimensions

Figure 6.5: Dimensions of the prototype machine